3D structured graphenes as (photo)catalysts

DOCTORAL THESIS

Presented by:

Ana García Mulero

Directors:

Prof. Hermenegildo García Gómez

Dr. Ana Primo Arnau

Valencia
Febrero 2023

Dr. HERMENEGILDO GARCÍA GÓMEZ, Professor of the Universitat Politècnica de València and Dr. ANA PRIMO ARNAU, tenured scientist at the Instituto de Tecnología Química (UPV-CSIC) as supervisors,

CERTIFY, that this doctoral thesis, entitled: "3D graphenes as (photo)catalysts", has been developed by Ana García Mulero, in the doctoral program in Sustainable Chemistry, at the Instituto de Tecnología Química (ITQ), Universitat Politècnica de València (UPV).

Prof. Hermenegildo García Gómez   Dr. Ana Primo Arnau

AGRADECIMIENTOS

Desde siempre, en casa hemos usado el refranero español hasta en la más mínima ocasión, así que esta no puede ser menos. Porque es de ser bien nacido el ser agradecido, con lo que debería comenzar esta sección (la que todo el mundo se lee) con el Proyecto PID2021-126071OB-C21 financiado por MCIN/ AEI /10.13039/501100011033/ y por FEDER Una manera de hacer Europa, por toda la financiación recibida, y al Ministerio por la FPU que me ha permitido desarrollar estos 4 años de trabajo. Y también gracias a esas personas que han pasado, se hayan quedado o no, porque de todo se aprende. Pero dejemos de ser serios, que para eso está el resto de la tesis.

En primer lugar, le quiero dar las gracias al Prof. Hermenegildo García, por dejarme entrar en el mundo de la investigación, por guiarme, por tu intensidad y por sacar lo mejor de cada uno del grupo (y por todos los documentos que te he hecho firmar). Sinceramente, ha sido un auténtico lujo poder aprender de ti. A la Dra. Ana Primo, por tu tesón, por enseñar todo cuanto ha estado en tu mano y por hacer el mejor equipo con Herme.

¿Por quién debería seguir? Quizá por las que han aguantado los altos y los bajos, los “no me esperéis que tengo clase”, y “no sé qué hago aquí”. Y es que, Esther y Amparo, sois el mejor dúo. Hacéis fácil consideraros familia con vuestros consejos, anécdotas y el “todas a una” cuando la cosa se pone complicada. Josep, gracias por tu humor ácido, pero sobretodo, por esa paciencia con quien te necesita, sea quien sea. Sara, la calma hecha persona, pero dispuesta a apuntarse a un bombardeo, qué suerte hemos tenido con tu llegada. Gracias por haber estado ahí.

Alejandra, mi pareja de la guardia civil, la versión cuqui de “Tú a Londres y yo a California”. La que, aunque haya 4300 km, sigue estando. Gracias por los *melona* cuando lo merecía, por animarme en todos y cada uno los momentos esta etapa, y por ser mi *re-cordis*.

Para acabar con el G3, vamos a la parte internacional: Yong, Horatiu and Dawid. You make us the most international lab. Thank you for all the good moments and scientific discussions.

A todo el A4, desde el predoc más veterano (aka Rubén) al más nuevo, y bueno, María, pero tú ya eres postdoc. Andrés, Alberto, Jiajun, Guillermo…, por todos los ratos vividos en los largos días de ITQ (y por los cotis, que dan la vida). Y Elena, aunque no seas oficialmente del grupo, dile a Pedro que te adoptamos. A todos, gracias por hacer que las horas pasaran fast and furious. Y gracias al resto de predocs que me he encontrado en esta etapa en el ITQ. Especialmente a Pili e Iván, que siempre han tenido palabras de afecto.

Tampoco puedo olvidar a caracterización, sobre todo las que he visitado con más frecuencia: Fany, Chusa, Maribel, Amparo, Dolo y Adelina. Sin vosotras el trabajo en el ITQ sería 100 veces más complejo.

Y hablando de técnicas de caracterización, gracias al equipo de microscopía con el que tantas horas he pasado, especialmente a José Luís, Ximo y Ali. Gracias por las fotos, por la paciencia y, en definitiva, por vuestra impecable profesionalidad.

Siguiendo con lo profesional, tuve la suerte de ir de estancia a centro Conditions Extrêmes et Matériaux: Haute Température et Irradiation (CEMHTI para los amigos) y sería un delito olvidarme de ellos.

A la Dra. Conchi O. Ania, por darme la oportunidad de pasar 3 maravillosos meses en Orleans aprendiendo y disfrutando de mi trabajo al mismo tiempo. Al Prof. Jesús Iniesta, por sus ganas, sus ideas y su optimismo ante los resultados. Roxana, esa señorita que me facilitó tanto llegar a querer la ciudad. Ojalá sigas siendo así de noble y nada pueda pararte los pies. A Martín, el miembro que me faltaba del equipo español que invadía Francia desde dentro. Por tus palabras de aliento en todo momento y hacer que el ánimo no decayese.

Next I should mention the non-Spanish speakers (for now). Hassan, who I spent with almost my entire internship. I became in your shadow, and you did not complain at all (in my presence). I really owe you a lot. Kana, my sweet girl, is a great professional but an even better person. Nadia, the most caring postdoc, Mauree and Ieuan, les plus sportifs; Dani and his quiet invasion to my desk; Khashayar, better known as Khasy; Ilhem, our brave girl; Haytem (finally I learnt your name, pinky promise); Ilse, excuse me I'm walking like a zombie… I know you get a déjà vu (la italiana con el mejor acento *granaíno*). I will never forget all the good moments. Bref, à toutes les personnes que j'ai rencontrées au CEMHTI car les 3 mois sont passés trop vite. Merci à vous tous .

Volviendo a Almería, mis mosqueteras. Gracias Cris, por recibirme con los brazos abiertos cada vez que he vuelto a casa y por hacerme partícipe de este grupo tan fantástico: Antonio, Joserru, Alex, Andrés y Carolina. A vosotros también gracias de corazón. Por acabar con las preocupaciones de un plumazo (incluso desde Irlanda) y por escucharme hablar de ciencia, aunque tengáis que poner cara de paisaje a veces. Mención especial a Carol por mejor portada de tesis del mundo (mundial). Y la otra mosquetera, la más aventurera, Isa. Porque puede que pase el tiempo, pero seguimos siendo las mismas. No es que sea un “si te tiras por el puente, yo voy detrás” pero si es por la borda de un barco… no te digo que no.

De Murcia me faltan un par que hace 10 años que nos cruzamos por primera vez y aquí siguen. Adolfo, gracias por las caminatas *pasilliles* post cena, por ser un mar de tranquilidad y por tus visitas exprés a Valencia llenas de ataques de risa y de búsquedas de parking. Subi y Rubén, por los abrazos de oso, por compartir vuestro tiempo y seguir estando. Y Damián, por esos cafés y puestas al día en Murcia, pero, lo que es más importante, ese superpoder de llamar por sorpresa cuando más lo necesito.

Gracias a mis señoritas veteranas de primera, Elena y Cristina Miñarro. Hace 6 años que nos fuimos de la resi pero seguimos compartiendo drama y cotilleo, y, por qué no, Champions y bodorrios. Y no, no me he olvidado de ti. Julia. Esta muchacha necesitaría su propio capítulo en los agradecimientos porque, entre otros, podría competir con mi propia madre en cuanto a orgullo por mis logros. Todo comenzó con un par de novatas de la tercera y bendito momento en que te encontré. La que ha leído (y sufrido) la tesis para echarle un ojo al inglés, tiene el cielo ganado. Tú tan de Letras y yo tan de Ciencias, pero qué bien nos entendemos. Gracias por cometer locuras conmigo y por empujarme a hacerlas, aunque me de miedo.

Por último, a mi familia. Por ser. Por estar. Por acompañarme en este camino que ya se acaba y ser un pilar fundamental. Por animarme a terminar cada proyecto que he comenzado. Y por quererme con mis taritas.

A todos. GRACIAS.

If you can dream- and not make dreams your master.

If you can think- and not make thoughts your aim.

If you can meet with Triumph and Disaster,

And treat those two impostors just the same;

If you can bear to hear the truth you've spoken

Twisted by knaves to make a trap for fools,

Or watch the things you gave your life to broken,

And stoop and build 'em up with worn out tools.

If, Rudyard Kipling (1895)

Symbols and abbreviations

°C	Celsius degrees
µmol	Micromol
2D	2 dimension
3D	3 dimension
a. u.	Arbitrary Units
AFM	Atomic Force Microscopy
BHT	Butylated hydroxytoluene
C	Carbon
CA	Chronoamperometry
CB	Conduction band
CV	Cyclic Voltamperometry
DLS	Dynamic Light Scattering
DMSO	Dimethyl sulfate
e^-	Electron
EDS	Energy-dispersive X-ray spectroscopy
EU	European Union
eV	Electron-volt
FESEM	Field Emission Scanning Electron Microscope
FTO	Fluorine-doped tin oxide glass
FWHM	Full width at half maximum
g	Gram
GC	Gas chromatography
GC-MS	Gas Chromatography/Mass Spectrometry
GO	Graphene oxide
h	Hour
h^+	Hole
HRTEM	High Resolution Transmission Electron Microscopy
ICP-OES	Inductively Coupled Plasma Optical Emission spectroscopy
J	Joule
mA	MiliAmper
mau	Mass atomic unit
mL	Milliliter
mM	MiliMolar
mmol x g^{-1}	Milimol per grame

mp	microporous
N	Nitrogen
NHE	Normal Hydrogen Electrode
nm	Nanometer
NMP	N-Methylpyrrolidone
NMR	Nuclear magnetic resonance spectroscopy
ns	Nanosecond
P	Phosphorous
PVDF	Polyvinylidene fluoride
SCE	Saturated Calomelanos Electrode
TCD	Thermal Conductivity Detector
TEMPO	2,2,6,6-Tetramethylpiperidine 1-oxyl
TEOA	Triethanol amine
UN	United Nations
US DoE	United States Department of Energy
UV	Ultraviolet
UV-Vis	Ultraviolet-Visible
V	Volt
VB	Valence band
W	Watt
XPS	X-Ray photoelectron spectrometry
λ	Wavelength

Index

Chapter 1. Introduction 1

1.1 Introduction 3

1.2 Solar fuels 6

1.3 Polysaccharides as biomass waste converted into photocatalysts 12

  1.3.1 Defective graphenes as catalysts and photocatalysts 14

  1.3.2 Microporous ordered graphitic carbons 19

  1.3.3 Cyclodextrins 23

1.4 References 30

Chapter 2. Objectives 39

Chapter 3. Microporous graphitic carbons prepared using soft templates employed in zeolite synthesis and their catalytic activity in aerobic oxidation 47

3.1 Introduction 47

3.2 Results and discussion 50

  3.2.1 Samples preparation 50

  3.2.2 Characterization 52

  3.2.3 Electron microscopy 58

  3.2.4 Catalytic activity 61

  3.2.5 Conclusions 68

3.3 References ... 70

Chapter 4. Cyclodextrins as precursors of microporous graphitic carbons. Band engineering by phosphorous doping ... 75

4.1 Introduction ... 75
4.2 Results and discussion ... 77
  4.2.1 Material preparation and characterization ... 77
  4.2.2 Photocatalytic hydrogen evolution in the presence of sacrificial electron donor ... 96
  4.2.3 Photocatalytic oxygen generation ... 106
  4.2.4 Photocatalytic overall water splitting ... 107
  4.2.5 Metal or metal oxide photodeposition ... 109
  4.2.6 Photocurrent measurements ... 112
4.3 Conclusions ... 117
4.4 References ... 119

Chapter 5. All carbon, metal-free, and doped microporous graphitic carbon as photocatalyst for the selective CO_2 reduction to CO ... 125

5.1 Introduction ... 125
5.2 Results and discussion ... 126
  5.2.1 Photocatalytic activity ... 133
  5.2.2 Photocurrent measurements ... 142
  5.2.3 Transient adsorption spectroscopy study ... 143

5.3 Conclusions 148
5.4 References 149

Chapter 6. Electrocatalytic activity of microporous graphitic carbons for CO_2 reduction 153

6.1 Introduction 153
6.2 Results and discussion 154
  6.2.1 Electrochemical evidence of CO_2 reduction by microporous graphitic carbons 158
  6.2.2 Electrochemical CO_2 reduction 160
6.3 Conclusions 162
6.4 References 163

Chapter 7. Experimental Section 167

7.1 Material synthesis 167
  7.1.1 Microporous graphenic carbon using a soft template 167
  7.1.2 Microporous 3D graphenic carbon based on cyclodextrins 168
  7.1.3 Microporous 3D graphenic carbon doped with heteroatoms 168
7.2 Reaction procedure 169
  7.2.1 Oxidation of benzylamine 169
  7.2.2 Water splitting reaction 169
  7.2.3 Platinum photodeposition 170
  7.2.4 Chromium photodeposition 171
  7.2.5 CO_2 photoreduction 171

7.2.6 Electrocatalytic CO_2 reduction ... 172
7.3 Electrochemical measurements ... 173
7.3.1 Electrode preparation ... 173
7.3.2 Photoelectrochemical measurements of the mp-(P)C materials 173
7.3.3 Conductivity measurements ... 174
7.3.4 Nyquist plots ... 174
7.3.5 Mott-Schottky plots ... 174
7.3.6 Photoelectrochemical measurements of the mp-C_α for CO_2 photoreduction ... 175
7.3.7 Electrochemical characterization for CO_2 electroreduction ... 175
7.4 Characterization techniques ... 176
7.4.1 Diffuse Reflectance UV-Vis Spectroscopy (DRS) and Fluorescence Spectrocopy ... 176
7.4.2 Combustion elemental analysis ... 176
7.4.3 Field Emission Scanning Electron Microscopy (FESEM) ... 177
7.4.4 Inductive Coupled Plasma-Optical Emission Spectrometry (ICP-OES) 177
7.4.5 Isotherm gas adsorption ... 177
7.4.6 Raman spectroscopy ... 177
7.4.7 Solid-State Nuclear Magnetic Resonance Spectroscopy ... 178
7.4.8 Thermogravimetric analysis (TGA) ... 178
7.4.9 Transient absorption measurements ... 178
7.4.10 Transmission Electron Microscopy (TEM) ... 178
7.4.11 X-Ray diffraction (XRD) ... 179
7.4.12 X-Ray Photoelectron Spectroscopy (XPS) ... 179
7.5 Other procedures ... 180
7.5.1 Valence band calculation ... 180

Chapter 8. Conclusions 183

Abstracs 185

9.1 Resumen 187
9.2 Abstract 189
9.3 Resum 191

List of publications 193

CHAPTER 1.

INTRODUCTION

1.1 Introduction

Current societies depend considerably on the consumption of energy to develop the majority of personal and industrial activities. The massive use of hydrocarbons as a primary energy source has led to the corresponding amount of CO_2 emitted into the atmosphere, and they are partially dissolved in the oceans. While the concentration of CO_2 in the atmosphere before World *War* II was estimated at 300 ppm, nowadays, there is an emission of almost 40 Gton of CO_2 per year as a consequence of the combustion of fossil fuels, mainly natural gas, oil, and coke.[1] These emissions have caused a significant increase in atmospheric CO_2 concentration from below 200 ppm to over 400 ppm in less than a century. Scientific studies on perennial ice in the Antarctic continent have been able to determine the concentration of CO_2 in the atmosphere over a period of millions of years. The Antarctic ice in contact with the corresponding atmosphere has captured air bubbles deeper below the surface as it ages. These studies have been able to correlate periods of high atmospheric CO_2 concentration with tropical climate on the Earth, while cold periods are associated with low atmospheric CO_2 concentration.[2]

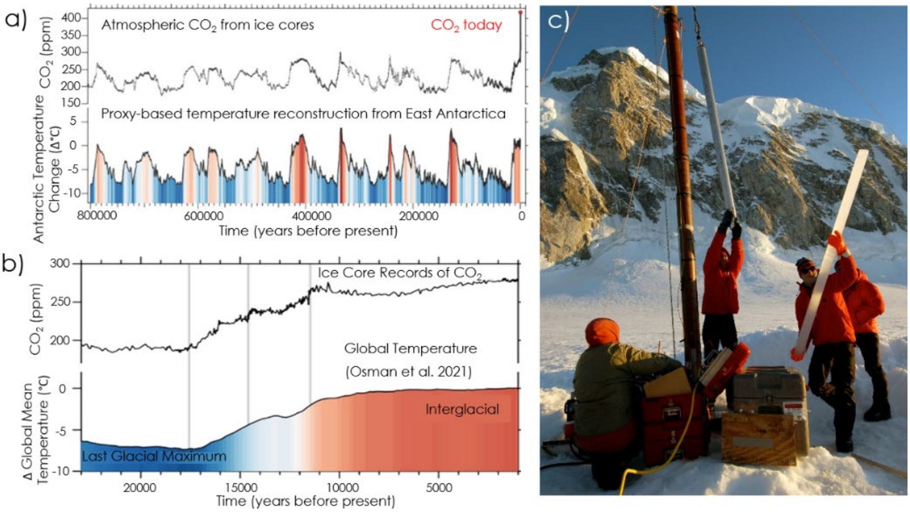

Figure 1.1. a) Ice core records for atmospheric CO_2 and temperature change in Antarctica; b) Atmospheric CO_2 and global temperature from the last ice age to the Industrial Revolution and c) Photography from the ice core sampling.[3]

In addition, studies on the Earth's atmosphere have shown that certain gases influence the temperature of the Earth's crust through the so-called greenhouse effect. Figure 1.2 illustrates in a pictorial way the greenhouse effect. This effect is due to the reabsorption of the atmosphere of near-infrared emissions from the Earth's surface (land and sea) that is responsible for the thermal equilibration of the planet. The absorption of this IR irradiation and the emission back to the Earth avoid the dissipation of the heat to the stratosphere, causing planet heating. [1,2]

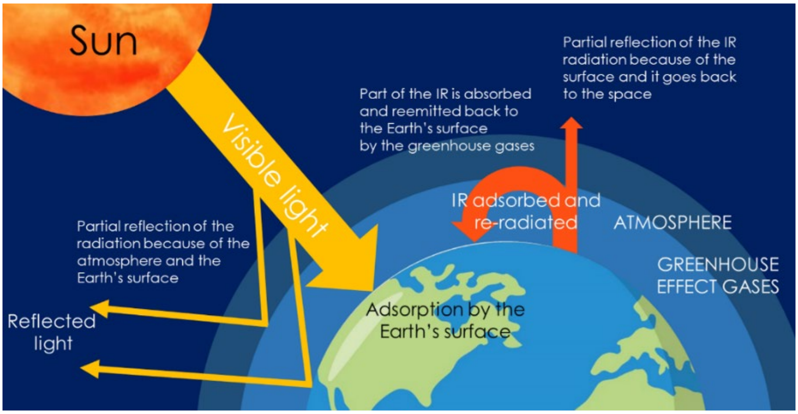

Figure 1.2. Irradiation flux Greenhouse effect.

In fact, evidences from satellite images measuring the surface of the North and South poles, as well as glaciers, reveal a considerable decrease in the Earth's surface covered by ice. In addition, satellites are also able to estimate the average temperature of the planet. It is clear that this temperature exchanges from point to point during the daytime, as a function of the season and also on the weather conditions, but at each instant in time, an average can be made. [4] This evidence has shown an increase in the average temperature of the planet over the years as indicated in Figure 1.3.

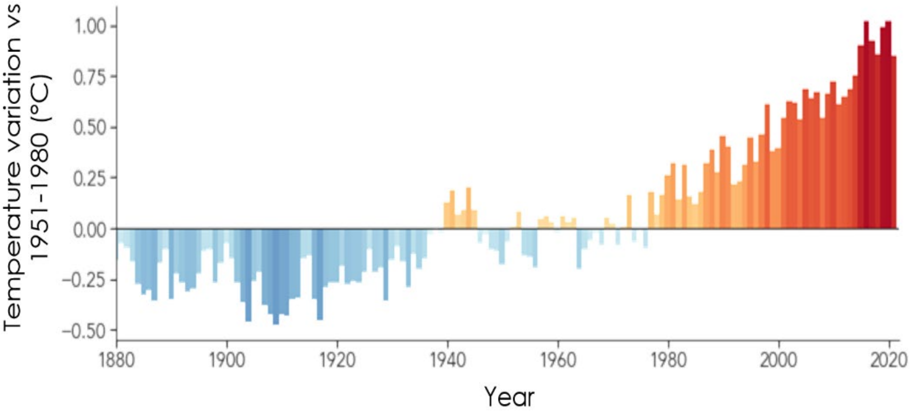

Figure 1.3. Global temperature changes taken the 1951-1980 mean value as reference.[4]

All this scientific evidence, combined with weather models, predicts that subsequent temperature increases will produce profound changes in the Earth's climate. This issue of climate change has been considered so important that the United Nations (UN) designated a panel of experts [5] to advise based on scientific data on countermeasures to deal with climate change and global warming. These UN initiatives on global climate change have resulted in several focus international submits, including Helsinki, Kyoto, and Paris. [6] In December 2019, in Paris, over 2000 countries, corresponding to more than 90% of the human population, agreed to decrease global CO_2 emissions to reduce it atmospheric concentrations to the levels before the 1970s. According to these models, this will produce by the end of the 21st century a temperature increase of the planet below 2 °C, which was considered the limit to avoid catastrophic changes at this time. [6] Figure 1.4 also illustrates the different scenarios of CO_2 emissions reduction. The Paris summit was followed by the Marrakesh agreement in 2020 and the strong commitment of the European Union to lead these changes. [6] The EU has launched a multibillion-euro program denoted as *Green Deal* to favor all the actions regarding climate change mitigation and social resilience against possible catastrophic events. [7]

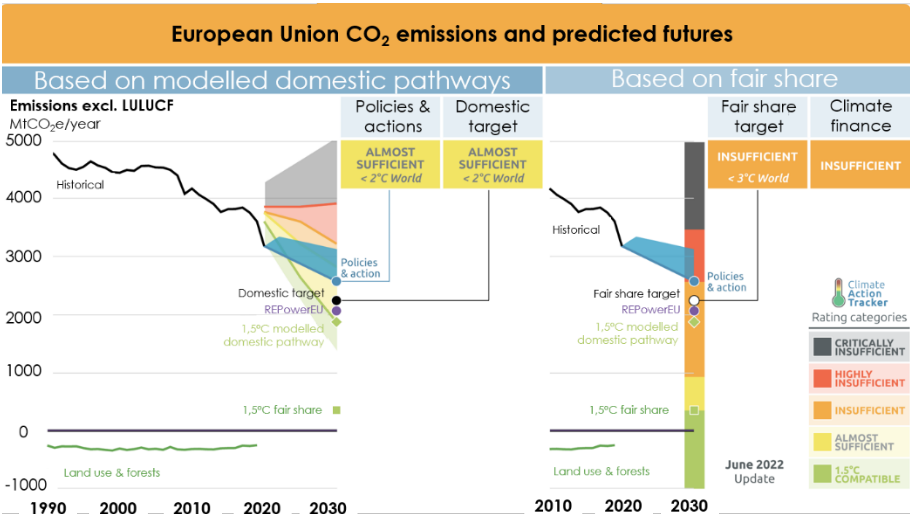

Figure 1.4. CO_2 emissions by the European Union and the different predicted futures temperature increase based on the climate models as function of atmosphere CO_2 emissions evolution, excluding LULUCF (Land Use, Land Use Chance and Forestry). [8]

1.2 Solar fuels

The main conclusion of the scientific evidence gathered by the UN climate panel is that the massive use of fossil fuels resulting in hundreds of GTon CO_2 emissions in a few years has increased the greenhouse effect of the atmosphere and, therefore, caused anthropogenic global warming. To reduce these CO_2 emissions is necessary to change the current primary energy source from hydrocarbon combustion to renewable and green alternative energy sources. Among various possible alternatives, the use of sunlight is considered to be one of the best options provided by scientific knowledge and the technology derived from is developed. [5] Figure 1.5 shows the estimated solar energy reaching the Earth and the various energy losses until reaching the Earth's solid land. As can be seen in this figure, just a minute use of solar energy, less than 1/10000 would be sufficient to provide the 10 TW estimated that is consumed by the whole of humankind on the planet. [9] It should be noted that sunlight energy is responsible for life on

Earth by natural photosynthesis in green algae, bacteria, and plants. The whole process of photosynthesis consumes a certain amount of energy compared to the amount of energy required currently to develop all the human activities on the planet. [9]

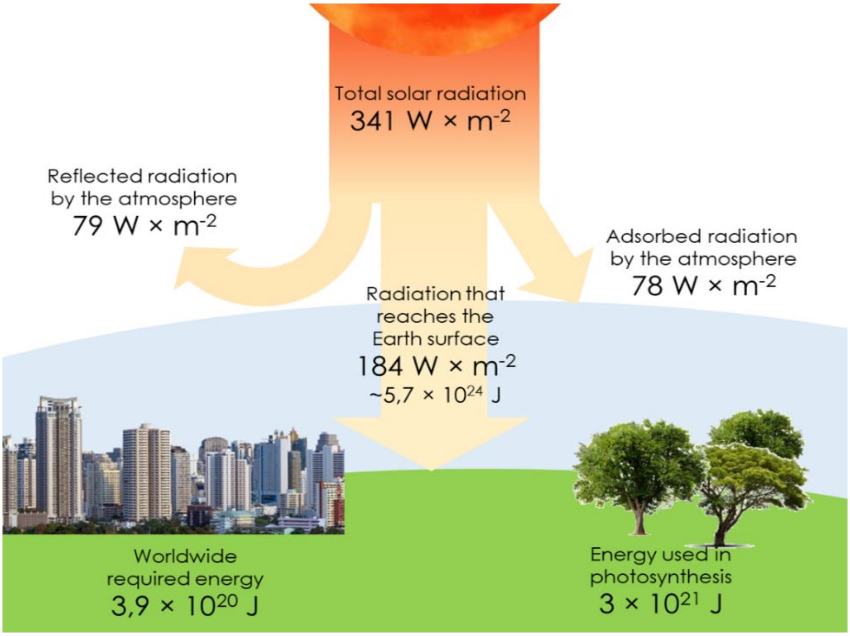

Figure 1.5. The estimated solar energy that reaches the Earth's surface and the values required for natural photosynthesis and human consumption.

However, sunlight as an energy source has several drawbacks that need to be overcome by the development of fundamental understanding and the corresponding technology. Sunlight power reaching the Earth is relatively weak (considered as 1000 W × m^{-2}), which makes its direct use impossible for many applications such as domestic use and transportation that require considerably higher power. [10] It is, therefore, necessary to accumulate sun energy for many hours and for a sufficiently large territory to have some practical applications. In addition, the problem is complicated by the period between day and night, and the influence of weather and seasons, among others, on the instantaneous solar power. One of the possibilities that have been developed and are reaching commercial stages is the conversion of sunlight into electricity. [11] But, one of the problems with this sunlight-produced electricity is the mismatch between production and consumption.

Therefore, it has to be stored somehow to be used according to consumers' demand, usually in electrical devices such as batteries or capacitors. [12] Therefore, one alternative is, provided that an efficient electrochemical process is developed, to use electricity to produce a chemical compound that can be used on demand as fuel. In this context, H_2, and products derived from CO_2 reduction, particularly methanol and formic acid, have been considered suitable fuels that can be, in principle, obtained by electrolysis. [13-16] One possible alternative to the conversion of the solar energy into electricity and, subsequently, implementing a new electrochemical process is the direct conversion of sunlight into fuels using a photocatalyst, that can absorb solar photons and transform them by any mechanism into chemical energy. [17-18] Moore and Gust coined the term *solar fuels* to denote those chemicals with possible use as energy storage compounds that are produced using solar light as the primary source by means of a photocatalyst. [19] In a certain way, the process mimics natural photosynthesis, in which sunlight is converted into ATP, NDAH, chemical potential, and O_2 from water. Figure 1.6 illustrates the photosynthetic system I and II located in the thylakoid membranes of green plants showing the flow of electrons and protons from water to biomolecules. [20]

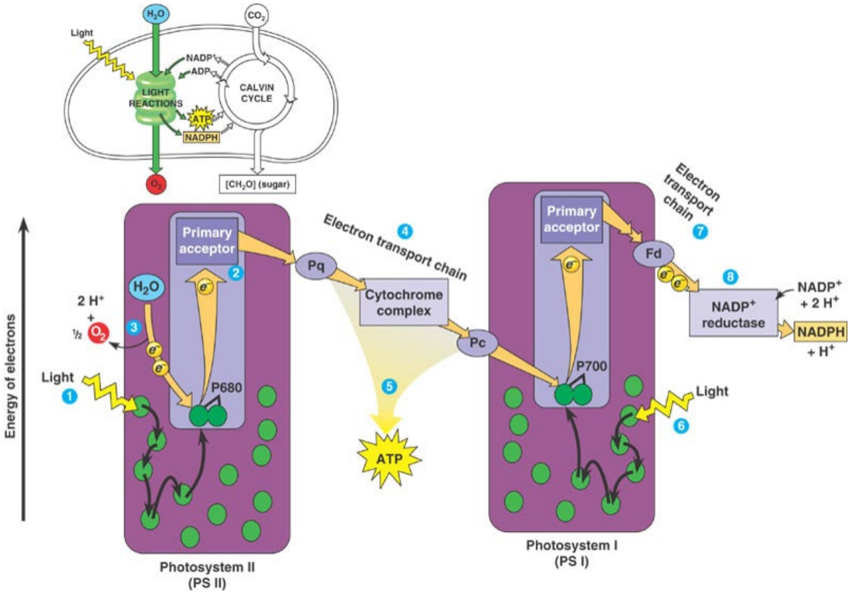

Figure 1.6. Photosystems I and II found in the thylakoid membrane which result in the production of biomolecules from CO_2 and H_2O.[20]

Although understanding of natural photosynthesis has progressed considerably in the last decades, the complexity of these biochemical processes is so large that we are still very far from preparing in the laboratory any system that could have similar spatial ordering energy level alignment, and durable structures to have any comparable photocatalytic process. Fortunately, the target of solar fuels is the preparation of simple molecules such as H_2 or CO that only require 2 bond breaks from the starting reagents. However, even though the target seems to be apparently simple and easy to achieve, we are still far from reaching an efficient photocatalyst. [21] Table 1.1 illustrates the current accepted solar fuels and their efficiencies.

Table 1.1. Current solar fuels and the reached efficiency of each process.

H_2 production from water splitting	**Solar-to-hydrogen efficiency**
Photoelectrochemical cells	19 % [21]
Photocatalysis	5 % [22]
Photovoltaic electrolysis	30 % [23]
CO_2 conversion in solar fuels	**Apparent Quantum Yield**
Photocatalytic production of methanol	6 % (λ=420 nm) [24]
Photocatalytic production of methane	10.2± 0.5% (450 nm)[25]
Other	**Efficiency**
Photocatalytic conversion of N_2 to NH_3	0.16 % [26]
Bio solar fuels using microorganisms	2.86 ± 0.38 % [27]

In 1970, as a consequence of the I Arab-Israeli War and the subsequent oil embargo on the US, the department of energy launched a quest among energy experts about which will be the ideal fuel. The conclusion of this quest was H_2, when produced from water and used in a fuel cell would not influence on the environment while being energetically very powerful, about 5 times the current hydrocarbon combustion, by mass unit. [28] This program identified several bottlenecks to implementing hydrogen technology, and the US DoE (United States Department of Energy) established a calendar with milestones to be achieved regarding the production of H_2 from water, its storage, and utilization. [29] Figure 1.7 summarizes these 3 steps that combined would result in a total neutral CO_2 footprint energy vector that could be used to store electricity, sunlight power, and transportation. US DoE already indicated that photocatalysis could be an ideal technology to obtain hydrogen. Unfortunately, after more than 50 years of intensive research, we are still far from any commercial application of hydrogen as an energy vector.

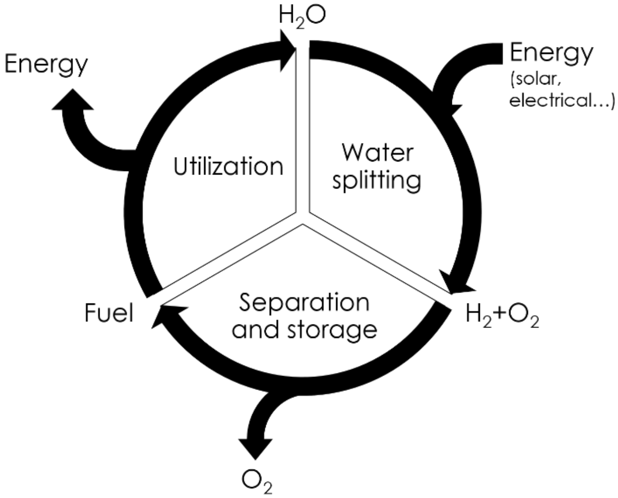

Figure 1.7. Steps to result in a neutral CO_2 footprint.

Another possibility as solar fuel that could be useful in the transitory period in which hydrocarbon combustion is used, consists of the capture of CO_2 from the fume gas and its conversion to fuel employing sunlight. [30] In certain ways, this would be a circular economy in which CO_2 is produced and reused compared to hydrogen production from water. CO_2 reduction by water is considerably more unfavorable from the thermodynamic and kinetic points of view. The reduction of CO_2 by water is denoted as *artificial photosynthesis* since these 2 reagents are also involved in natural photosynthesis producing O_2 and glucose. [20] Compared to hydrogen evolution from water, CO_2 reduction is a much more complex process, and this is reflected by the fact that the efficiency of the photocatalytic processes is at least 2 orders of magnitude lower than H_2 evolution. [31] The problem is that several products, including CO, formic acid, oxalic acid, methanol, and methane as well as C2+ products can be formed in photocatalytic CO_2 reduction. Since the number of protons and electrons for CO and formic acid formation is only 2, most of the photocatalytic processes report the formation of these two products. [31] In addition, since water is generally present, photocatalytic CO_2 reduction occurs simultaneously with hydrogen evolution, thus making mixture separation much more complex.

In the present thesis, chapters 3 to 6 will be focused on the preparation of metal-free, microporous graphitic carbons to be used as photocatalysts for H_2 evolution and CO_2 reduction. In photocatalysis, a material absorbs photons and generates a transient state of charge separation in which electrons move away from the place in which are formed, leaving behind a positive electron-hole as is summarized in Figure 1.8. [32] If electrons and holes reach the surface of the material, where the adsorbates are present, they can produce reduction and oxidation reactions, depending on the potentials required for these processes. [32]

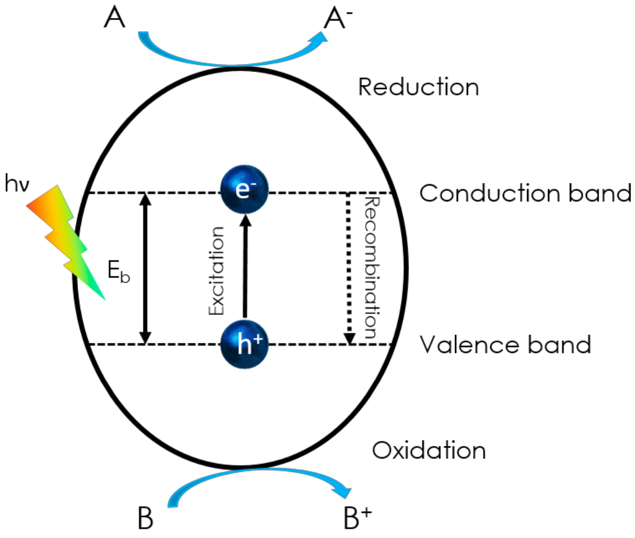

Figure 1.8. Elemental processes which take places when a semiconductor is irradiated with photons of energy higher than the semiconductor bandgap.

Since the discovery by Fujishima and Honda that TiO_2 when polarize in an electrode and illuminated by UV light can generate H_2 from water and reduce CO_2 to CO, in the 70s, there was an interest in studying new photocatalysts to expand the list of this photocatalyst and to understand the process. [33-34] Semiconducting metal oxides such as TiO_2, ZnO, CeO_2, WO_3, Fe_2O_3, and others are among the most studied photocatalyst. [35] Other family of well-studied photocatalysts are transition metal chalcogenides like CdS, ZnS, and

MoS_2 among others. [35] In fact, the field of photocatalysis has been dominated by metal-containing semiconductors. In some cases, metals are toxic, like Pb or Cd semiconductors, or they are critical raw materials, with low availability and high cost. [35] To tackle this problem, and in response to the demand for sustainability, there has been active research to develop metal-free photocatalysts. [36] The best example of this metal-free photocatalyst is the graphitic carbon nitride (g-C_3N_4), which can be easily obtained from melamine or dicyandiamide and exhibits a yellow color that responds under solar light. [37-38] Figure 1.9 illustrates the preparation of graphitic carbon nitride and its structure.

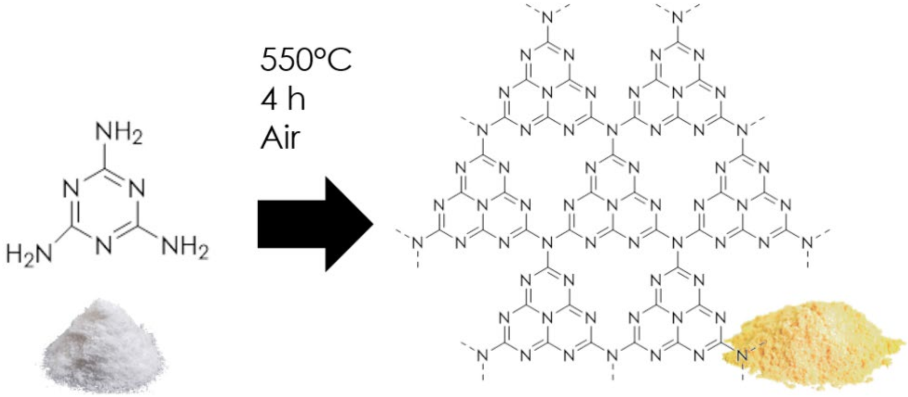

Figure 1.9. Graphitic carbon nitride preparation and its ideal structure.

Our group has made a contribution to this field by developing defective graphenes as photocatalyst. [39-42]

1.3 Polysaccharides as biomass waste converted into photocatalysts

In 2012, our group reported that pyrolysis of polysaccharides such as chitosan, alginate and carrageenan raise to graphitic carbons that can be subsequently exfoliated with a high yield to obtained doped defective graphenes. [42] The process is illustrated in Figure 1.10.

While pyrolysis of carbohydrates was known to form graphitic carbons, our contribution to the field was to show that, in comparison to graphite, which does not undergo exfoliation to graphene in a significant percentage, those materials derived from polysaccharides can be converted very efficiently into defective graphene. Considering that some polysaccharides form thin films of nanometric thickness without cracks, pinholes, and uniform thickness and very low rugosity, the polysaccharide pyrolysis process can be applied to both the preparation of defective graphenes as inks or thin films. [39]

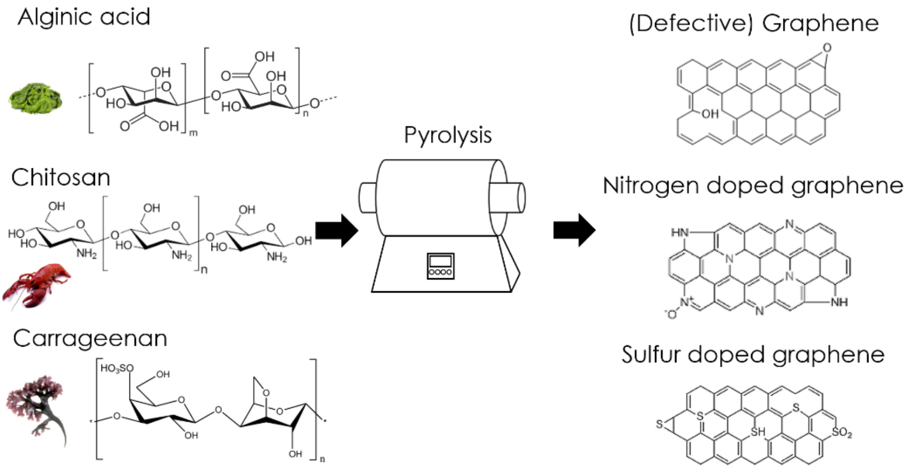

Figure 1.10. Defective graphenes obtained from the pyrolysis of the biomass.

Considering the hydroxyl groups present in polysaccharides, the process can be adapted to the formation of doped and co-doped defective graphenes. In some cases, like chitosan or carrageenan, the polysaccharide already contains nitrogen (chitosan, about 7 %) [42], or sulfur (carrageenan, about 9 %) [41] , and the pyrolytic process results in the N or S doping of the resulting graphene, as prove by chemical analysis which gives the amount of the heteroatoms in the material and XPS that provides the oxidation state and coordination sphere of the different families of dopant atoms. [41-42] Although is a specific surface technique that only proves a few nanometers of a material, the fact that graphene is a 2D nanomaterial with subnanometric thickness makes XPS an adequate analytical technique. In other cases, in which polysaccharides do not contain the heteroatoms, it is possible to form an ester of polysaccharide with the corresponding inorganic acid to introduce a dopant element. This strategy was used to introduce boron by forming the borate ester of alginate and phosphorous by forming the phosphate ester of alginate or chitosan.[39, 43] It is appropriate to remind that DNA and RNA are polyanionic polymers constituted by 5 membered-ring sugar forming the ester with phosphate bridging the position 3’ and 5’ of the sugar. [44]

Phosphate esters are, in fact, very common in carbohydrate chemistry. In this way, this is possible to introduce different heteroatoms, but also open the door to having co-doped graphenes with dopant elements in different proportions. Thus, for instance, Figure 1.11 illustrates the process of N and P co-doping by starting with chitosan, which is derivatized to the corresponding phosphate ester.

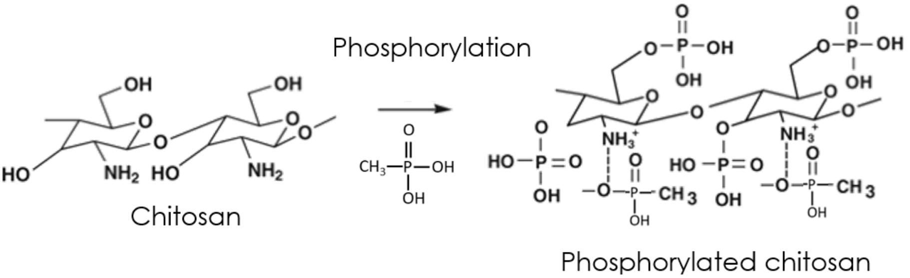

Figure 1.11. Synthesis of the phosphorylated chitosan.

1.3.1 Defective graphenes as catalysts and photocatalysts

While ideal graphene contains carbon atoms exclusively in sp^2 hybridization a hexagonal arrangement [45] is the void of any catalytic activity, and the presence of defects, acting as active sites, introduces centers on the graphene sheet that can promote chemical reactions. [46] These catalysts, based exclusively or predominantly on carbon and without metals, have opened a new research front on catalysis that has been named *carbocatalysis*. [47] While conventional catalysis is dominated by the use of transition metals as active sites, the scarcity of some of these metals and their high cost have been increasingly considered a major bottleneck in the area. The European Union has issued a list of critical raw materials whose scarcity and difficult availability can damage or impede certain sectors. [48] The catalysis and chemical industry is one of these sectors that heavily depend on critical raw materials. A program has been launched to decrease and minimize the dependence of Europe on this critical use of noble metal. [49] In this sense, the use of carbocatalysts is very appealing considering the sustainability of the lifecycle and the fact that most of the precursors are agricultural or marine waste and, therefore, their use represents an example of the circular economy. In the particular case that we are commenting on, chitosan derives from the skin of scrims and other crustaceous and can be converted into nitrogen-doped graphene with catalytic activity. [42] Our group has been active in the field of carbocatalysis and has contributed to several findings, including aerobic oxidation of saturated and unsaturated hydrocarbons and amines, Fenton catalysis, and selective hydrogenations by hydrogen activation. [47, 50-52] One important feature of carbocatalysts is that they can be engineered in the sheet and can be mimicked by organic molecules. In fact, carbocatalysis represents a bridge between organocatalysis and catalysis by transition metals. Figure 1.12 represents the type of active sites that have been proposed to be present in defective graphenes.

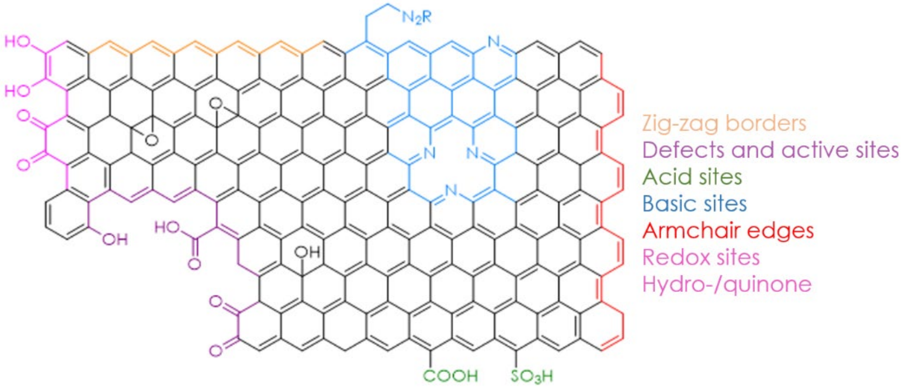

Figure 1.12. Defects found in graphenes which can act as catalytic sites.

Defects on graphenes also open the use of these materials in other types of catalysis such as electro and photocatalysis. [53] Typical catalytic processes use heat to activate substrates and reagents, allowing them to overcome the activation energy of the rated determining step in a reaction mechanism. Heat is normally obtained by the combustion of fossil fuels.[54]

In the current ongoing efforts to decarbonize industrial processes and energy consumption, other types of energy, different from heat, are becoming increasingly important. Particularly, renewable electricity from solar panels and wind turbines has made this energy one of the most important types that could become predominant in the coming years. [55] Also, when using electricity, activation barriers occurring in any reaction can be decreased by using appropriate catalysts that diminish the overpotential needed to perform the electrochemical process at a convenient rate. [56] Graphenes, being electrically conductive by having defects, have shown electrocatalytic activity for instance, in H_2 evolution reaction and water oxidation.[57] For these two electrochemical processes, the effect of dopants, particularly nitrogen and sulfur, in an appropriate configuration and loadings are crucial to obtain highly active materials. [41-42] Our group has also made contributions, showing that defective graphenes obtained from polysaccharides and their heterojunctions with other 2D materials can be appropriate electrocatalysts for these two processes. Figure 1.13 illustrates the contribution of the group with the use of large surface area superlattice heterojunctions of defective graphenes and MoS_2. [58]

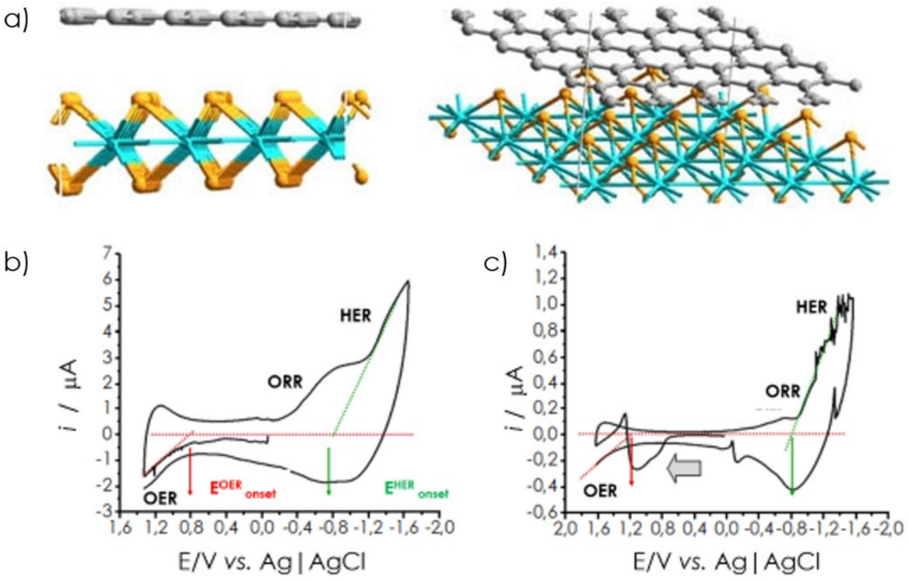

Figure 1.13. a) Two different views of superlattice heteorjunciton of graphene and Mo_2S; Cyclic voltamperometry of the heterojunction in b) superlattice structure and c) random configuration. [58]

Defects are also crucial in the use of defective graphenes in photocatalysis. While conductive graphenes are 0 band gap semiconductors due to the coincidence in the energy of the highest occupied molecular orbital, and the lowest unoccupied molecular orbital of ideal graphene, the presence of defects opens a gap between HOMO and LUMO energies, making possible electronic transitions from the HOMO to the LUMO. [59] These electronic transitions, together with the high mobility of electrons on graphene, result in a charge-separated transient state characteristic of photocatalysis by metallic semiconductors. As in the case of catalysis and electrocatalysis, the use of materials that can absorb photons and promote chemical reactions in the absence of metals is highly advantageous from the point of view of sustainability and good use of natural resources. [60] Introduction of N or P as dopant elements increases the response of doped graphenes as photocatalysts. [43, 50] Figure 1.14 shows the reported photocatalytic efficiency of P-doped graphene for H_2 evolution.

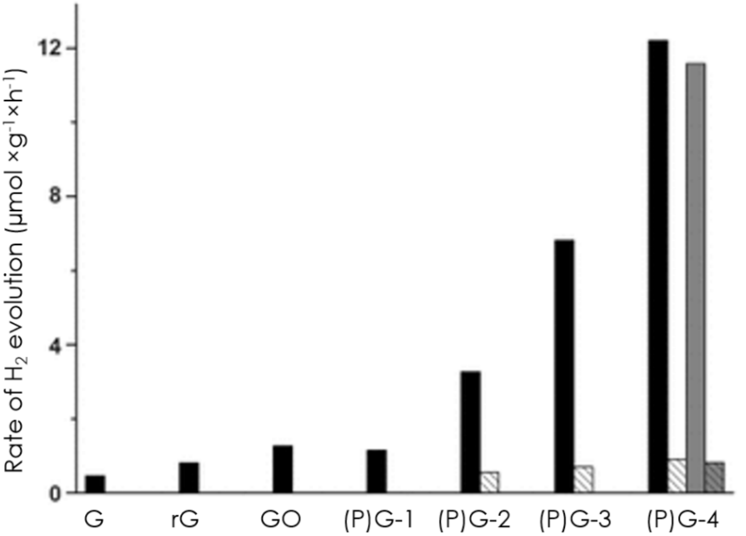

Figure 1.14. Photocatalytic activity for H_2 generation for samples of graphene, rG, GO, (P)G-1, (P)G-2, (P)G-3, (P)G-4, and (P)G-4 (third use) from an aqueous-methanol solution (30 v/v %). Catalyst concentration = 0.16 g × L^{-1}. Black: UV/Vis light; shaded gray: visible light (>390 nm), third use of the catalyst. [43]

Inorganic semiconductors frequently increase their efficiency as photocatalysts by the deposition of some additional material in the form of nanoparticles. The modification of semiconductors by these nanoparticles generally known as co-catalysts have been rationalized considering the role of promoting charge separation, acting these nanoparticles as charge carrier's buffers, or favoring product formation transferring electron or holes to the substrate efficiently. [61-64] Two types of co-catalysts, either metal nanoparticles or metal oxides, having different roles and activities have been reported, either independently or in cooperation to favor the efficiency of the photocatalytic processes. In the case of metal nanoparticles, particularly those stable to the ambient such as Pt or Au, electrons from the semiconductor can be easily stored in these nanoparticles, and subsequently, they can be transferred to the substrate.[65-66] On the contrary, metal oxides are more efficient in managing holes from the semiconductors. Particularly efficient oxides are IrO_2 and RuO_2, which facilitates water oxidation.[67-68] It has to be commented that many experimental parameters such as particle size, loading, and location, are crucial to achieve maximum photocatalytic efficiency. [62, 69-70] High loading of these co-catalysts is, generally, detrimental since they can absorb light, thus avoiding excitation of the semiconductor, and acting as recombination sites. In the last case, since electrons or holes are located at the co-catalysts, a large number of these charge carriers could cause the two charge carriers to coincide at one point, resulting in their recombination. [71] For instance, in TiO_2, electrons are located preferentially in crystallographic planes different from holes, but, a large concentration of Pt would transfer electrons from one plane to another, resulting in recombination. [72-73]

Our group has shown that, also in the case of defective graphenes, the deposition of Au or Cu_2O nanoparticles significantly increases the photocatalytic activity. [40, 74] The case of oriented Au nanoparticle strongly grafted on defective N-doped graphene is illustrated in Figure 1.15, in which the photocatalytic efficiency for solar or visible light H_2 evolution is also presented, as well as overall water splitting is presented.

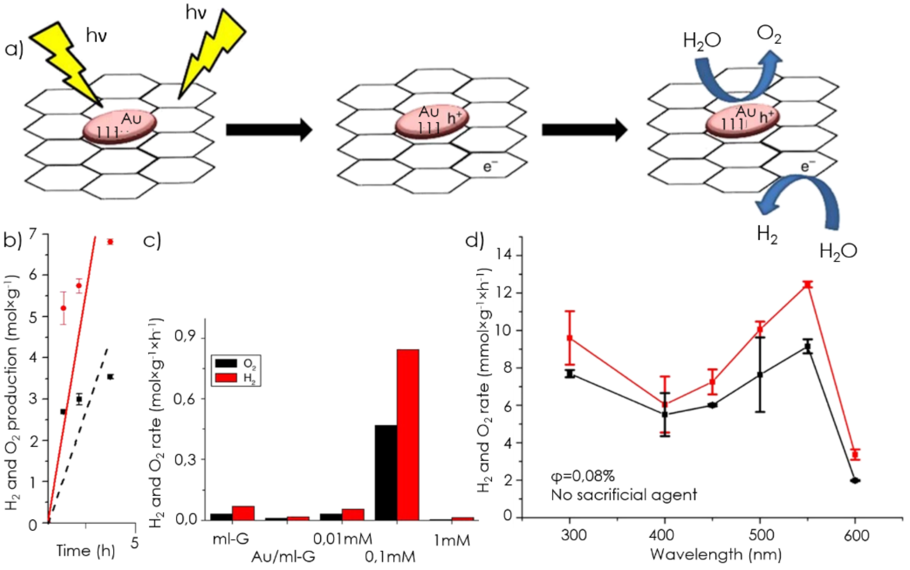

Figure 1.15. a) Proposed mechanism for the overall water splitting reaction, b) H_2 and O_2 evolution under irradiation, c) H_2 and O_2 production under different concentrations of Au, d) Overall water splitting using monochromatic irradiation and calculated apparent quantum yield. [40]

1.3.2 Microporous ordered graphitic carbons

The previous comments on the properties of defective graphenes as carbocatalysts and electro/photocatalysts refer to the inks of suspended graphene sheets. While these materials exhibit remarkable catalytic properties, they are essentially flat flexible catalysts with 2D morphology offering a large surface area.

While the surface area is important in heterogeneous catalysis in which substrate and reagents interact with the active sites located in the catalysts, a type of solids that have found wide application as catalysts are microporous materials. Microporous solids, such as zeolites and MOFs not only offer a large surface area with accessible active sites, but the presence of pores introduces additional effects highly important in catalysis like a defining polarity of the environment around the active sites and the so-called confinement effect. [75-76] The confinement effect refers to the increasing catalytic activity frequently observed when a site of a given structure, is incorporated inside a channel or case. Confinement effects are particularly remarkable when the dimension of the pores is close to the diameter of the substrate. In this case, the interaction of the walls of the micropores with the occluded substrate increases the reactivity of the latter. Figure 1.16 provides an example of this confinement effect.

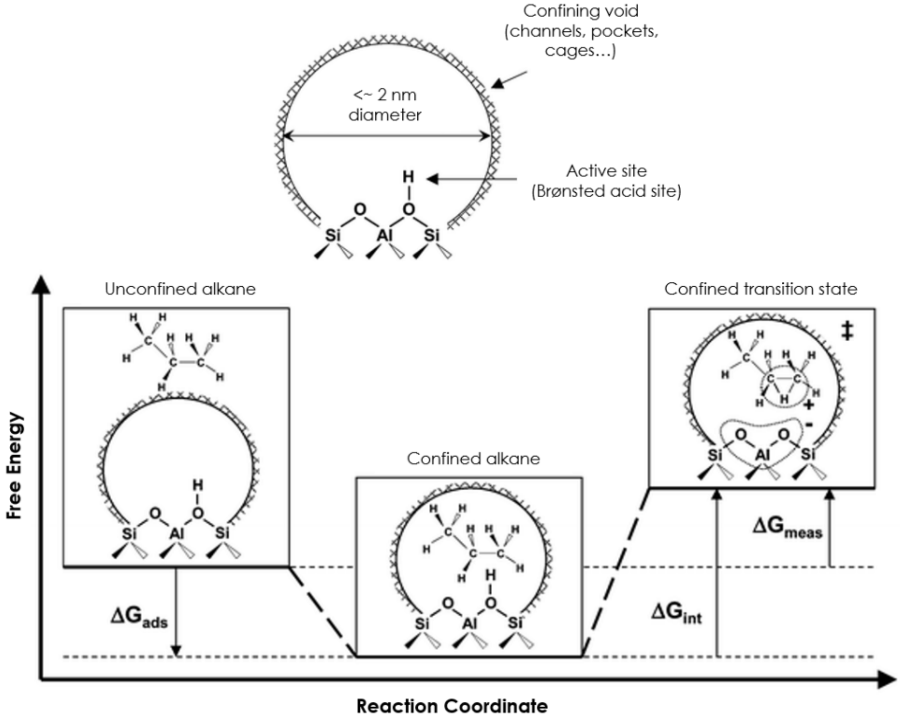

Figure 1.16. 2D confined active site in a zeolite, and the scheme of an alkane activation with the Gibbs free energy versus reaction coordinate diagram for alkane cracking., where the differences between the same confined transition state and either unconfined (ΔG_{meas}) or the confined alkane reactants (ΔG_{int}) are presented. [77]

Due to the importance of regular porosity on catalysis, there have been serious efforts to develop carbons' regular porosity.

Two general strategies, either hard templating or soft templating are generally implemented to obtain porous materials with regular and uniform pore-size distribution. In the hard templation method, some materials, such as silica or polystyrene with well-defined spherical shapes, and the same dimension, are used and the material is formed around these regular spheres. After the removal of the hard template by appropriate chemical or thermal treatment, an empty space is generated with exactly the same dimension. [78] Hard templation is very useful to obtain pores in the dimension of hundreds of nanometers or larger. This is because silica spheres obtained by stablished method are commercially available. Our group prepared carbon sponges with a diameter of 80 nm by using silica spheres that were coated with alginate or chitosan. Subsequent pyrolysis renders the graphene material but has the morphology with strictly regular spherical cavities.[78-79] Figure 1.17 presents selected reported images of this type of material.

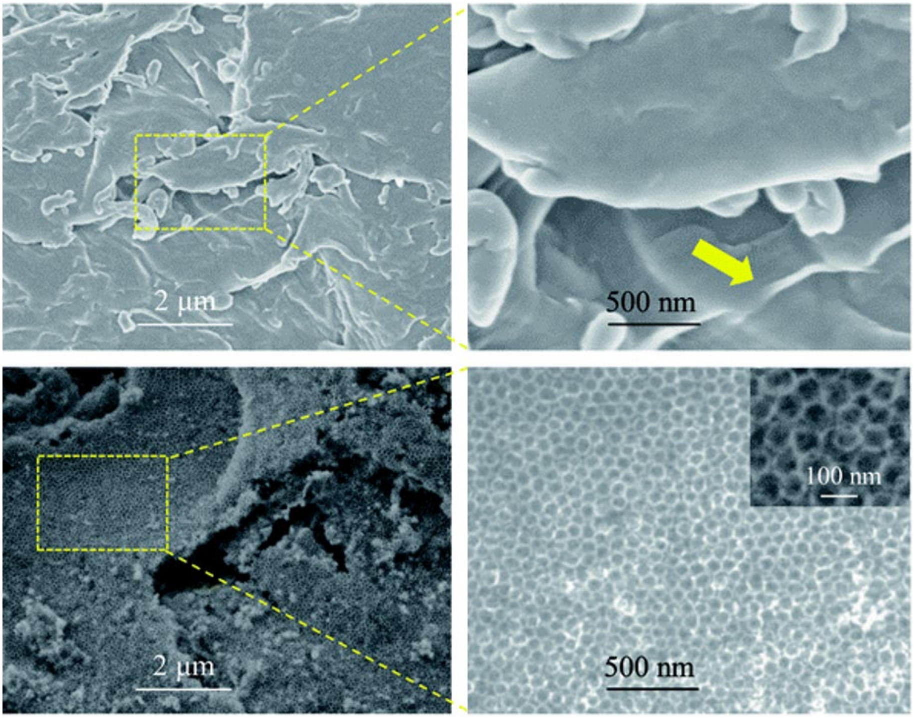

Figure 1.17. SEM images of 3D graphene sponges.[79]

However, hard templation to obtain pores smaller than 100 nm is uncommon. For this size region, even going lower to nanometric dimensions, soft templation appears to be a more common strategy for the preparation of porous silica aluminophosphates and zeolites. [80] However, this soft templation has not been applied for the preparation of carbon materials. For this reason, carbon material having regular micropores in the nanometric scale are very uncommon and has not been reported so far.

Considering that as previously commented some natural polysaccharides are filmogenic materials meaning that they adopt the form of the surface in which these polymers are supported, it is one of the targets of the present thesis to determine if soft templation can also be applied to natural polysaccharides following a templation mechanism similar to those generally accepted for the synthesis of zeolites and other aluminosilicates. The soft templation mechanism is illustrated in Figure 1.18.

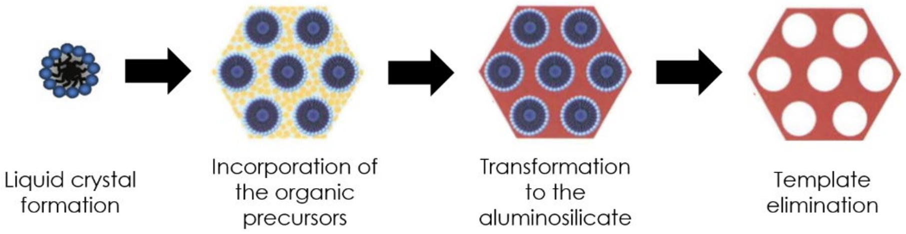

Figure 1.18. Soft templation mechanism.

This mechanism is based on the self-aggregation of an organic molecule in water forming well-defined aggregates around which start to nucleate the inorganic material. It occurs to us that since natural polysaccharide a filmogenic with subnanometric rugosity they could also adapt the form of the spontaneous aggregates formed from some common organic templates. In a subsequent step, the template polysaccharide, having already the information of the porosity imported from the templates, will be transformed into a graphitic carbon. This strategy original in our view will be the subject of Chapter 3 of the present thesis.

The aim is to show that soft templation can also be applied to these natural organic polymers and by using templates known in the literature for zeolite synthesis, graphitic carbons with regular microporosity can be obtained. Specifically, two templates in which the group has experience are the tetraethylammonium, which is used in beta zeolite, and hexamethyleneimine, used in the synthesis of MCM 22 and ITQ 2. [81-82] Figure 1.19 shows the structure of these organic templates and the resulting zeolites derived from soft templation. The target will be to mimic this process using alginate or chitosan, making use of the ability to adopt different shapes.

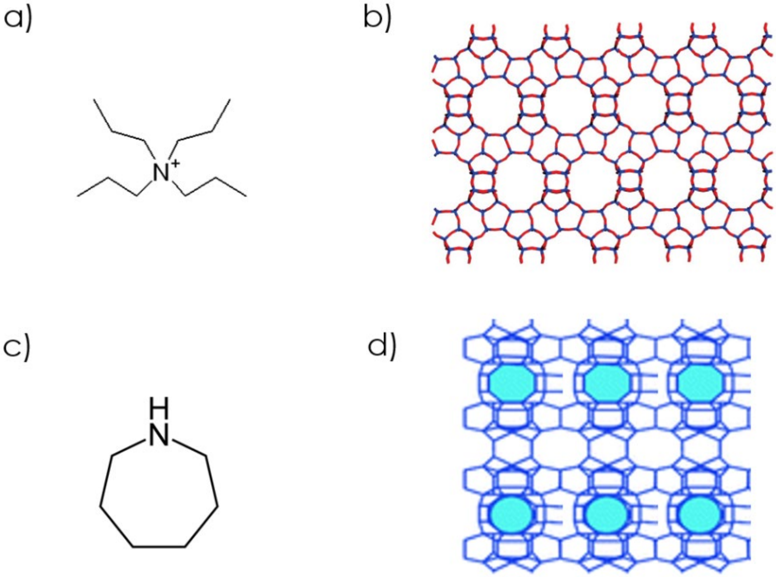

Figure 1.19. Structures of a) tetraethylamonium (TEA), b) beta zeolite, c) hexamethyleneimine (HMI) and d) MCM-22 zeolite.

1.3.3 Cyclodextrins

The past work of our group was mainly polymeric saccharides that have appropriate physical properties to stand temperature without sublimation until the temperature is high enough to promote chemical transformations that will end up in the graphitization of the material. [41-42, 83] Other organic molecules are not suitable for analogous graphitization processes since they become volatile and are swifted by the inert gas flow out of the oven. Evaporation of organic molecules is the main limitation to obtaining carbon residues in many cases.

One particular case that was not explored in the literature was the case of cyclodextrins. Cyclodextrins are cyclic oligomers of 6, 7, or 8 glucose units in the case of α-, β-, and γ-cyclodextrins. These cyclic molecules have a truncated-cone geometry with the height of the dimension of the glucose and the diameter depending on the number of glucopiranosil units.[84-85] Figure 1.20 shows the structure and dimensions of these molecules. Cyclodextrins are easily obtained in large quantities by enzymatic hydrolysis of starch and other polysaccharides. [86]

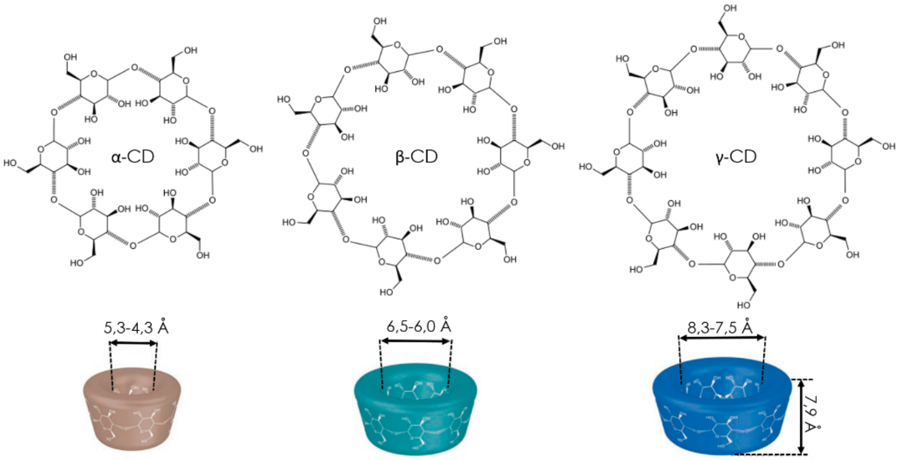

Figure 1.20. Structure and dimensions of α-, β-, and γ- cyclodextrin. [87]

Cyclodextrins are highly soluble in water due to the abundant presence of polar hydroxyl groups, pointing to the outer surface of the molecules. However, the interior of the cyclodextrins is considerably more apolar, and the hollow geometry allows the inclusion in the interior of certain organic molecules. In this way, cyclodextrins have been used as monomers to form host-guest complexes in water, in which an apolar molecule, typically an aromatic hydrocarbon insoluble in water, assemblies with dissolved cyclodextrins by being accommodated in the interior of the oligosaccharide capsule. [86, 88] Table 1.2 illustrates several known examples of host-guest complexes using cyclodextrins. The tight fit of the guest inside cyclodextrins and the appropriate polarity are the driving forces determining the binding constant between cyclodextrin and the guest.

Table 1.2. Examples of host-guest cyclodextrin compounds.[89]

Extract/Drug	Compound	Effect
Shiitake	Cyclic sulfur compound	Flavor retention
Thermally processed foods	l-menthol	Flavor retention
Soy protein	Phenylalanine, tryptophan, tyrosine, isoleucine, proline, histidine	Reduce bitter taste
Caffeine	β and γ-cyclodextrin linked to chitosan	Bitter masking properties
Garlic oil	Antimicrobial compounds	Protection against oxidation to keep the antimicrobial properties
Meiac	Cephalosporin	Protection of the antibiotic
Nicorette	Nicotine	Slow releasing for smoking cessation
Ibuprofen	Inclusion of the complexes with the non-polar molecule	Increase the solubility
Omeprazole	Prevention of drug-drug or drug-additive interaction	Prevention incompatibility
Curcumin	Anti-inflammatory, antioxidant and antitumor compounds	Drug release in 2 steps

Cyclodextrins have a high melting point of about 300 °C. [85] This high temperature is close to the temperature at which the hidrazion of sugar and humins formation starts. In addition, the conical geometry of cyclodextrins has been reported to be responsible for the self-assembly of these cyclic molecules forming tubes of a few cyclodextrin units. [90] Figure **1.21** illustrates cyclodextrin self-assembling as a consequence of the different diameters of the tube opening of the molecule and the appearance of hydrogen bond interactions between one molecule and the neighbor.

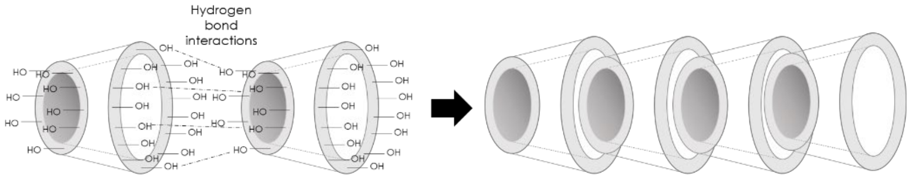

Figure 1.21. Self-assembling of the cyclodextrin (β-cyclodextrin in this example).

Pyrolysis of cyclodextrins has been reported in the literature but the focus was placed on the evolution of volatile products and not on the nature of the resulting residue. [91] Figure 1.22 shows some of the products that have been detected as arising cyclodextrins.

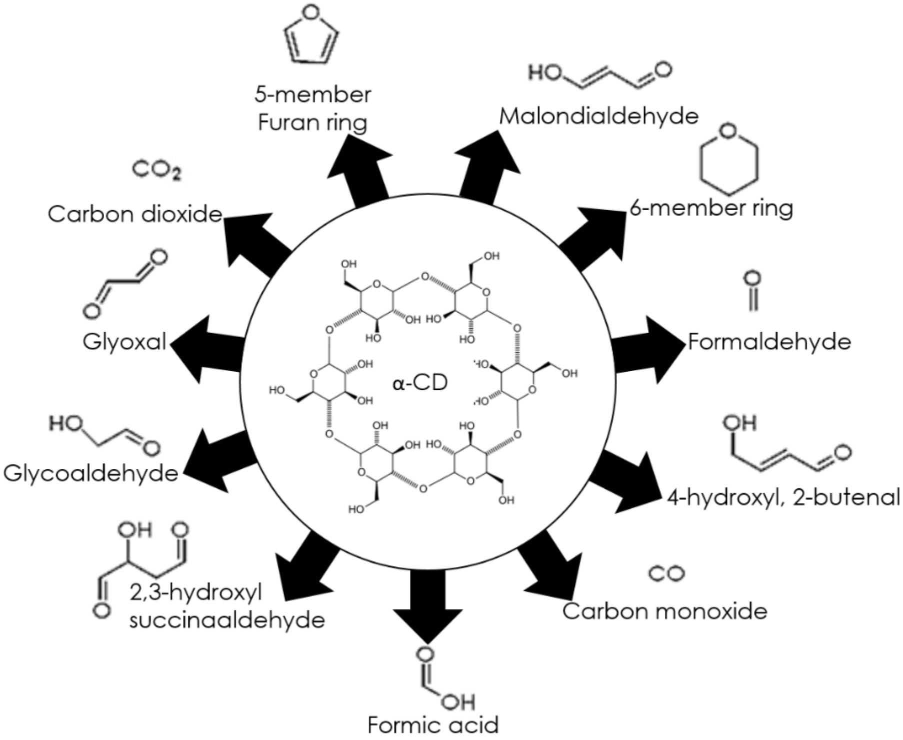

Figure 1.22. Volatile products detected in the pyrolysis of α-cyclodextrin. [92]

Considering the molecular of cyclodextrins, and their tendency to self-assemble, it occurs to us that, in the absence of any template, these organic capsules will form defined particles with microporosity. In this sense, the resulting material could be similar to those arising from the soft templation method using organic quaternary ammonium templates as previously commented. Subsequent pyrolysis could render the corresponding graphitic carbons. Our group recently demonstrated this template-free synthesis of microporous graphitic carbons and the resulting structured microporous materials were used as carbocatalysts to promote aerobic oxidation reactions and as photocatalyst for hydrogen evolution. [93-94] Figure 1.23 illustrates some of the reactions that have been studied with these carbons derived from cyclodextrins.

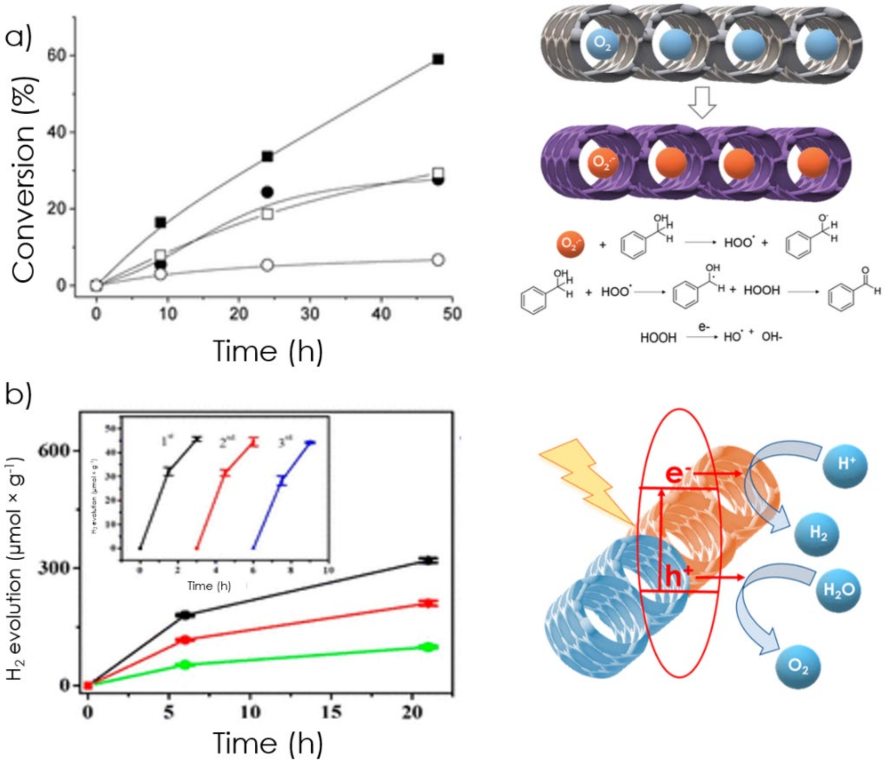

Figure 1.23. a) Conversion plots for aerobic oxidation of benzyl alcohol usign microporous graphitic carbon from α- (■), β- (□), and γ-cyclodextrin (●), and active carbon (○) for comparison. [93] b) H_2 evolution using TEOA as electron donor in the photocatalytic irradiation using microporous graphitic carbon from the α- (black), β- (red), and γ- cyclodextrin (green) as photocatalyst. [94]

Continuing with this line of research, it would be interesting if doping with heteroatoms can increase the activity of these carbons. In the case of carbon residue derived from α-cyclodextrin, combustion chemical analysis shows that the material is constituted almost by carbon with a minimum amount of hydrogen. It could be that the presence of heteroatoms such as nitrogen and phosphorous could increase the activity of these materials, for instance, in photocatalysis, for which we have commented previously that N or P-doping of graphene renders highly efficient photocatalyst. In this way, very recently we reported that N-doping increases the photocatalytic activity of cyclodextrins for overall water splitting. It remains to determine if P-doping can lead to the same or even higher photocatalytic activity. Thus, the target of Chapter 4 would be the preparation of P-doped microporous graphitic carbons derived from cyclodextrins pyrolysis and compared its photocatalytic activity for H_2 evolution, O_2 evolution, and overall water splitting with that of similar materials without doping. The purpose is to adjust the band energies aligned with the redox potential of water potential of reduction and oxidation to make the photocatalytic process more efficient.

Besides overall water splitting resulting in the generation of H_2 from water without any additives, and as commented in the Introduction, photocatalytic CO_2 reduction is also a very important process in the field of solar fuels. Up to now, no data on the photocatalytic CO_2 reduction activity of microporous graphitic carbons have been reported. Therefore, to advance the knowledge of the performance and potential applications of microporous graphitic carbons, it would be important to evaluate the activity of these materials for photocatalytic CO_2 reduction, determining efficiency and reaction products. This would be the target of Chapter 5, in which a comparison of the photocatalytic CO_2 performance of microporous graphitic carbons as a function of the dimension of the cyclodextrin precursor and the presence or absence of heteroatoms will be investigated.

The final chapter of the present thesis will use these graphitic carbons derived from cyclodextrins to act as catalysts in other fields. Particularly, in Chapter 6 we will study the possibility to extend the application of these materials as (photo)electrocatalysts for the challenging reaction of the CO_2 reduction. In this case, we will check the influence on the catalytic performance of the presence of doping elements previously characterized and applied on photocatalysis. These results are obtained during the internship in the CEMHTI (France) under the supervision of Prof. Conchi O. Ania.

Overall, the present research is aimed at the advance of the field of carbocatalysis and carbo-photocatalysis as alternative to the use of conventional transition metal catalysts. The use of carbon materials present advantages in terms of wise use of natural resources, sustainability and less environmental impact of catalysis. The carbon materials having porosity that will be prepared in the present in this Thesis will be evaluated as catalyst for aerobic oxidation, a reaction of large industrial importance, and as photocatalyst for H_2 evolution or CO_2 reduction.

1.4 References

1. Ritchie, H. R., Max; and Rosado Pablo CO_2 and Greenhouse Gas Emissions. https://ourworldindata.org/co2-and-other-greenhouse-gas-emissions (accessed 02/10/2022).

2. Marcott, S. A.; Bauska, T. K.; Buizert, C.; Steig, E. J.; Rosen, J. L.; Cuffey, K. M.; Fudge, T. J.; Severinghaus, J. P.; Ahn, J.; Kalk, M. L.; McConnell, J. R.; Sowers, T.; Taylor, K. C.; White, J. W. C.; Brook, E. J., Centennial-scale changes in the global carbon cycle during the last deglaciation. *Nature* **2014,** *514* (7524), 616-619.

3. Bauska, T. K. Ice cores and climate change. https://www.bas.ac.uk/data/our-data/publication/ice-cores-and-climate-change/#:~:text=Ice%20cores%20provide%20direct%20information,change%20abruptly%20under%20some%20circumstances. (accessed 22/09/2022).

4. NASA World of Change: Global Temperatures. https://earthobservatory.nasa.gov/world-of-change/global-temperatures#:~:text=According%20to%20an%20ongoing%20temperature,1.9%C2%B0%20Fahrenheit)%20since%201880. (accessed 22/09/2022).

5. Nations, U. The Intergovernmental Panel on Climate Change. https://www.ipcc.ch/ (accessed 22/09/2022).

6. Poulopoulos, S. G., Chapter 2 - Atmospheric Environment. In *Environment and Development*, Poulopoulos, S. G.; Inglezakis, V. J., Eds. Elsevier: Amsterdam, 2016; pp 45-136.

7. Comission, E. A European Green Deal. https://ec.europa.eu/info/strategy/priorities-2019-2024/european-green-deal_en (accessed 02/10/2022).

8. New Climate Institute, C. a. Climate Action Tracker. https://climateactiontracker.org/countries/ (accessed 02/10/2022).

9. Towler, B. F., Chapter 8 - Solar Power. In *The Future of Energy*, Towler, B. F., Ed. Academic Press: Boston, 2014; pp 161-185.

10. Lindsay, R. Climate and Earth's Energy Budget. https://earthobservatory.nasa.gov/features/EnergyBalance/page2.php (accessed 02/10/2022).

11. Phillips, L., 9 - Solar energy. In *Managing Global Warming*, Letcher, T. M., Ed. Academic Press: 2019; pp 317-332.

12. Biswas, A.; Swain, S.; Maiti, D. K., Chapter 22 - Eco-friendly cost-effective energy-storage device for the benefit of society. In *Nano Tools and Devices for Enhanced Renewable Energy*, Devasahayam, S.; Hussain, C. M., Eds. Elsevier: 2021; pp 567-583.

13. Zhu, J.; Hu, L.; Zhao, P.; Lee, L. Y. S.; Wong, K.-Y., Recent Advances in Electrocatalytic Hydrogen Evolution Using Nanoparticles. *Chemical Reviews* **2020,** *120* (2), 851-918.

14. Deng, C.; Toe, C. Y.; Li, X.; Tan, J.; Yang, H.; Hu, Q.; He, C., Earth-Abundant Metal-Based Electrocatalysts Promoted Anodic Reaction in Hybrid Water Electrolysis for Efficient Hydrogen Production: Recent Progress and Perspectives. *Advanced Energy Materials* **2022,** *12* (25), 2201047.

15. Albo, J.; Alvarez-Guerra, M.; Castaño, P.; Irabien, A., Towards the electrochemical conversion of carbon dioxide into methanol. *Green Chemistry* **2015,** *17* (4), 2304-2324.

16. Adegoke, K. A.; Radhakrishnan, S. G.; Gray, C. L.; Sowa, B.; Morais, C.; Rayess, P.; Rohwer, E. R.; Comminges, C.; Kokoh, K. B.; Roduner, E., Highly efficient formic acid and carbon dioxide electro-reduction to alcohols on indium oxide electrodes. *Sustainable Energy & Fuels* **2020,** *4* (8), 4030-4038.

17. Kumar, P.; Dhand, C.; Dwivedi, N.; Singh, S.; Khan, R.; Verma, S.; Singh, A.; Gupta, M. K.; Kumar, S.; Kumar, R.; Srivastava, A. K., Graphene quantum dots: A contemporary perspective on scope, opportunities, and sustainability. *Renewable and Sustainable Energy Reviews* **2022,** *157*, 111993.

18. Ezendam, S.; Herran, M.; Nan, L.; Gruber, C.; Kang, Y.; Gröbmeyer, F.; Lin, R.; Gargiulo, J.; Sousa-Castillo, A.; Cortés, E., Hybrid Plasmonic Nanomaterials for Hydrogen Generation and Carbon Dioxide Reduction. *ACS Energy Letters* **2022,** *7* (2), 778-815.

19. Gust, D.; Moore, T. A.; Moore, A. L., Solar Fuels via Artificial Photosynthesis. *Accounts of Chemical Research* **2009,** *42* (12), 1890-1898.

20. Gao, J.; Wang, H.; Yuan, Q.; Feng, Y., Structure and Function of the Photosystem Supercomplexes. *Frontiers in plant science* **2018,** *9*, 357.

21. Cheng, W.-H.; Richter, M. H.; May, M. M.; Ohlmann, J.; Lackner, D.; Dimroth, F.; Hannappel, T.; Atwater, H. A.; Lewerenz, H.-J., Monolithic Photoelectrochemical Device for Direct Water Splitting with 19% Efficiency. *ACS Energy Letters* **2018,** *3* (8), 1795-1800.

22. Li, Y.; Wang, Z.; Wang, Y.; Kovács, A.; Foo, C.; Dunin-Borkowski, R. E.; Lu, Y.; Taylor, R. A.; Wu, C.; Tsang, S. C. E., Local magnetic spin mismatch promoting photocatalytic overall water splitting with exceptional solar-to-hydrogen efficiency. *Energy & Environmental Science* **2022,** *15* (1), 265-277.

23. Jia, J.; Seitz, L. C.; Benck, J. D.; Huo, Y.; Chen, Y.; Ng, J. W. D.; Bilir, T.; Harris, J. S.; Jaramillo, T. F., Solar water splitting by photovoltaic-electrolysis with a solar-to-hydrogen efficiency over 30%. *Nature Communications* **2016,** *7* (1), 13237.

24. Wang, Y.; Godin, R.; Durrant, J. R.; Tang, J., Efficient Hole Trapping in Carbon Dot/Oxygen-Modified Carbon Nitride Heterojunction Photocatalysts for Enhanced Methanol Production from CO2 under Neutral Conditions. *Angewandte Chemie International Edition* **2021,** *60* (38), 20811-20816.

25. Wang, J.-W.; Jiang, L.; Huang, H.-H.; Han, Z.; Ouyang, G., Rapid electron transfer via dynamic coordinative interaction boosts quantum efficiency for photocatalytic CO2 reduction. *Nature Communications* **2021,** *12* (1), 4276.

26. Shiraishi, Y.; Kishimoto, T.; Tanaka, S.; Hirai, T., Photocatalytic Dinitrogen Fixation with Water on High-Phosphorus-Doped Carbon Nitride with Surface Nitrogen Vacancies. *Langmuir* **2022,** *38* (23), 7137-7145.

27. Zhang, H.; Liu, H.; Tian, Z.; Lu, D.; Yu, Y.; Cestellos-Blanco, S.; Sakimoto, K. K.; Yang, P., Bacteria photosensitized by intracellular gold nanoclusters for solar fuel production. *Nature Nanotechnology* **2018,** *13* (10), 900-905.

28. Yip, H. L.; Srna, A.; Yuen, A. C. Y.; Kook, S.; Taylor, R. A.; Yeoh, G. H.; Medwell, P. R.; Chan, Q. N., A Review of Hydrogen Direct Injection for Internal Combustion Engines: Towards Carbon-Free Combustion. *Applied Sciences* **2019,** *9* (22), 4842.

29. Energy, U. S. D. o. Hydrogen and our energy future. https://www.energy.gov/eere/fuelcells/downloads/hydrogen-our-energy-future (accessed 02/10/2022).

30. Wang, X.; Song, C., Carbon Capture From Flue Gas and the Atmosphere: A Perspective. *Frontiers in Energy Research* **2020,** *8*.

31. Tu, W.; Zhou, Y.; Zou, Z., Photocatalytic Conversion of CO2 into Renewable Hydrocarbon Fuels: State-of-the-Art Accomplishment, Challenges, and Prospects. *Advanced Materials* **2014,** *26* (27), 4607-4626.

32. Yanagi, R.; Zhao, T.; Solanki, D.; Pan, Z.; Hu, S., Charge Separation in Photocatalysts: Mechanisms, Physical Parameters, and Design Principles. *ACS Energy Letters* **2022,** *7* (1), 432-452.

33. Fujishima, A.; Honda, K., Electrochemical Photolysis of Water at a Semiconductor Electrode. *Nature* **1972,** *238* (5358), 37-38.

34. Hashimoto, K.; Irie, H.; Fujishima, A., TiO₂Photocatalysis: A Historical Overview and Future Prospects. *Japanese Journal of Applied Physics* **2005,** *44* (12), 8269-8285.

35. Hernández-Alonso, M. D.; Fresno, F.; Suárez, S.; Coronado, J. M., Development of alternative photocatalysts to TiO2: Challenges and opportunities. *Energy & Environmental Science* **2009,** *2* (12), 1231-1257.

36. Wang, Z.; Li, C.; Domen, K., Recent developments in heterogeneous photocatalysts for solar-driven overall water splitting. *Chemical Society Reviews* **2019,** *48* (7), 2109-2125.

37. Wang, X.; Maeda, K.; Thomas, A.; Takanabe, K.; Xin, G.; Carlsson, J. M.; Domen, K.; Antonietti, M., A metal-free polymeric photocatalyst for hydrogen production from water under visible light. *Nature materials* **2009,** *8* (1), 76-80.

38. Wang, X.; Blechert, S.; Antonietti, M., Polymeric Graphitic Carbon Nitride for Heterogeneous Photocatalysis. *ACS Catalysis* **2012,** *2* (8), 1596-1606.

39. Esteve-Adell, I.; He, J.; Ramiro, F.; Atienzar, P.; Primo, A.; García, H., Catalyst-free one step synthesis of large area vertically stacked N-doped graphene-boron nitride heterostructures from biomass source. *Nanoscale* **2018,** *10* (9), 4391-4397.

40. Mateo, D.; Esteve-Adell, I.; Albero, J.; Royo, J. F. S.; Primo, A.; Garcia, H., 111 oriented gold nanoplatelets on multilayer graphene as visible light photocatalyst for overall water splitting. *Nature Communications* **2016,** *7* (1), 11819.

41. Dhakshinamoorthy, A.; Latorre-Sanchez, M.; Asiri, A. M.; Primo, A.; Garcia, H., Sulphur-doped graphene as metal-free carbocatalysts for the solventless aerobic oxidation of styrenes. *Catalysis Communications* **2015,** *65*, 10-13.

42. Primo, A.; Atienzar, P.; Sanchez, E.; Delgado, J. M.; García, H., From biomass wastes to large-area, high-quality, N-doped graphene: catalyst-free carbonization of chitosan coatings on arbitrary substrates. *Chemical Communications* **2012,** *48* (74), 9254-9256.

43. Latorre-Sánchez, M.; Primo, A.; García, H., P-Doped Graphene Obtained by Pyrolysis of Modified Alginate as a Photocatalyst for Hydrogen Generation from Water–Methanol Mixtures. *Angewandte Chemie International Edition* **2013,** *52* (45), 11813-11816.

44. Watson, J. D.; Crick, F. H. C., Molecular Structure of Nucleic Acids: A Structure for Deoxyribose Nucleic Acid. *Nature* **1953,** *171* (4356), 737-738.

45. Novoselov, K. S.; Geim, A. K.; Morozov, S. V.; Jiang, D.; Katsnelson, M. I.; Grigorieva, I. V.; Dubonos, S. V.; Firsov, A. A., Two-dimensional gas of massless Dirac fermions in graphene. *Nature* **2005,** *438* (7065), 197-200.

46. Fan, X.; Zhang, G.; Zhang, F., Multiple roles of graphene in heterogeneous catalysis. *Chemical Society Reviews* **2015,** *44* (10), 3023-3035.

47. Espinosa, J. C.; Navalón, S.; Primo, A.; Moral, M.; Sanz, J. F.; Álvaro, M.; García, H., Graphenes as Efficient Metal-Free Fenton Catalysts. *Chemistry (Weinheim an der Bergstrasse, Germany)* **2015,** *21* (34), 11966-71.

48. Comission, E. Critical raw materials. https://single-market-economy.ec.europa.eu/sectors/raw-materials/areas-specific-interest/critical-raw-materials_en (accessed 24/10/2022).
49. Union, E. European Raw Materials Alliance. https://erma.eu/ (accessed 24/10/2022).
50. Dhakshinamoorthy, A.; Primo, A.; Concepcion, P.; Alvaro, M.; Garcia, H., Doped Graphene as a Metal-Free Carbocatalyst for the Selective Aerobic Oxidation of Benzylic Hydrocarbons, Cyclooctane and Styrene. *Chemistry – A European Journal* **2013,** *19* (23), 7547-7554.
51. Primo, A.; Rendón-Patiño, A.; Bucur, C.; Jurca, A.; Cojocaru, B.; Parvulescu, V. I.; Garcia, H., Doped microporous graphitic carbons as metal-free catalysts for the selective hydrogenation of alkynes to alkenes. *Journal of Catalysis* **2022,** *405*, 355-362.
52. Primo, A.; Neatu, F.; Florea, M.; Parvulescu, V.; Garcia, H., Graphenes in the absence of metals as carbocatalysts for selective acetylene hydrogenation and alkene hydrogenation. *Nature Communications* **2014,** *5* (1), 5291.
53. Navalon, S.; Dhakshinamoorthy, A.; Alvaro, M.; Antonietti, M.; García, H., Active sites on graphene-based materials as metal-free catalysts. *Chemical Society Reviews* **2017,** *46* (15), 4501-4529.
54. Chapter 2 Catalytic processes in industry. In *Studies in Surface Science and Catalysis*, Moulijn, J. A.; van Leeuwen, P. W. N. M.; van Santen, R. A., Eds. Elsevier: 1993; Vol. 79, pp 23-67.
55. Jäger-Waldau, A.; Szabó, M.; Scarlat, N.; Monforti-Ferrario, F., Renewable electricity in Europe. *Renewable and Sustainable Energy Reviews* **2011,** *15* (8), 3703-3716.
56. Stratakes, B. M.; Dempsey, J. L.; Miller, A. J. M., Determining the Overpotential of Electrochemical Fuel Synthesis Mediated by Molecular Catalysts: Recommended Practices, Standard Reduction Potentials, and Challenges. *ChemElectroChem* **2021,** *8* (22), 4161-4180.
57. Nemiwal, M.; Zhang, T. C.; Kumar, D., Graphene-based electrocatalysts: Hydrogen evolution reactions and overall water splitting. *International Journal of Hydrogen Energy* **2021,** *46* (41), 21401-21418.
58. Rendón-Patiño, A.; Domenech-Carbó, A.; Primo, A.; García, H., Superior Electrocatalytic Activity of MoS2-Graphene as Superlattice. *Nanomaterials* **2020,** *10* (5), 839.
59. Chigo Anota, E.; Escobedo-Morales, A.; Salazar Villanueva, M.; Vázquez-Cuchillo, O.; Rubio Rosas, E., On the influence of point defects on the structural and electronic properties of graphene-like sheets: a molecular simulation study. *Journal of Molecular Modeling* **2013,** *19* (2), 839-846.

60. Gosling, J. H.; Makarovsky, O.; Wang, F.; Cottam, N. D.; Greenaway, M. T.; Patanè, A.; Wildman, R. D.; Tuck, C. J.; Turyanska, L.; Fromhold, T. M., Universal mobility characteristics of graphene originating from charge scattering by ionised impurities. *Communications Physics* **2021,** *4* (1), 30.
61. Kato, H.; Kudo, A., Visible-Light-Response and Photocatalytic Activities of TiO2 and SrTiO3 Photocatalysts Codoped with Antimony and Chromium. *The Journal of Physical Chemistry B* **2002,** *106* (19), 5029-5034.
62. Zhang, Z.; Wang, C.-C.; Zakaria, R.; Ying, J. Y., Role of Particle Size in Nanocrystalline TiO2-Based Photocatalysts. *The Journal of Physical Chemistry B* **1998,** *102* (52), 10871-10878.
63. Yu, J.; Xiong, J.; Cheng, B.; Liu, S., Fabrication and characterization of Ag–TiO2 multiphase nanocomposite thin films with enhanced photocatalytic activity. *Applied Catalysis B: Environmental* **2005,** *60* (3), 211-221.
64. Litter, M. I., Heterogeneous photocatalysis: Transition metal ions in photocatalytic systems. *Applied Catalysis B: Environmental* **1999,** *23* (2), 89-114.
65. Yamaguti, K.; Sato, S., Photolysis of water over metallized powdered titanium dioxide. *Journal of the Chemical Society, Faraday Transactions 1: Physical Chemistry in Condensed Phases* **1985,** *81* (5), 1237-1246.
66. Sonawane, R. S.; Dongare, M. K., Sol–gel synthesis of Au/TiO2 thin films for photocatalytic degradation of phenol in sunlight. *Journal of Molecular Catalysis A: Chemical* **2006,** *243* (1), 68-76.
67. Akihide, I.; Hideki, K.; Akihiko, K., A Novel Photodeposition Method in the Presence of Nitrate Ions for Loading of an Iridium Oxide Cocatalyst for Water Splitting. *Chemistry Letters* **2005,** *34* (7), 946-947.
68. Maeda, K.; Saito, N.; Lu, D.; Inoue, Y.; Domen, K., Photocatalytic Properties of RuO2-Loaded β-Ge3N4 for Overall Water Splitting. *The Journal of Physical Chemistry C* **2007,** *111* (12), 4749-4755.
69. Tsukamoto, D.; Shiraishi, Y.; Sugano, Y.; Ichikawa, S.; Tanaka, S.; Hirai, T., Gold Nanoparticles Located at the Interface of Anatase/Rutile TiO2 Particles as Active Plasmonic Photocatalysts for Aerobic Oxidation. *Journal of the American Chemical Society* **2012,** *134* (14), 6309-6315.
70. Nakibli, Y.; Mazal, Y.; Dubi, Y.; Wächtler, M.; Amirav, L., Size Matters: Cocatalyst Size Effect on Charge Transfer and Photocatalytic Activity. *Nano Letters* **2018,** *18* (1), 357-364.
71. Mateo, D.; García-Mulero, A.; Albero, J.; García, H., N-doped defective graphene decorated by strontium titanate as efficient photocatalyst for overall water splitting. *Applied Catalysis B: Environmental* **2019,** *252*, 111-119.

72. Linsebigler, A. L.; Lu, G.; Yates, J. T., Jr., Photocatalysis on TiO2 Surfaces: Principles, Mechanisms, and Selected Results. *Chemical Reviews* **1995,** *95* (3), 735-758.
73. Mercado, C. C.; Knorr, F. J.; McHale, J. L.; Usmani, S. M.; Ichimura, A. S.; Saraf, L. V., Location of Hole and Electron Traps on Nanocrystalline Anatase TiO2. *The Journal of Physical Chemistry C* **2012,** *116* (19), 10796-10804.
74. Mateo, D.; Esteve-Adell, I.; Albero, J.; Primo, A.; García, H., Oriented 2.0.0 Cu2O nanoplatelets supported on few-layers graphene as efficient visible light photocatalyst for overall water splitting. *Applied Catalysis B: Environmental* **2017,** *201*, 582-590.
75. Liu, L.; Lopez-Haro, M.; Perez-Omil, J. A.; Boronat, M.; Calvino, J. J.; Corma, A., Direct assessment of confinement effect in zeolite-encapsulated subnanometric metal species. *Nature Communications* **2022,** *13* (1), 821.
76. Zhu, N.; Liu, C.; Liu, R.; Niu, X.; Xiong, D.; Wang, K.; Yin, D.; Zhang, Z., Biomimic Nanozymes with Tunable Peroxidase-like Activity Based on the Confinement Effect of Metal–Organic Frameworks (MOFs) for Biosensing. *Analytical Chemistry* **2022,** *94* (11), 4821-4830.
77. Gounder, R.; Iglesia, E., The catalytic diversity of zeolites: confinement and solvation effects within voids of molecular dimensions. *Chemical Communications* **2013,** *49* (34), 3491-3509.
78. Rendón-Patiño, A.; Niu, J.; Doménech-Carbó, A.; García, H.; Primo, A., Polystyrene as Graphene Film and 3D Graphene Sponge Precursor. *Nanomaterials* **2019,** *9* (1), 101.
79. Niu, J.; Domenech-Carbó, A.; Primo, A.; Garcia, H., Uniform nanoporous graphene sponge from natural polysaccharides as a metal-free electrocatalyst for hydrogen generation. *RSC Advances* **2019,** *9* (1), 99-106.
80. Valtchev, V.; Tosheva, L., Porous Nanosized Particles: Preparation, Properties, and Applications. *Chemical Reviews* **2013,** *113* (8), 6734-6760.
81. Corma, A.; Corell, C.; Pérez-Pariente, J., Synthesis and characterization of the MCM-22 zeolite. *Zeolites* **1995,** *15* (1), 2-8.
82. Lu, T.; Yan, W.; Xu, R., Chiral zeolite beta: structure, synthesis, and application. *Inorganic Chemistry Frontiers* **2019,** *6* (8), 1938-1951.
83. Primo, A.; Sánchez, E.; Delgado, J. M.; García, H., High-yield production of N-doped graphitic platelets by aqueous exfoliation of pyrolyzed chitosan. *Carbon* **2014,** *68*, 777-783.
84. Szejtli, J., Bender, M. L., and M. Komiyama: Cyclodextrin Chemistry-Reactivity and Structure, Concepts in Organic Chemistry Vol. 6 (Editors: K. Hafner, J.-M. Lehn, C. W. Rees, P. v. R. Schleyer, B. M. Trost and R, Zahradnik) (Cyclodextrin Chemistry. Reaktionsfähigkeit und Struktur, Konzepte der

Organischen Chemie Bd. 6). Springer-Verlag, Berlin - Heidelberg - New York 1978. X, 96 pages, with 14 figs, and 37 tables, cloth DM 44,-; US $ 22.00. *Starch - Stärke* **1979,** *31* (1), 32-33.

85. Szejtli, J., Introduction and General Overview of Cyclodextrin Chemistry. *Chemical Reviews* **1998,** *98* (5), 1743-1754.

86. Connors, K. A., The Stability of Cyclodextrin Complexes in Solution. *Chemical Reviews* **1997,** *97* (5), 1325-1358.

87. Lee, J.-u.; Lee, S.-S.; Lee, S.; Oh, H. B., Noncovalent Complexes of Cyclodextrin with Small Organic Molecules: Applications and Insights into Host–Guest Interactions in the Gas Phase and Condensed Phase. *Molecules* **2020,** *25* (18), 4048.

88. Saenger, W., Cyclodextrin Inclusion Compounds in Research and Industry. *Angewandte Chemie International Edition in English* **1980,** *19* (5), 344-362.

89. Gonzalez Pereira, A.; Carpena, M.; García Oliveira, P.; Mejuto, J. C.; Prieto, M. A.; Simal Gandara, J. Main Applications of Cyclodextrins in the Food Industry as the Compounds of Choice to Form Host–Guest Complexes *International Journal of Molecular Sciences* [Online], 2021.

90. Ryzhakov, A.; Do Thi, T.; Stappaerts, J.; Bertoletti, L.; Kimpe, K.; Sá Couto, A. R.; Saokham, P.; Van den Mooter, G.; Augustijns, P.; Somsen, G. W.; Kurkov, S.; Inghelbrecht, S.; Arien, A.; Jimidar, M. I.; Schrijnemakers, K.; Loftsson, T., Self-Assembly of Cyclodextrins and Their Complexes in Aqueous Solutions. *Journal of Pharmaceutical Sciences* **2016,** *105* (9), 2556-2569.

91. Trotta, F.; Zanetti, M.; Camino, G., Thermal degradation of cyclodextrins. *Polymer Degradation and Stability* **2000,** *69* (3), 373-379.

92. Mettler, M. S.; Mushrif, S. H.; Paulsen, A. D.; Javadekar, A. D.; Vlachos, D. G.; Dauenhauer, P. J., Revealing pyrolysis chemistry for biofuels production: Conversion of cellulose to furans and small oxygenates. *Energy & Environmental Science* **2012,** *5* (1), 5414-5424.

93. Rendón-Patiño, A.; Santiago-Portillo, A.; Vallés-Garcia, C.; Palomino, M.; Navalón, S.; Franconetti, A.; Primo, A.; Garcia, H., Templateless Synthesis of Ultra-Microporous 3D Graphitic Carbon from Cyclodextrins and Their Use as Selective Catalyst for Oxygen Activation. *Small Methods* **2020,** *4* (3), 1900721.

94. Peng, Y.; Rendón-Patiño, A.; Franconetti, A.; Albero, J.; Primo, A.; García, H., Photocatalytic Overall Water Splitting Activity of Templateless Structured Graphitic Nanoparticles Obtained from Cyclodextrins. *ACS Applied Energy Materials* **2020,** *3* (7), 6623-6632.

CHAPTER 2.

OBJECTIVES

As commented in the introduction, the overall objective of the present thesis is to obtain microporous structured graphitic carbons to be applied as carbo- or photocatalysts. Structuration of the graphitic carbons will be achieved in the present thesis following two complementing strategies. In one case, we will use the soft templation method based on self-assembled in an aqueous medium of an amphiphilic organic molecule around which occurs the nucleation of the structured material. In the second approach, organic molecules having a rigid molecular shape as truncated cones that self-assemble by hydrogen bonds will be used as the precursor of these microporous carbons. The relevance of the presence objectives derives from the fact that there are very scarce examples of microporous materials with well-defined and regular porosity in the subnanometric scale. According to the IUPAC classification, the microporosity term applies to those porous materials with pore dimensions below 2 nm. The size of the pores is better relevant in the context of confinement effects, known to activate substrates and make them more reactive.

Two main types of reactions will be tested according to these two methodologies to obtain the microporous graphitic carbons previously mentioned. On the one hand, these materials will be used as aerobic oxidation catalysts using benzylamine oxidative coupling as a benchmark reaction. This constitutes an example of carbocatalysis. The second type to be tested in the present thesis is those in which the energy of the photons is used to activate chemical processes. Specifically, the reactions that will be studied will be photocatalytic H_2 and O_2 evolution, as well as overall water splitting and photocatalytic CO_2 reduction.

Specifically, the objectives of the present thesis are the following:

- Use tetraethylammonium and hexametilenimine as templates to organize the porosity in natural polysaccharides. Study the morphology and properties of graphitic carbons derived from these templated polysaccharides and their use as carbocatalysts to promote the aerobic oxidation of benzylamine, benchmarking other carbocatalysts.
- Doping of microporous graphitic carbons derived from cyclodextrin pyrolysis with phosphorous and evaluating their photocatalytic activity using simulated solar or visible light for H_2 evolution, O_2 evolution, and overall water splitting. The influence of the P doping level on the conduction and valence bands' energy, as well as the cyclodextrin precursor, on the photocatalytic activity, will be evaluated.
- Study of the photocatalytic activity for CO_2 reduction in the presence of sacrificial electron donors of a series of cyclodextrins-derived microporous carbon without doping or containing N or P heteroatoms. The study will determine the nature of the products and should confirm CO_2 as the substrate undergoing reduction.
- Testing the microporous graphitic carbon as an electrocatalyst for the CO_2 reduction according to the previously obtained results in the water splitting and CO_2 photoreduction.

In case the above objectives are achieved, the results obtained will be significant for the progress of carbocatalysis by providing a series of microporous graphitic carbons with uniform porosity and regular structure. These results will show the advantages of porosity and confinement regarding the photocatalytic activity. If these materials' catalytic and photocatalytic activity is high, they will open new avenues in the field for further optimization of their performance. Possible strategies for this purpose will include doping with other elements, generating additional defects, depositing co-catalysts, or forming heterojunctions with other semiconductors and materials.

CHAPTER 3.

MICROPOROUS GRAPHITIC CARBONS PREPARED USING SOFT TEMPLATES EMPLOYED IN ZEOLITE SYNTHESIS AND THEIR CATALYTIC ACTIVITY IN AEROBIC OXIDATION

3.1 Introduction

Previous research of our group has shown the ability of certain natural polysaccharides and derivatives to cote conformably arbitrary surfaces. We coined the term filmogenity to denote this property of forming perfect films of nanometric thickness without cracks, pinholes, or other defects and with subnanometric roughness. [1-5] In comparison, synthetic plastics like for instance polystyrene are also able to form films on different surfaces, but the thickness is typically in the micrometric range, [6-8] while with chitosan, the films that have been achieved in our group can be as thin as 10 nm. [9]

In the present chapter, we went a step forward trying to exploit the filmogenic ability of some polysaccharides to obtain ordered microporous graphitic carbons. The leading idea was that if a nanoobject consisting of a liquid crystal droplet is used instead of a rigid surface, it could also be possible that the polysaccharide tries to reproduce this object. This concept is similar to the accepted mechanism for zeolites and other porous aluminosilicates formation in which amphiphilic organic molecules self-assemble in water, forming micellar-typed suspensions that are subsequently used to drive the crystallization of the aluminosilicate.[10-15] Scheme 3.1 illustrates the concept of soft templation and how this has been used in synthesizing porous aluminosilicates. Scheme 3.1 also shows the idea of the present chapter in which instead of an inorganic precursor that is oligomerizing to form the rigid aluminosilicate framework, a filmogenic organic polymer would undergo templation.

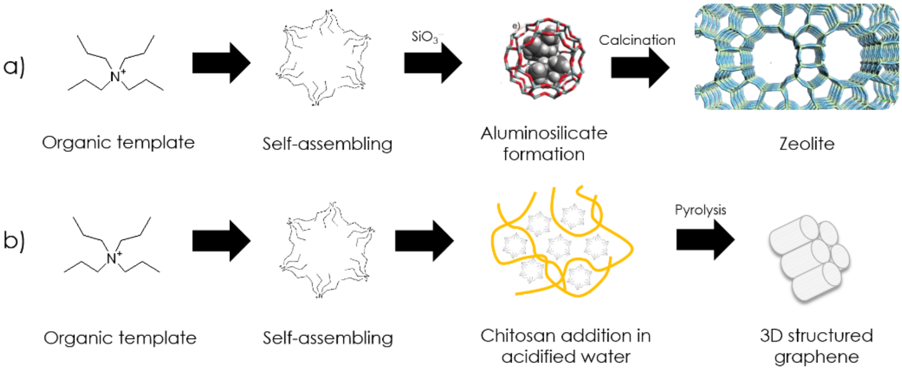

Scheme 3.1. Concept of soft templation a) traditional zeolite synthesis and b) concept followed in the present chapter.

In the present chapter, the biopolymer used to undergo templation will be chitosan, derived from the partial deacetylation of chitin. Chitin is the common exoskeleton of any type of insect and crustaceous. Our group has previously proposed that nature has taken advantage of the filmogenic ability of this material to form thin films with defects and without rugosity. [9] Chitosan is a homo-polymer of glucosamine without ramification. Scheme **3.2** presents the structure of the monomer and chitosan. While chitosan is insoluble in water at neutral or basic pH values due to the strong association of fibrils, it becomes soluble at acidic pH values below 4. Acetic acid is typically used to promote the protonation of the amino groups necessary to dissolve chitosan without promoting hydrolysis of the glucosamine units. This viscose aqueous solution can be used to form thin films on quartz and any other material surfaces.

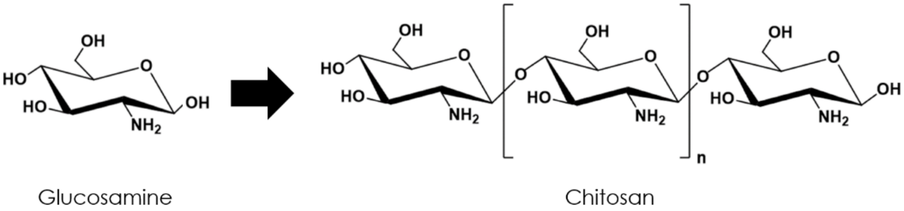

Scheme 3.2. Glucosamine and chitosan structure.

Conventional microscopic techniques can assert the quality of the film. Particularly, AFM provides subnanometric resolution of the thickness of these films, while the frontal view of the surfaces indicates the absence of pinholes, cracks, and peats in the film. [9] Alternatively, water can be removed by freeze drying, providing a chitosan powder, or chitosan can be precipitated by dropping with a syringe the aqueous chitosan solution of sodium hydroxide. In the last case, millimetric spheres with regular diameter can be obtained.[16] Figure 3.1 shows examples of films and microspheres of chitosan obtained from an aqueous solution. Either as film or powder, chitosan undergoes upon pyrolysis at temperatures between 850 to 1300 °C transformation into nitrogen-doped defective graphene. Depending on the thickness of chitosan films, single or few layers of graphene can be obtained by coating the substrate.[9] In the case of the microspheres, the spherical morphology of chitosan is maintained during the pyrolysis to form nitrogen-doped graphitic carbons that can be easily exfoliated with almost quantitative yield into a single-layer or few-layer graphene sheets upon sonication in water or other liquid solvents. [16]

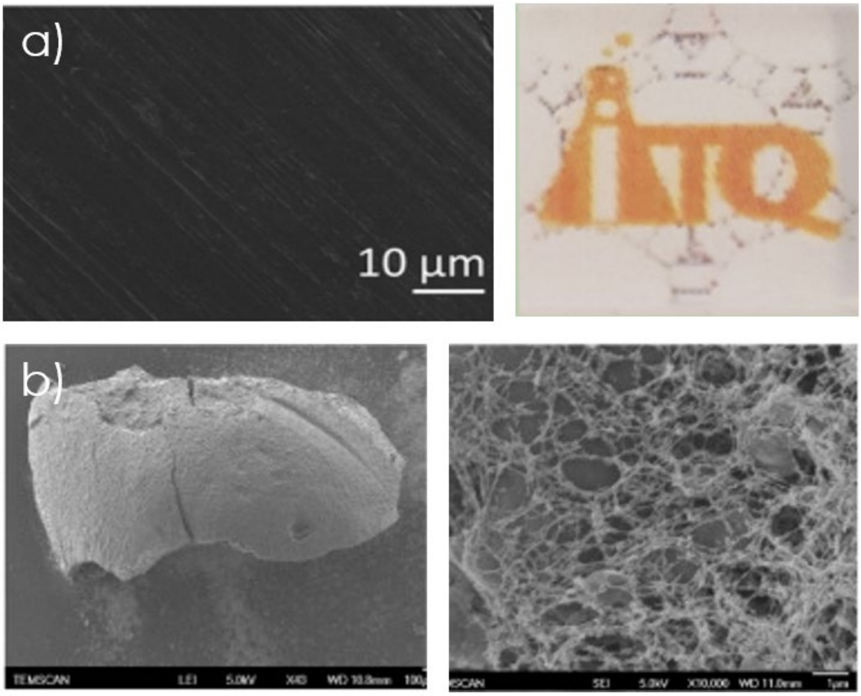

Figure 3.1. Images of film and spheres of chitosan.

Starting from the above knowledge on the filmogenic ability of the chitosan and its conversion into defective and doped graphene, the present chapter aims to use soft templating to explore if the nano-objects generated by the self-assembling of a quaternary ammonium salt can also be used to template the shape of chitosan and, therefore, the resulting N-doped graphene obtained therefrom. Thus, the present chapter reports another procedure inspired by zeolites synthesis of preparation of 3D graphene sponges by hydrothermal synthesis. In particular, we will prepare nitrogen-doped structured graphenes using hexametilenimine (HMI), the templating agent typically used to prepare MCM-22 zeolite.[17] The second structured directing agent used is tetraethyl ammonium (TEA), the template for zeolite β.[18] It will be shown that chitosan undergoes templation by these two structuring directing agents, and after subsequent pyrolysis structures, 3D graphene sponges will be formed. Catalytic tests have demonstrated that the 3D structuration of graphene-defining micropores enhances the catalytic activity of the resulting sponges by the so-called confinement effect [19-20] to promote aerobic oxidations compared to analogous layered 2D materials [9, 21-25].

3.2 Results and discussion

First, sample preparation and characterization will be presented before showing the graphene sponges' catalytic activity for the aerobic oxidation of benzylamine. Comparison with related carbonaceous materials clearly shows the advantages of structuration and microporosity on the catalytic activity.

3.2.1 Samples preparation

Two analogous materials were prepared using chitosan as the precursor and either HMI or TEABr as structuring directing agents. The materials are denoted as 3DNC22 or 3DNCβ depending on the template used in the synthesis, 3D meaning three-dimensional, NC N-doped graphitic carbon, and 22 or β referring to the template in the synthesis.

Material preparation is illustrated in Scheme 3.3. The procedure tries to mimic the hydrothermal synthesis of zeolites with some adaptation to take into account the pure thermal stability and high sensitivity to bases of chitosan. For this reason, the temperature employed in the synthesis was limited to 90 °C, a higher temperature resulting in the formation of the humins as visually observed from the dark color of the suspension. To avoid high based concentration, urea was used as a gradual ammonia precursor under mild conditions. It was anticipated that the generation of NH_3 by the composition of the urea would neutralize the solution's acidity, leading to the precipitation of chitosan due to the high pH values.

On the other hand, the self-assembling of the structural directing agent will form nanoobjects that will be replicated by chitosan due to its filmogenic property. The main difference between the synthesis of 3DNC22 and 3DNCβ is the amount of acetic acid required in the two processes. In the case of 3DNC22, the use of HMI as template with basic character makes it necessary to employ higher amounts of acetic acid to dissolve chitosan than the synthesis of the 3DNCβ. In the last case, the surface template image was neutral TEABr, and the amount of acetic acid was lower since it is needed only to protonate certain glucosamine groups of chitosan.

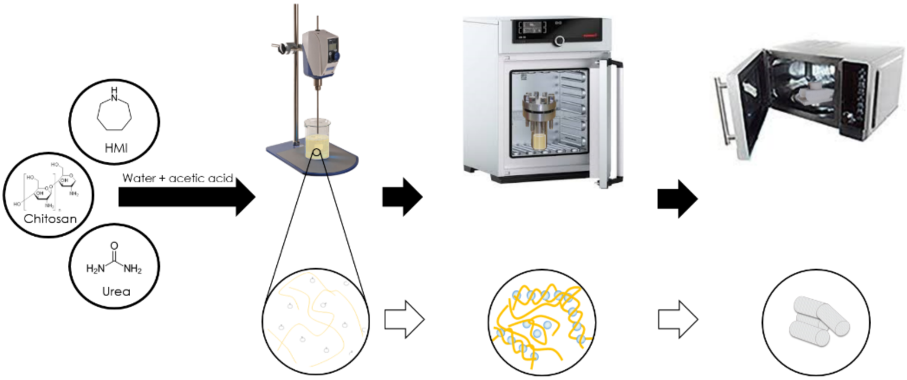

Scheme 3.3 Sample preparation of 3DNC samples, including water dissolution, hydrothermal treatment, and pyrolysis.

After the hydrothermal treatment, the resulting soft sticky material was washed and dried at 60 °C before pyrolysis to transform chitosan into graphene. In the present Chapter, the pyrolysis of chitosan was carried out in a microwave oven at 800 W power using three cycles of power of 1-min heating and 2-min resting time. During the process, the microwave oven was fluxed with an argon flow to decrease oxygen concentration in the chamber. The main advantage of the microwave heating procedure for pyrolysis consists in the short time needed to obtain the structure of the nitrogen-doped graphitic carbons (3 × 3 minutes) compared with conventional electrical furnace pyrolysis, which takes about 24 h.

Nevertheless, samples prepared by conventional pyrolysis were also synthesized to compare with those obtained by microwave.

3.2.2 Characterization

The powders of the materials present a light brown color after the hydrothermal treatment. The XRD patterns exhibit broad peaks coincident in the case of the soft solids prepared using either HMI or TEA as template agents. Comparison with the XRD pattern of chitosan treated with the same hydrothermal process but in the absence of any directing agent shows that these XRD spectra are not affected by the presence or absence of the template agent. At this point, a commercial sample of chitosan powder was also analyzed by XRD diffraction, showing that this sample was amorphous, and lacking any XRD pattern. In addition, the XRD of urea shows an entirely different diffractogram, indicating that this nitrogenated organic compound does not contribute to the diffractogram of the chitosan samples. Figure 3.2 presents selected XRD recorded for the two 3DNC samples and compared with other related precursors.

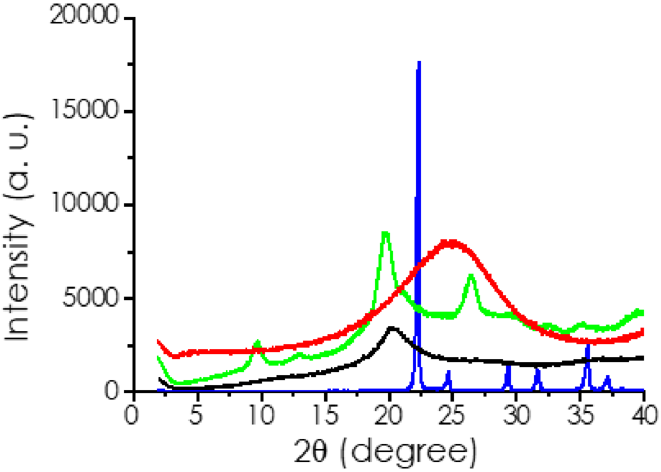

Figure 3.2. XRD patterns of raw chitosan (black), after hydrothermal treatment (green), after pyrolysis (red), and urea (blue).

Given these diffractograms, it is proposed that the diffraction patterns recorded after hydrothermal treatment should correspond more probably to a crystalline chitosan phase appearing in the process. After pyrolysis of the 3DNC samples, the diffraction patterns change significantly, leading to the appearance of a broad band at about 24 ° that has been attributed previously to the imperfect stacking of defective graphene layers in a graphitic carbon residue. The changes observed in the XRD are compatible with the expected transformation of the chitosan into N-doped graphitic carbon.

Thermogravimetric profiles obtained upon gradual heating the samples at a constant heating rate in N_2 or O_2 atmosphere is a helpful technique commonly widely employed in zeolite synthesis to determine the amount of organic template. In the present case, the organic nature of chitosan makes thermogravimetry more complex and challenging to interpret. The comparison between the thermogravimetric plot of pristine chitosan and the samples 3DNC before pyrolysis is presented in Figure 3.3. The differences between the profiles can be taken as an indication of the presence of structure-directing agents, known to desorb and decompose at low temperatures, typically below 300 °C. As can be seen in Figure 3.3, thermogravimetry exhibits some differences between the behavior and that of 3DNC samples before pyrolysis. These differences are particularly notable at temperatures below 300 °C approximately. It is proposed that the initial weight loss of about 4.5 % at temperatures below 200 °C should correspond to the combined desorption of H_2O, as well as the initial stages of template degradation. Subsequently, in the range of temperature between 250 and 350 °C, there is a significant weight loss, of about 48 %, for the 3DNC and the chitosan reference, which should be attributed to the dehydration, decomposition, and the initial stages of restructuring of chitosan. Beyond these temperatures, the minor differences between raw chitosan as reference and the 3DNC samples of about 3 wt % can be attributed to the templating agent in the sample. Finally, at a temperature of about 600 °C, the weight loss is much less important, resulting in a carbon residue of about 35 % for the 3DNC samples.

After pyrolysis, the graphitic 3D sponges were also analyzed by thermogravimetry. The two samples exhibit a weight loss of about 19 % upon heating from room temperature to about 600 °C. This weight loss of 3DNC samples after pyrolysis should correspond to co-adsorbed water (estimated about 3 wt %) and a deeper restructuration and graphitization of the material due to a consecutive thermal treatment.

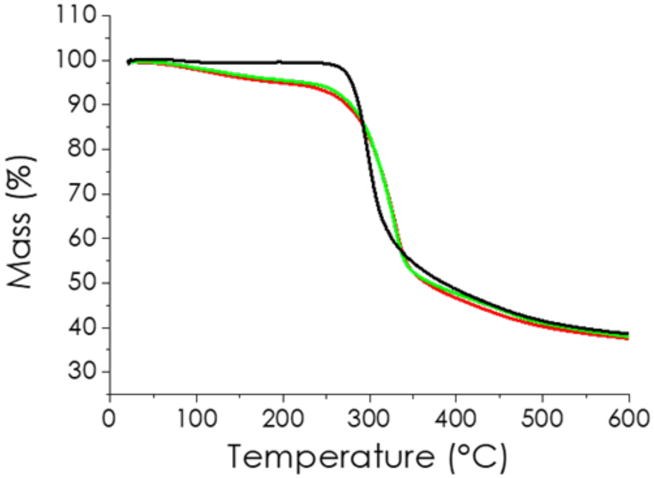

Figure 3.3 Thermogravimetry of raw chitosan (black), 3DNC22 (red) and 3DNCβ (green).

This proposal is in accordance with the elemental analysis of the two 3DNC graphitic sponges that still contain about 16-20 % oxygen and about 14 % nitrogen in their composition after the first pyrolysis process. Table 3.1 summarizes the elemental composition of the 3DNC samples before and after pyrolysis obtained by combustion chemical analysis. This table shows that in the first pyrolysis, the carbon content of the 3DNC sponges is still below 70 %. Consequently, it is still possible that these elements oxygen and nitrogen, as well as some carbon, became gaseous products in the thermal treatment.

Table 3.1. Combustion elemental analysis of the 3DNC sponges.

Material	**% C**	**% H**	**% N**	**% O**
Chitosan	41	6.64	7.61	44.70
3DNC22	39.39	6.02	10.26	44.33
3DNC22 after pyrolysis	64.64	1.10	13.54	20.72
3DNCβ	38.81	6.02	10.72	44.45
3DNCβ after pyrolysis	67.86	1.39	14.18	16.57

XPS is a very important technique for analyzing and obtaining information about the coordination sphere of the different dopant elements in graphitic carbons. [16] Therefore, the transformation of chitosan into 3DNC graphene sponges was further studied by XPS. From the survey XPS spectrum of the 3DNC sponges, quantitative data of the amount of carbon, nitrogen, and oxygen in the material can be obtained. In the present case, the survey XPS spectrum of 3DNC22 shows the presence of carbon, nitrogen, and oxygen in an atomic proportion of 74.6 %, 15.8 %, and 9.5 %, respectively. It should be noted that these atomic percentages referred to the composition of this material's surface rather than the bulk's analysis. This is due to the low energy of soft X-rays that can only screen the external surface. Besides survey XPS, high-resolution XPS carbon and nitrogen peaks were also analyzed for 3DNC22 and 3DNCβ. Figure 3.4 presents high-resolution C1s and N1s peaks for these two 3D materials and the best fitting deconvolution of the experimental peaks to individual components. The proportion of each of these different types of carbon and nitrogen atoms is also indicated in the figures. As can be seen in the figures, the major component of C1s peak has a binding energy of 282.5 eV, corresponding to about 36 % of the total signal attributable to graphitic carbon atoms. This component is accompanied by two others that can be ascribed to carbon atoms bonded to nitrogen or bonded to oxygen with single or a double bond appearing at a binding energy of 286.0 eV. The presence of a minor component at higher binding energies, probably due to carbon atoms bonded to 3 oxygen atoms like in carboxylic groups, accounting for about 6% of the total carbon atoms, was also found in the deconvolution. Both samples, 3DNC22 and 3DNCβ, exhibit similar C1s peaks.

A similar analysis of the XPS N1s peak shows the presence of two main components in similar proportion that can be attributed to pyridinic and graphenic nitrogen atoms appearing at 398.0 eV and 400.0 eV, respectively.

The above analysis of XPS for 3DNC samples agrees with previous reports from our group about the characterization of N-doped defective graphenes derived from chitosan [9]. This coincidence indicates that the hydrothermal treatment to produce the structuration of chitosan and the structure-directing agent’s presence does not significantly influence the distribution of carbon and nitrogen atoms in the material. It should also be noted that O1s peak in XPS is much less informative due to the presence of co-adsorbed water from the ambient that privies in proportion or any other component.

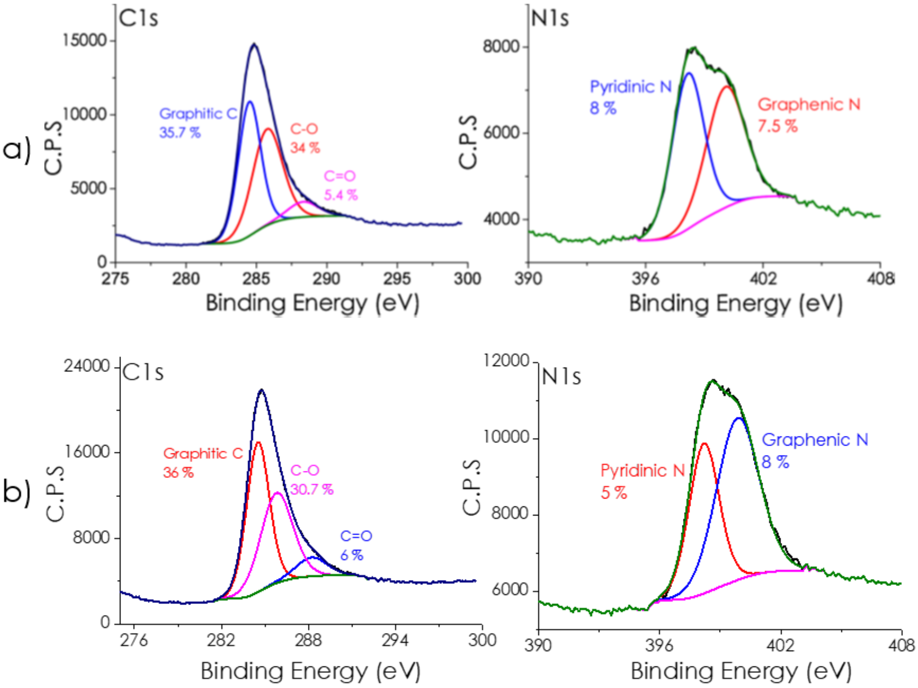

Figure 3.4 High-resolution XPS peaks of C1s and N1s and the best deconvolution to individual components of a) 3DNC22 and b) 3DNCβ.

Vibrational spectroscopy is also a valuable tool for determining the structure of the graphitic carbon and the transformation of the chitosan. Thus, IR spectroscopy shows the disappearance of the characteristic complex IR spectrum of chitosan due to the presence of amino, hydroxyl and glycosidic oxygen that after the pyrolysis is converted into a carbon residue with no much functional groups. To illustrate the transformation, Figure 3.5 shows the IR corresponding to the 3DNC22 sample in which no characteristic vibrations can be reported. The lack of characteristic vibrations bands active in the infrared is consistent with the decreases in polarity of the functional groups upon pyrolysis of chitosan.

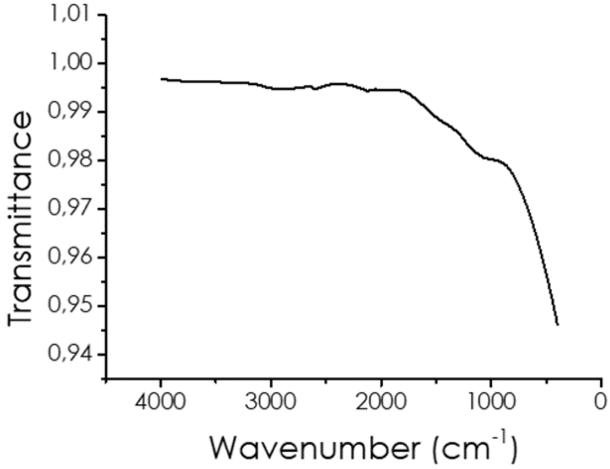

Figure 3.5 Infrared spectrum of the sample 3DNC22.

In comparison, Raman spectroscopy is much more informative. The Raman spectra of the two 3D sponges show the three characteristic peaks at 2900 (very broad), 1950 (sharp) and 1350 (broad) cm^{-1} peaks expected for defective graphitic materials. The 1950 cm^{-1} peak (G band) corresponds to the vibration of the graphitic carbons, while 1350 cm^{-1} (D band) is associated with defects including carbon vacancies and dopant elements. Depending on the number of layers in the structure and the density of defects, an overtone (G+D peak) generally recorded as a very broad vibration band can also be recorded below 3000 cm^{-1}. Figure 3.6 present the Raman spectrum corresponding to the 3DNC22 and 3DNCβ that were almost coincident with those previously reported for the Raman spectra of N-doped defective graphenes derived from chitosan pyrolysis. [3, 26] The intensity of the G over the D band, about 1.15 in the present samples, is taken as a quantitative indicator of the density of defects in the materials. This value is very similar to those commonly reported for reduced graphene oxides in which residual amounts of oxygen are still present in the material. [26-27]

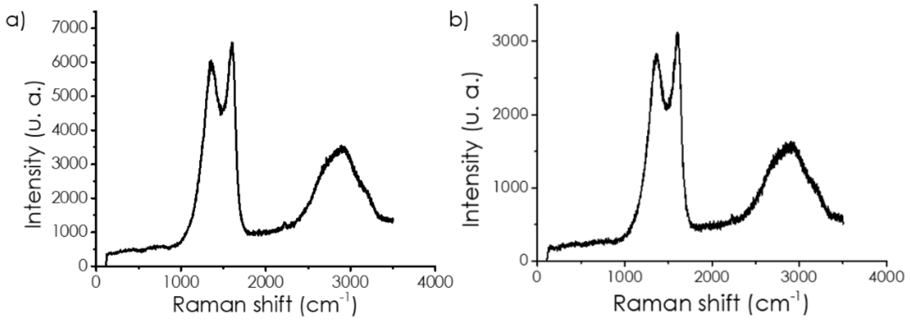

Figure 3.6 Raman spectra of a) 3DNC22 and b) 3DNCβ.

3.2.3 Electron microscopy

The precious characterization data commented on so far mainly indicates the elemental composition, the distribution of the elements into different coordination, and the transformations of the material into defective graphenes. However, this characterization data does not confirm the occurrence of 3D structuring as a consequence of the presence of HMI and TEA as structure-directing agents. Therefore, it is necessary to complement the previous data with isothermal gas adsorption measurements and electron microscopy images of the particles to gain information on the particle morphology and porosity.

Isothermal gas adsorption is a routine technique valid for determine surface area and porosity on porous materials and, particularly, carbon residues. Argon adsorption at 77 K was used to determine the surface area of the two 3DNC sponges. The values are summarized in Table 3.2. As it can be seen in this table the specific surface area of the two 3DNC sponges are about 500 $m^2 \times g^{-1}$ mainly due to the presence of micropores. Considering that the material corresponds to graphene and the theoretical surface area of fully exfoliated graphene is about 2600 $m^2 \times g^{-1}$ [28-30] it can be concluded as average that the 3DNC correspond to the stacking of about 5-6 graphene layers. The micropore size distribution of 3DNC22 and 3DNCβ was determined from the argon desorption branch giving an average value of 2.1 and 4.1 nm respectively. These micropores values are much larger than those typically achieved in zeolite synthesis that are below 1 nm. However, in the present case it could be that the flexibility of the chitosan and the thermal treatment at high temperature of the pyrolysis result in a larger pore dimension compared to zeolite MCM 22 and zeolite beta pores that are about 0.7 nm of pore size. [17]

Table 3.2 Specific surface area of the 3DNC sponges using different adsopted gases.

Gas	**3DNC22 surface area ($m^2 \times g^{-1}$)**	**3DNCβ surface area ($m^2 \times g^{-1}$)**
N_2	536	440
Ar	524	450
CO_2	635	579

Besides Ar and N_2 adoption, the textural and porosity distribution of the two 3DNC materials was completed by CO_2 adsorption measurements. The different adsorption temperature and the kinetic diameter of CO_2 may give different surface area values that N_2 or Ar that have been generally attributed to the presence of ultramicropores in the materials. Ultramicropores are pores of dimensions below 0.6 nm [31] that are generally too narrow to be measured by N_2 or Ar due to their larger kinetic diameter. However, some of these ultramicropores can be accessed by CO_2. Therefore, the difference in surface area based on N_2 or Ar absorption and CO_2 is generally attributed to ultramicropores in a material. [31] As it can be seen in Table 3.2 both 3DNC sponges present higher surface area in the CO_2 measurement compared to N_2 of about 100 $m^2 \times g^{-1}$ in both cases. This discrepancy is proposed to be due to the presence of ultramicroporosity in 3DNC sponges. This ultramicropores could be due to defects in the stacking of the graphene layers defining the walls and channels of the structure and they are so small that cannot be observed by high resolution TEM.

In fact, scanning electron microscopy of the samples reveals that the materials are constituted by particles of hundreds of microns and characterized by large bubbles of several micrometers of dimension. These bubbles are most probably formed by the action of evolving gases during the thermal treatment. The thickness of the particles walls was about 190 nm.

Further additional information about the morphology and structuration of the material at the nanometric length scale was obtained by high-resolution transmission electron microscopy (TEM). TEM images were acquired from samples that were prepared by dispersion of the solid in dichloromethane and submitting the suspension to ultrasound treatment for 30 min to produce the de-aggregation of the solid into primary nanoparticles.

These TEM images reveal a structuring of the material with the presence of uniform channels at the nanometric scale with domains of between 10 and 40 nm. The presence of channels in the structure domains was observed all over the sample. To illustrate the presence of channels in the two 3DNC samples, Figure 3.7 shows selected images taken for 3DNC22 and 3DNCβ. Measurements in these structured regions in which the presence of channels is observed by comparing the contrast images across different lines indicate a constant regular channel size that in the case of 3DNC22 was 1.5 nm while for the sample 3DNCβ the channel diameter was 0.75 nm.

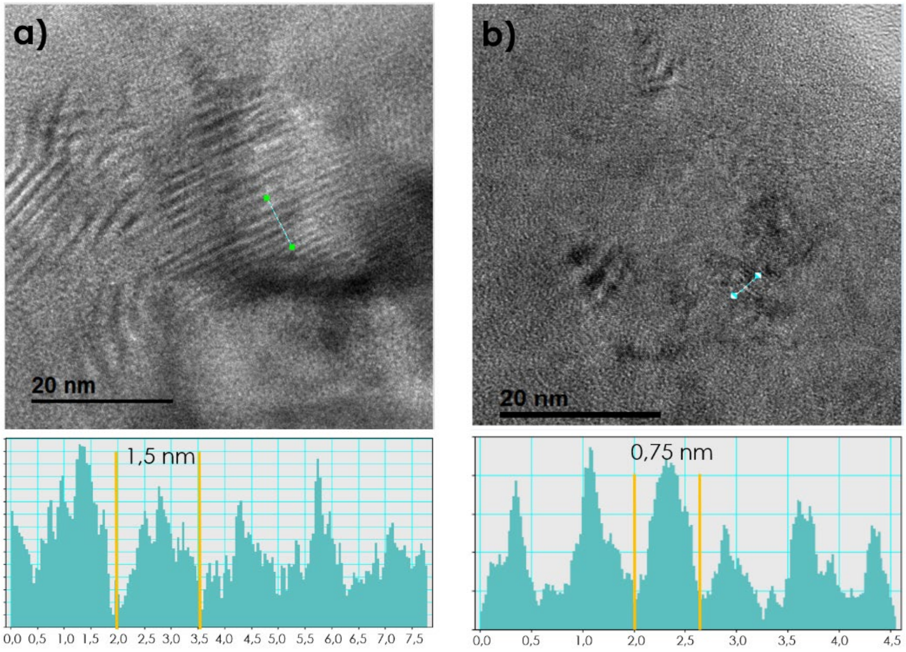

Figure 3.7. High resolution TEM images of a) 3DNC22 and b) 3DNCβ.

TEM images at even higher resolution reveal interlayer distances of 0.34 nm, a value that agrees with the distance between graphene layers in graphitic materials. This would indicate that the walls of the channels would be constituted by defective graphene sheets in good agreement with early reports of the formation of graphenes from chitosan pyrolysis.

To summarize the information obtained by electron microscopy, Scheme 3.4 depicts the structure of the 3DNC materials. It is proposed that this special structuration derives from the use of the HMI or the TEA as template agent of chitosan.

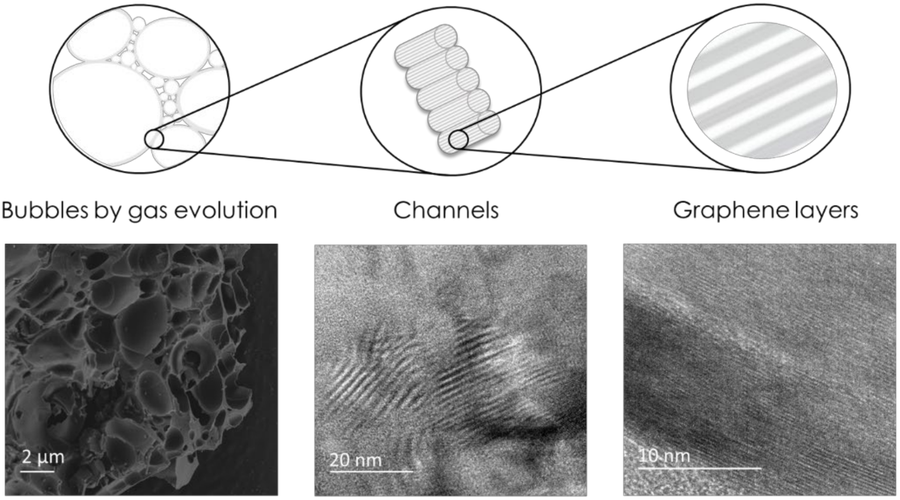

Scheme 3.4. Proposed morphology and structuration of the 3DNC particles.

3.2.4 Catalytic activity

The purpose of the present chapter is to show the possibility of structured chitosan at the nanometric scale by using soft templating and the catalytic consequences of this structuration. Aim at this purpose and considering that one of the most general reaction types that have been widely reported as promoted by carbon-based materials in the absence of any metals is aerobic oxidations, the oxidative coupling of benzylamine was selected as a model reaction. Aerobic oxidations are important industrial processes used on large scale for the oxidation of hydrocarbons and other functional groups. [32] Furthermore, Loh and coworkers proposed aerobic oxidation benzylamine as a benchmark reaction to assess the catalytic activity of metal-free materials and defective graphenes in particular. [33]

For the purpose of the present chapter, it is important to assess whether or not the presence of porosity, even in the range of the ultramicropores as in the 3DNC sponges, enhances the activity of these metal-free catalysts as compared to 2D analogous or even bulk carbons dots. It has been proposed that confinement of oxygen and reaction intermediates can result in an increase in the catalytic activity due to the activation because of these species. This effect of confinement appears an excerpt larger influence when the dimensions of the micropores is similar to the molecular size of the species involved as substrates or intermediates in the reaction mechanism. Most of the presence of the confinement defects refer to inorganic microporous zeolites [19], due to the lack of template carbon materials there is not much information about the operation of about this effect in the case of structured carbons.

In the present chapter and with the objective to compare the catalytic activity of the two 3DNC sponges with respect to related materials, benzylamine aerobic oxidation was performed in the absence of solvents and under a stream of O_2 at atmospheric pressure working at temperatures of 80 °C in the presence or absence of carbon catalyst. Activity data under these conditions are summarized in Table 3.3

Table 3.3. Activity date for the oxidative coupling of benzylamine to N benzylidenebenzylamine catalyzed by different materials.

Entry	Catalyst	Conversion (%)	Selectivity (%)[b]
1	-	4	99
2	G	2	99
3	(N)G	4	99
4	Graphite	8	98
5	GO	11	97
6	rGO	25	98
7	Active carbon Norit	19	99
8	3DNC22	60	99
9	3DNCβ	61	99
10	3DNC22[c]	10	97
11	3DNC22[d]	40	98
12	3DNC22[e]	26	99

[a] Reaction conditions: benzylamine (20 mmol), catalyst (10 mg), oxygen flow at atmospheric pressure, 80 °C, 28 h.

[b] Determined by GC. [c] BHT (50 mg). [d] TEMPO (50 mg). [e] DMSO (250 µL).

As shown in Table 3.3, the main product with essentially complete selectivity of benzylamine oxidation is the N-benzylidenebenzylamine arising from the coupling and de-amination of two benzylamines. In the absence of a catalyst or in the presence of defective graphene from alginate pyrolysis (G) or chitosan pyrolysis ((N)G), benzylamine conversion at 28 h reactions was very low. The use of graphite as catalyst (10 mg) increases somewhat benzylamine conversion that was still below 10 % at 28 h. Higher benzylamine conversion was achieved using graphene oxide (Table 3.3, entry 5) or particularly reduced graphene oxide (Table 3.3, entry 6). Also active carbon, in spite of its large surface area, was unable to increase benzylamine conversion above 20 %.

In contrast, the use as a catalyst of 3DNC sponges results in remarkably high oxidation of benzylamine. Similar results were achieved for 3DNC22 and 3DNCβ (Table 3.3, entries 8 and 9). This high catalytic activity contrast with that of nitrogen-doped graphene also derived from chitosan, therefore indicating the large beneficial influence of (ultra)microporosity to activate molecular oxygen. In the case of 3DNC sponges and due to their high benzylamine conversion, the presence of very small amounts of benzaldehyde was detected in both cases. Figure 3.8 shows the temporal evolution of benzylamine conversion for 3DNC22 and 3DNCB under different conditions. As can be seen in Figure 3.8, hot filtration of 3DNC22 after 1 h reaction when benzylamine conversion was about 10 % shows that the reaction mostly stops in the absence of the catalyst. These results indicate that 3DNC22 is acting as a true catalyst rather than a radical initiator. For chain reaction mechanisms in which the propagation chain is very long, just a few radical species are able to promote the conversion of a large number of substrates. This is not apparently the case with the 3DNC catalyst, since the removal of the solid stop the reaction, meaning that the reaction occurs in the solid. In other words, no radicals in the liquid phase are contributing substantially to benzylamine oxidation.

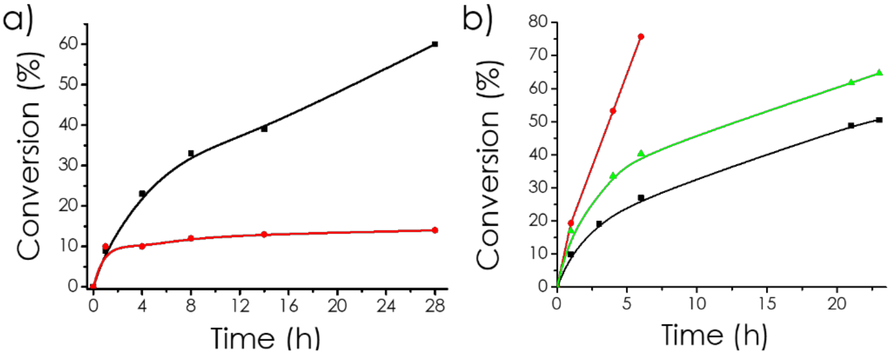

Figure 3.8. a) Time conversion plot for the aerobic oxidation of benzylamine with 3DC22 (black) and filtered after 1 h (red). b) Time conversion plot for the aerobic oxidation of benzylamine with fresh 3CD22 (black), 3D22 with O_2 flux 0.05 L × min^{-1} (green), and 3DCβ (red)

Catalyst stability was confirmed by performing a series of consecutive benzylamine oxidation using the same samples. After each reaction, the 3DNC sponges were recovered from the reaction mixture, washed with chloroform, dried at 60 °C, and used in a consecutive run.

Very similar temporal profiles of benzylamine conversion with almost coincident initial reaction rates and only a minor decrease in final conversion at 24 h (less than 5%) was observed in five consecutive uses, thus confirming catalyst stability. Similar results were obtained for 3DNCβ in 3 consecutive uses as it can be seen in Figure 3.9.

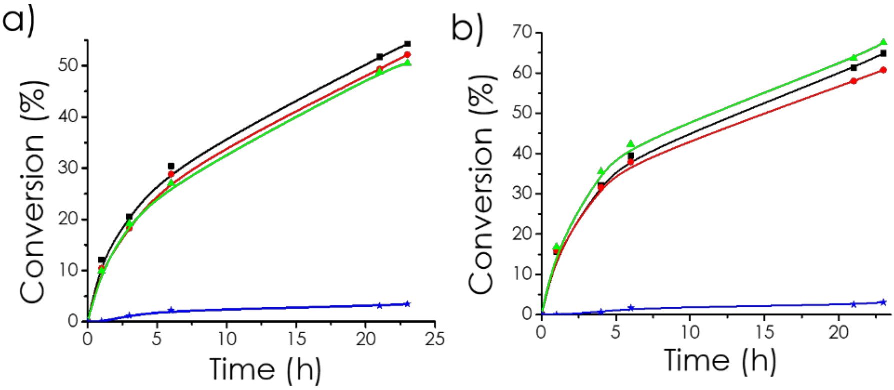

Figure 3.9. Reusability of a) 3DC22 and b) 3DCβ in the aerobic oxidation of benzylamine in successive runs 1st run (black), 2nd run (red), 3rd (green), and no catalyst (blue).

Therefore, it can be concluded that both microporous structures 3DNC sponges are stable under the reaction conditions, the minimal deactivation being attributable to the blocking of channels and active sites by benzylamine or the reaction products that were not removed by the washing of the material.

To understand the reaction mechanism and determine the reactive oxygen species generated in the process, several control reactions were performed. It should be commented that available data in the literature indicate that oxidative benzylamine coupling to N-benzylidenebenzylamine requires some oxygen-centered radicals at the reactive species. A general strategy to address the nature of the major reactive oxygen species participating in a reaction is the use of specific quenchers. In the present case, butylated hydroxytoluene (BHT) was used as a trapping agent of superoxide and hydroperoxy radicals. As can be seen in Table 3.3, the presence of BHT results in a considerable decrease in the benzylamine concentration using 3DC22 as catalyst (Table 3.3, entry 10). These results clearly support superoxide and hydroperoxyl radicals as the main responsible for the generation of benzylamine radicals. Additional quenching experiments were performed using TEMPO as a scavenger. TEMPO is a specific trapping agent of benzyl radicals. The results obtained using 3DNC22 as catalyst and TEMPO as benzyl radical quencher are presented in entry 11 of Table 3.3 It was observed that TEMPO decreases somewhat benzylamine conversion meaning that the agent is able to trap some amino benzyl radicals. It is proposed here that due to the large molecular size of TEMPO and the occurrence of the reaction inside the micropores channels of the 3DNC catalyst, this bulky quencher is unable to stop the reaction completely. In accordance with the previously commented results of the hot filtration test, the oxidative coupling of benzylamine mostly occurs inside the microporous channels of the structured carbons.

The quenching experiment by DMSO was unexpected and provides further information on the nature of the active oxygen species. DMSO is a selective quencher of hydroxyl radicals. Hydroxyl radicals are formed from superoxide by additional proton and electron reduction. Hydroxyl radicals are the most aggressive oxygen species. The results of DMSO quenching are also presented in Table 3.3, entry 12. It was observed that DMSO quenches a significant percentage of the catalytic activity of 3DNC22, although to a lesser extent than BHT. This result indicates that superoxide is transformed into hydroxyl radicals, and both species are able to attack benzylamine. Otherwise, either DMSO would not influence the reaction (no implication of hydroxyl radicals) or the degree of quenching by BHT and TEMPO should not be the same (no activity of superoxide radical). Scheme 3.5 presents the proposed reaction mechanism for the oxidative coupled benzylamine catalyzed by 3DNC sponges.

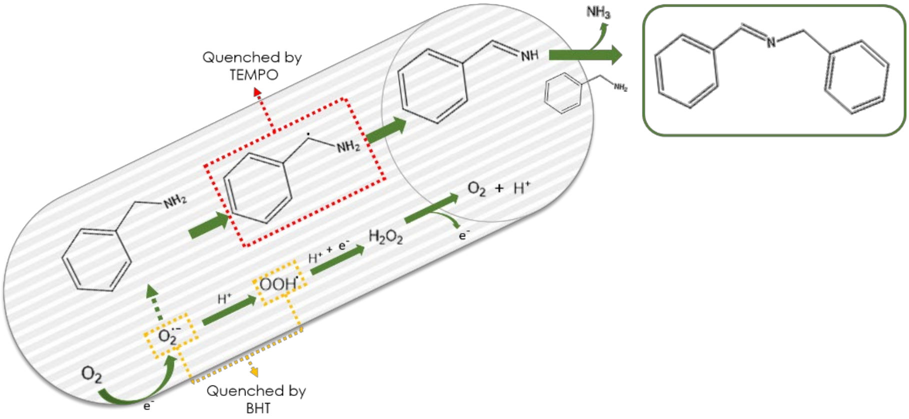

Scheme 3.5. Proposed mechanism for the oxidative coupling of benzylamine that occurs mostly inside the micropores of 3DNC sponges.

Reactive oxygen species will be mainly located inside the micropores with short reaction chain lengths and limited diffusion outside the pores. This would explain why the reaction chain mechanism; the reaction stops upon removal of the solid carbon catalyst. Partial incomplete TEMPO quenching is explained by the steric constraints imposed by the carbon channels of the 3DNC sponges. BHT quenching agrees with superoxide as the primary species.

Type I aerobic oxidations occur thought a chain reaction mechanism in which the initial steps are the generation of oxygen radical species. These reactive oxygen species are typically a cocktail of different oxygen centered radicals, generally formed from molecular triplet oxygen accepting one electron, giving rise to superoxide radical as the primary species. Due to the basicity of superoxide, proton abstraction from water will generate hydroperoxyl radical (HOO·). A subsequent electron-transfer to superoxide, generally coupled with proton transfer, will render hydrogen peroxide (HOOH). Under the reaction conditions, hydrogen peroxide, although more stable than oxygen-centered radicals, undergoes homolytic or heterolytic O-O bonded cleavage giving rise to two hydroxyl radicals (·OH) or one hydroxyl radical and hydroxide. Scheme 3.4 illustrates the series of elementary reactions giving rise to reactive oxygen species that are considered as the initiation steps in the radical chain mechanism in aerobic oxidation. Any of the oxygen centered radical is able to abstract one hydrogen atom from organic substrates due to favorable thermodynamics (OH bonds are stronger than the CH ones) and kinetically uneasy process (no steric hindrance of the process and a single bond to be broken). Subsequently, the generated carbon centered radical will be trapped by molecular oxygen to form a peroxyl radical, able to abstract another hydrogen from the organic substrate. These two steps form the so-called propagation chain since a single carbon-centered radical in the presence of oxygen could be able, in principle, to convert an indefinite number of substrate molecules. The mechanism ends with the ending steps in which two of the radical species coupled into a non-radical product. All these elemental steps are included in the Scheme 3.6.

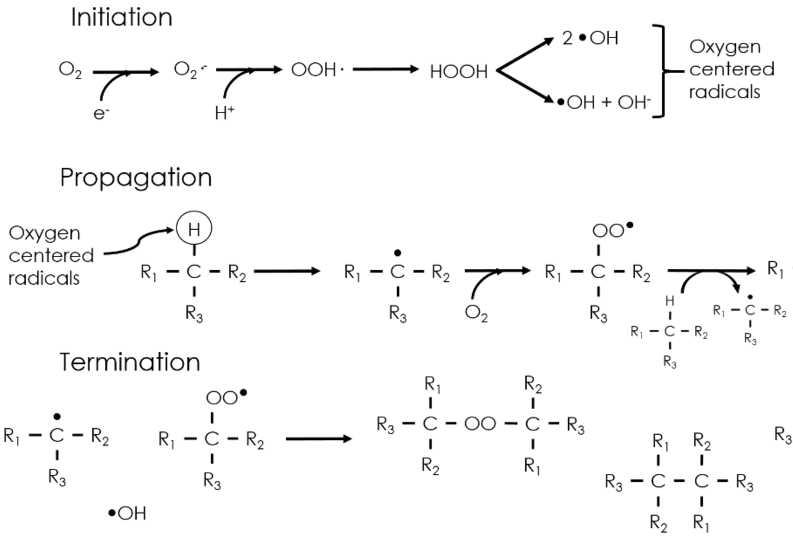

Scheme 3.6. Elementary steps in a reaction chain mechanism illustrating the 3 phases, initiation, propagation and termination, of the type I oxidation.

To make compatible the catalytic results shown in Table 3.3, the quenching experiments with different selective quenchers and the Type I mechanism, it is proposed that the reaction occurs mainly within the micropores of the 3DNC sponges. In this proposal, steric constraints and limited diffusion of the radical to the liquid phase will make the propagation chain very short and limited to only a few cycles. Therefore, no radicals will be almost present in the liquid phase, and under this regime, the 3D sponges will be active as a real catalyst since almost virtually every product molecule requires activation of molecular oxygen by the active site of the catalyst. For this reason, when the catalyst is removed, the reaction stops. This explanation will also be compatible with the partial incomplete quenching by TEMPO of the carbon-centered radicals.

In this mechanistic proposal, the role of the 3D sponges is to activate molecular oxygen by electron transfer from the graphene domains to molecular oxygen affording superoxide initially. The process will generate an electron-hole on the graphenic sites of the catalyst, and these holes would accept one electron from any electron reaching reducing species present in the medium, provided that the redox potential made the process thermodynamically favorable. One well-known reducing species is hydrogen peroxide which is converted into oxygen with a redox potential of 0.695 V.

3.2.5 Conclusions

This chapter has shown that the filmogenic properties of chitosan can also be used to template this material at the nanometric scale using a soft template known in zeolite synthesis. In this way, using HMI, the template of zeolite MCM 22, and TEOABr, the template of zeolite beta, have been used to prepare two similar graphene sponges with 3D structuration as determined by high-resolution transmission electron microscopy and by isothermal gas adsorption. This structuration is noted however reflected in the XRD of the chitosan precursor after the templation. The resulting 3DNC sponges are efficient catalysts to promote the aerobic oxidative coupling of benzylamine to N-benzylidenebenzylamine, a reaction that has been proposed in the state of the art as standard process to evaluate the activity of the different graphene materials. The catalytic results have been explained as the reaction occurring mainly inside the micropores of the material. The operation of confinement effect in which molecules can be activated inside restricted spaces due to the proximity of the walls has been claimed to understand the enhanced catalytic activity of these materials. In this way, the present chapter opens the door for the preparation of other microporous 3D graphenes by soft templation.

3.3 References

1. Mateo, D.; Esteve-Adell, I.; Albero, J.; Primo, A.; García, H., Oriented 2.0.0 Cu2O nanoplatelets supported on few-layers graphene as efficient visible light photocatalyst for overall water splitting. *Applied Catalysis B: Environmental* **2017,** *201*, 582-590.

2. Mateo, D.; Esteve-Adell, I.; Albero, J.; Royo, J. F. S.; Primo, A.; Garcia, H., 111 oriented gold nanoplatelets on multilayer graphene as visible light photocatalyst for overall water splitting. *Nature Communications* **2016,** *7* (1), 11819.

3. Esteve-Adell, I.; He, J.; Ramiro, F.; Atienzar, P.; Primo, A.; García, H., Catalyst-free one step synthesis of large area vertically stacked N-doped graphene-boron nitride heterostructures from biomass source. *Nanoscale* **2018,** *10* (9), 4391-4397.

4. Latorre-Sánchez, M.; Primo, A.; Atienzar, P.; Forneli, A.; García, H., p–n Heterojunction of Doped Graphene Films Obtained by Pyrolysis of Biomass Precursors. *Small* **2015,** *11* (8), 970-975.

5. Primo, A.; Esteve-Adell, I.; Coman, S. N.; Candu, N.; Parvulescu, V. I.; Garcia, H., One-Step Pyrolysis Preparation of 1.1.1 Oriented Gold Nanoplatelets Supported on Graphene and Six Orders of Magnitude Enhancement of the Resulting Catalytic Activity. *Angewandte Chemie International Edition* **2016,** *55* (2), 607-612.

6. Liu, Y.; Goebl, J.; Yin, Y., Templated synthesis of nanostructured materials. *Chemical Society Reviews* **2013,** *42* (7), 2610-2653.

7. Zhang, H.; Cooper, A. I., Synthesis and applications of emulsion-templated porous materials. *Soft Matter* **2005,** *1* (2), 107-113.

8. Malgras, V.; Ji, Q.; Kamachi, Y.; Mori, T.; Shieh, F.-K.; Wu, K. C.-W.; Ariga, K.; Yamauchi, Y., Templated Synthesis for Nanoarchitectured Porous Materials. *Bulletin of the Chemical Society of Japan* **2015,** *88* (9), 1171-1200.

9. Primo, A.; Atienzar, P.; Sanchez, E.; Delgado, J. M.; García, H., From biomass wastes to large-area, high-quality, N-doped graphene: catalyst-free carbonization of chitosan coatings on arbitrary substrates. *Chemical Communications* **2012,** *48* (74), 9254-9256.

10. Cundy, C. S.; Cox, P. A., The hydrothermal synthesis of zeolites: Precursors, intermediates and reaction mechanism. *Microporous and Mesoporous Materials* **2005,** *82* (1), 1-78.

11. Cundy, C. S.; Cox, P. A., The Hydrothermal Synthesis of Zeolites: History and Development from the Earliest Days to the Present Time. *Chemical Reviews* **2003,** *103* (3), 663-702.

12. Wang, Z.; Yu, J.; Xu, R., Needs and trends in rational synthesis of zeolitic materials. *Chemical Society Reviews* **2012,** *41* (5), 1729-1741.

13. Bieseki, L.; Simancas, R.; Jordá, J. L.; Bereciartua, P. J.; Cantín, Á.; Simancas, J.; Pergher, S. B.; Valencia, S.; Rey, F.; Corma, A., Synthesis and structure determination via ultra-fast electron diffraction of the new microporous zeolitic germanosilicate ITQ-62. *Chemical Communications* **2018,** *54* (17), 2122-2125.

14. Simancas, J.; Simancas, R.; Bereciartua, P. J.; Jorda, J. L.; Rey, F.; Corma, A.; Nicolopoulos, S.; Pratim Das, P.; Gemmi, M.; Mugnaioli, E., Ultrafast Electron Diffraction Tomography for Structure Determination of the New Zeolite ITQ-58. *Journal of the American Chemical Society* **2016,** *138* (32), 10116-10119.

15. Bereciartua, P. J.; Cantín, Á.; Corma, A.; Jordá, J. L.; Palomino, M.; Rey, F.; Valencia, S.; Corcoran, E. W.; Kortunov, P.; Ravikovitch, P. I.; Burton, A.; Yoon, C.; Wang, Y.; Paur, C.; Guzman, J.; Bishop, A. R.; Casty, G. L., Control of zeolite framework flexibility and pore topology for separation of ethane and ethylene. *Science* **2017,** *358* (6366), 1068-1071.

16. Primo, A.; Sánchez, E.; Delgado, J. M.; García, H., High-yield production of N-doped graphitic platelets by aqueous exfoliation of pyrolyzed chitosan. *Carbon* **2014,** *68*, 777-783.

17. Corma, A.; Corell, C.; Pérez-Pariente, J., Synthesis and characterization of the MCM-22 zeolite. *Zeolites* **1995,** *15* (1), 2-8.

18. Lu, T.; Yan, W.; Xu, R., Chiral zeolite beta: structure, synthesis, and application. *Inorganic Chemistry Frontiers* **2019,** *6* (8), 1938-1951.

19. Moissette, A.; Hureau, M.; Vezin, H.; Lobo, R. F., Chapter 14 - Electron Transfers Under Confinement in Channel-Type Zeolites. In *Chemistry of Silica and Zeolite-Based Materials*, Douhal, A.; Anpo, M., Eds. Elsevier: 2019; Vol. 2, pp 249-271.

20. Li, Z.; Jeanmairet, G.; Méndez-Morales, T.; Burbano, M.; Haefele, M.; Salanne, M., Confinement Effects on an Electron Transfer Reaction in Nanoporous Carbon Electrodes. *The Journal of Physical Chemistry Letters* **2017,** *8* (9), 1925-1931.

21. Long, J.; Xie, X.; Xu, J.; Gu, Q.; Chen, L.; Wang, X., Nitrogen-Doped Graphene Nanosheets as Metal-Free Catalysts for Aerobic Selective Oxidation of Benzylic Alcohols. *ACS Catalysis* **2012,** *2* (4), 622-631.

22. Dhakshinamoorthy, A.; Latorre-Sanchez, M.; Asiri, A. M.; Primo, A.; Garcia, H., Sulphur-doped graphene as metal-free carbocatalysts for the solventless aerobic oxidation of styrenes. *Catalysis Communications* **2015,** *65*, 10-13.

23. Watanabe, H.; Asano, S.; Fujita, S.-i.; Yoshida, H.; Arai, M., Nitrogen-Doped, Metal-Free Activated Carbon Catalysts for Aerobic Oxidation of Alcohols. *ACS Catalysis* **2015,** *5* (5), 2886-2894.

24. Gu, Q.; Wen, G.; Ding, Y.; Wu, K.-H.; Chen, C.; Su, D., Reduced graphene oxide: a metal-free catalyst for aerobic oxidative desulfurization. *Green Chemistry* **2017,** *19* (4), 1175-1181.

25. Dreyer, D. R.; Jia, H.-P.; Bielawski, C. W., Graphene Oxide: A Convenient Carbocatalyst for Facilitating Oxidation and Hydration Reactions. *Angewandte Chemie International Edition* **2010,** *49* (38), 6813-6816.

26. Baldovi, H. G.; Krüger, M.; Reinsch, H.; Alvaro, M.; Stock, N.; Garcia, H., Transient absorption spectroscopy and photochemical reactivity of CAU-8. *Journal of Materials Chemistry C* **2015,** *3* (15), 3607-3613.

27. Seehra, M. S.; Narang, V.; Geddam, U. K.; Stefaniak, A. B., Correlation between X-ray diffraction and Raman spectra of 16 commercial graphene–based materials and their resulting classification. *Carbon* **2017,** *111*, 380-385.

28. Baburin, I. A.; Klechikov, A.; Mercier, G.; Talyzin, A.; Seifert, G., Hydrogen adsorption by perforated graphene. *International Journal of Hydrogen Energy* **2015,** *40* (20), 6594-6599.

29. Pumera, M., Graphene-based nanomaterials for energy storage. *Energy & Environmental Science* **2011,** *4* (3), 668-674.

30. Tai, Z.; Yan, X.; Lang, J.; Xue, Q., *Lancet* **2011,** *199*, 373-378.

31. Peng, L.; Doménech-Carbó, A.; Primo, A.; García, H., 3D defective graphenes with subnanometric porosity obtained by soft-templating following zeolite procedures. *Nanoscale Advances* **2019,** *1* (12), 4827-4833.

32. Navalon, S.; Dhakshinamoorthy, A.; Alvaro, M.; Garcia, H., Carbocatalysis by Graphene-Based Materials. *Chemical Reviews* **2014,** *114* (12), 6179-6212.

33. Su, C.; Acik, M.; Takai, K.; Lu, J.; Hao, S. J.; Zheng, Y.; Wu, P.; Bao, Q.; Enoki, T.; Chabal, Y. J.; Loh, K. P., Probing the catalytic activity of porous graphene oxide and the origin of this behaviour. *Nat Commun* **2012,** *3*, 1298.

CHAPTER 4.

CYCLODEXTRINS AS PRECURSORS OF MICROPOROUS GRAPHITIC CARBONS. BAND ENGINEERING BY PHOSPHOROUS DOPING

4.1 Introduction

As commented earlier in the introduction chapter, there is much current interest in developing new processes for the production of green hydrogen from water. [1] Hydrogen has been considered a possible alternative to the use of fossil fuels in transportation. Also, it can be a chemical to store massive amounts of energy from renewable electricity when there is a peak in production compared to the demand. Among the various possible alternatives, the direct conversion of sunlight into hydrogen is appealing since it would require only a single material, the photocatalyst, in contact with water for hydrogen generation. [2] This would considerably minimize the cost of installing wind turbines and electrolyzers.

Back in mead 70s, Fujishima and Honda already reported that UV irradiation of a titanium dioxide photoelectrode was able to generate hydrogen.[3] Since then, many studies have reported the photocatalytic activity of TiO_2, mainly containing noble metals for hydrogen generation. [4] In this research, the target is to increase the efficiency under solar light irradiation and avoid using noble and critical transition metals, which are limited compared to their demand. [5]

Although the initial development in photocatalysis was based on inorganic semiconductors and mainly motivated by avoiding transition metals, [4] there has been a recent interest in developing metal-free photocatalysts. Among them, the best-studied case is graphitic carbon nitride which is obtained, among other procedures, by thermal condensation of amino-substituted triazines. [6] For carbon nitride, it has been found that the photocatalytic activity depends considerably on the precursors and synthesis procedure because they determine the structural integrity and the presence of defects. [7-8] The presence of co-catalysts on carbon nitride has also been studied as a method to increase their photocatalytic activity. [9] Although considerably less studied than graphitic carbon nitrides, defective graphenes have also received some attention as metal-free photocatalysts. [10] In particular, our group has shown that nitrogen and phosphorous doping of defective graphene introduces visible light photoresponse on these types of graphenes. [11-12] Also, the presence of metal nanoparticles such as gold or copper acting either as co-catalyst or heterojunctions significantly enhances the photocatalytic activity of graphenes. [13-14] Therefore, continuing with this line of research, it is crucial to determine the influence of the structuration of the graphene sheets on the photocatalytic activity of carbonaceous materials.

Upon structuration, the presence of micropores and ultramicropores can add an extra factor in the material influencing the photocatalytic activity by introducing confinement effects. These confinement effects derive from the electrostatic interaction between the walls of the porous materials and the occluded molecules that are particularly important when there is a tight fit of the substrate inside the micropores. [15-16]

As commented in the introductory chapter, our group has developed novel methods for preparing 2D graphenes by pyrolysis at 900 °C of polysaccharides such as chitosan and alginate. With these linear and branch polysaccharides, the formation of graphenes as a single layer or a few layers' stacks can be obtained upon sonication of the graphitic carbon residue after the pyrolysis. [17]

Similar to the behavior of linear polysaccharides, the group also reported that the pyrolysis of cyclodextrins forms structured microporous graphitic residues in which the walls have the characteristic hexagonal structure of graphene. [18] It appears that the conical shape of the cyclodextrin favors the arrangement of these cyclic molecules into tubes, as it is observed upon melting cyclodextrin at about 300 °C. Further heating at pyrolytic temperatures of 900 °C transforms cyclodextrins into microporous graphitic carbon nanoparticles of about 20-30 nm. The channels of these microporous particles are related to the dimensions of the cyclodextrin precursor. [19] Chemical analysis shows that these microporous graphitic carbons are constituted by carbon over 90 % with minimal residual oxygen content.

An essential property of these structured microporous carbons was their semiconducting nature, as revealed by their photocatalytic activity. However, the photocatalytic activity was low, and it is necessary to increase this activity further. One general way to increase photocatalytic activity is by introducing dopant elements in the optimal amount. [20] Theoretical studies have shown that the presence of dopant elements can create intra-band gap stages that resolve in a new band alignment that could render the material more efficient from the photocatalytic point of view. As commented, this methodology has also worked for graphenes and carbon nitrides. [6, 21-22]

Following the lead of P-doping of graphene, which has been shown to increase the photocatalytic activity of defective graphenes, the present chapter describes the remarkable influence of P-doping on the photocatalytic activity of microporous graphitic carbons derived from cyclodextrins. [23] This influence derives from the appropriate band alignment due to the presence of P atoms. In addition, it has also been observed the effect of the pore size on the photocatalytic activity for hydrogen generation by overall water splitting.

4.2 Results and discussion

4.2.1 Material preparation and characterization

Based on the prior studies on cyclodextrins pyrolysis, [18-19] the preparation procedure of the present materials consists of heating cyclodextrins up to 900 °C with an intermediate step of about 300 °C. Although the melting point of cyclodextrins depends on the number of glucose units, all of them are close to 300 °C. By introducing in the temperature program an annealing step at 300 °C for 2 hours, it is expected that cyclodextrins will become melted at this temperature, making easier the aggregation of their units into tubular structures. It has been proposed that due to the conical shape, the narrower opening of one cyclodextrin is inserted into the larger entrance of a neighbor cyclodextrin.[14] This aggregation is illustrated in Scheme 4.1 and will take place before the chemical transformation of the glucoses into graphitic carbon that requires much higher temperatures. Graphitization and material synthesis is completed after the annealing step by heating at 900 °C. P-doping is achieved by introducing in the oven mixed with cyclodextrins, a non-volatile precursor of phosphorous.

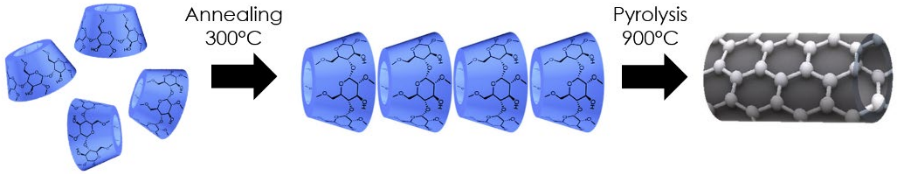

Scheme 4.1. Formation of the microporous graphitic carbon.

In the present chapter, two different P-containing precursors, phosphoric acid and phytic acid, were used. [23] At the typical temperatures and reductive conditions of the pyrolysis, [24-25] phosphorous undergoes reduction to elemental phosphorous or phosphorous species with lower oxidation states that can become incorporated into the graphene by forming carbon-phosphorous bonds. [23] The proposed simplified doping process is illustrated in Scheme 4.2.

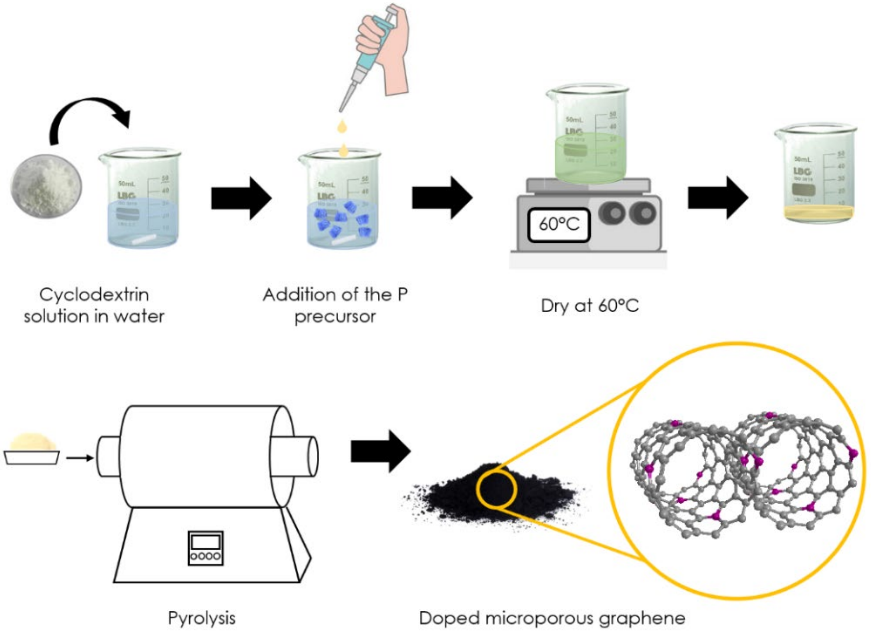

Scheme 4.2. Process of doping of the cyclodextrins.

The presence of phosphorous in the resulting graphitic carbon residue was determined by elemental chemical analysis and resulted in much lower percentages than expected according to the proportion of the phosphorous precursor. The amount of phosphorous incorporated into the microporous graphitic carbon could not be predicted. However, a trend relating high percentages of P precursor with higher rates of P in the resulting graphitic carbon residue was observed. Table 4.1 indicates the samples prepared in the present chapter, as well as their primary analytical data and specific surface area values determined by CO_2 adsorption isotherms.

Table 4.1. List of carbon materials prepared by pyrolysis of alpha, beta, and gamma cyclodextrins at 900 °C in the presence of a phosphorous-containing precursor.

Sample	% C[a]	% P[a]	Surface area[c] ($m^2 \times g^{-1}$)	Band gap (eV)
C_α	95.44	0	728	3.30
$(P)C_\alpha$-1	79.85	0.14	923	4.50
$(P)C_\alpha$-2	71.77	2.40	1928	3.16
$(P)C_\alpha$-3	55.17	2.40	-	3.07
$(P)C_\alpha$-4[b]	75.05	1.56	1573	3.24
$(P)C_\beta$-2	73.95	1.37	1150	3.28
$(P)C_\gamma$-2	77.38	3.25	1619	3.01

[a] The amount of C was obtained by combustion elemental analysis, while the %P by XPS and ICP-OES. [b] The P precursor is phytic acid, and phosphoric acid was the P precursor in the rest of the samples. [c] N_2 adsorption was negligible; therefore, these results were obtained by CO_2 adsorption.

The table also indicates the carbon and phosphorous content and specific surface area. The band gap of each material determined from the Tauc plot of the diffuse reflectance optical adsorption spectroscopy has also been included.

As can be seen in Table 4.1, pyrolysis of cyclodextrins with phosphorous precursors increases considerably by almost a factor of 2 in the specific surface area of the material. Figure 4.1 shows a representative CO_2 adsorption isotherm with the corresponding surface value. This fact has already been reported in the literature for the pyrolysis of other biomass materials. [17] We propose that the strong acidity of the precursors under phosphoric acid or phytic acid under high temperatures favors the corrosion of the carbon residue with the removal of oxygenated groups by the evolution of water, CO_2, and other gases. This corrosion will generate ultramicroporosity on the graphene walls as a consequence of the atom vacancies caused by the acid attack. In any case, the large surface area suggests and considering the graphitic nature of the material would indicate that single or few layers of graphene should constitute the walls of these materials because the specific area values are close to the maximum theoretical surface area of ideal graphene that is about 2650 $m^2 \times g^{-1}$.

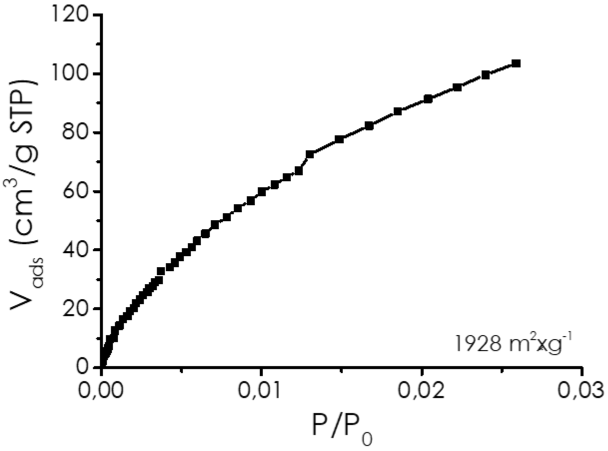

Figure 4.1. Isotherm CO_2 absorption of (P)C_α-2.

Figure 4.2 to Figure 4.5 show the thermogravimetric profile of P-doped graphitic carbons (P)C upon heating the sample at 900 °C under air. These profiles show a weight increase in the temperature range from 200 °C to 600 °C. It is proposed that this temperature increase reflects the oxidation of partially reduced P atoms to different types of phosphorous oxides. Beyond 600 °C and up to about 700 °C, the weight decrease corresponds to the combustion of most of the carbon component of the material, which is about 80 %, and in the case of the (P)C_β, over 90%. The residual weight should correspond to some phosphorous oxide species.

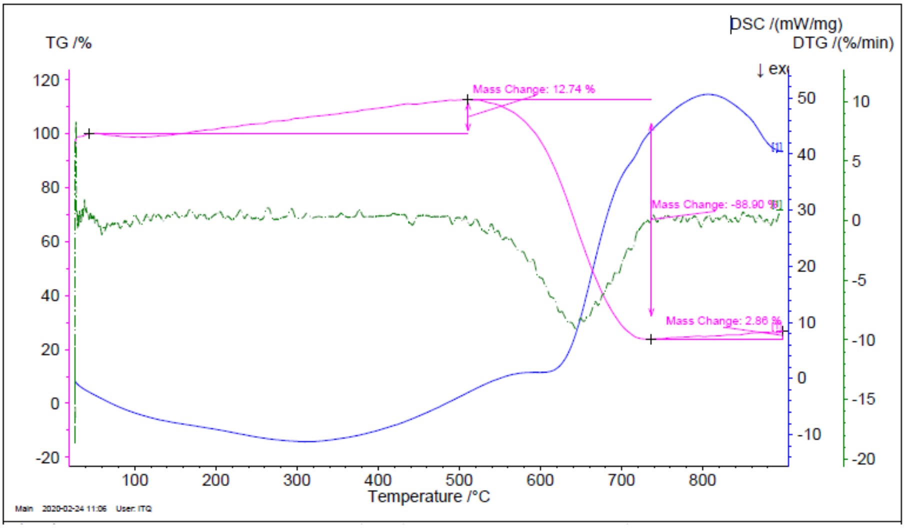

Figure 4.2. Thermogravimetric analysis in air (TGA) of the sample (P)C$_{\alpha}$-2.

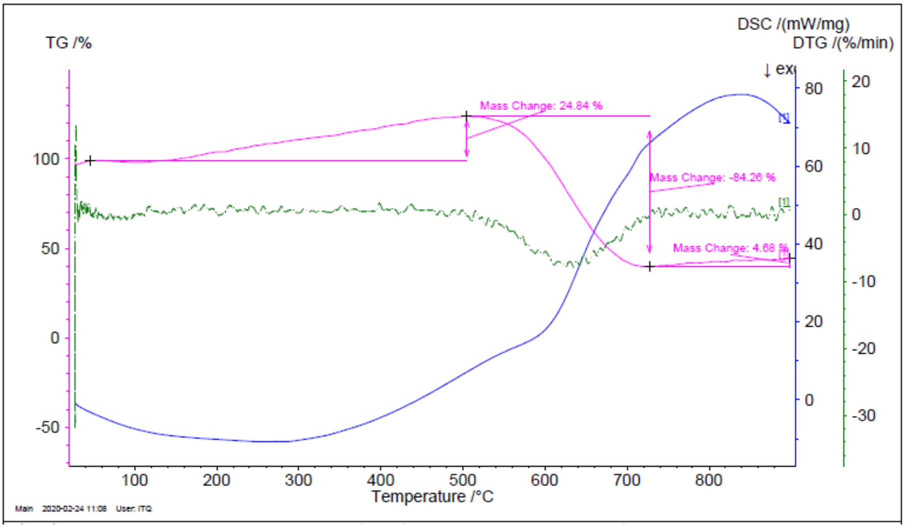

Figure 4.3. Thermogravimetric analysis in air (TGA) of the sample (P)C$_{\alpha}$-4.

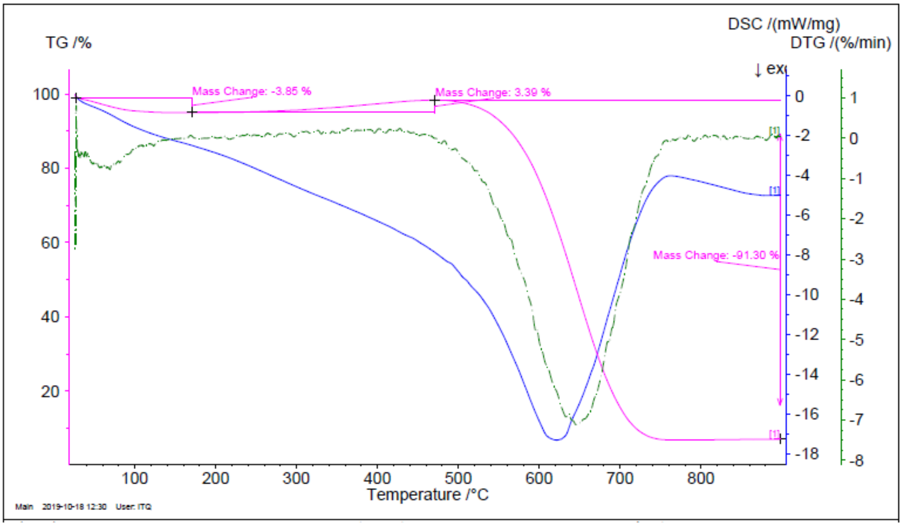

Figure 4.4. Thermogravimetric analysis in air (TGA) of the sample (P)C_β-2.

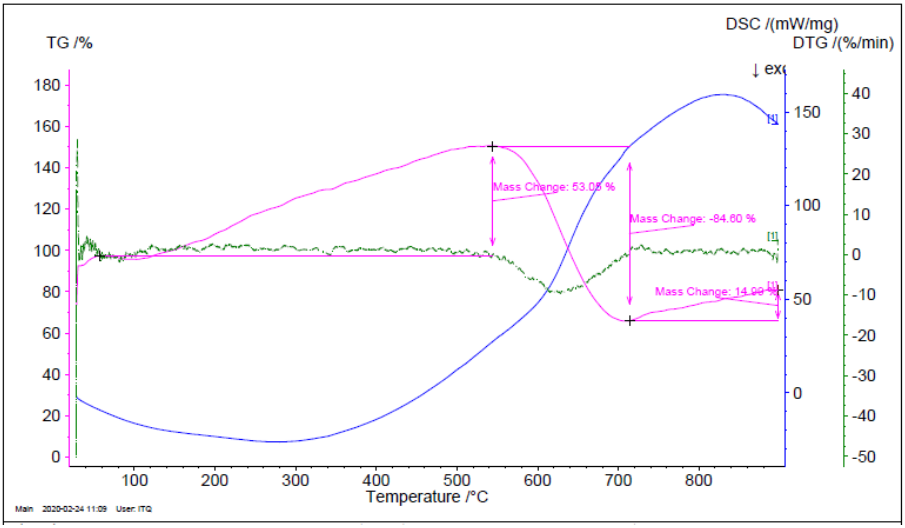

Figure 4.5. Thermogravimetric analysis in air (TGA) of the sample (P)C_γ-2.

The nature of the carbon residue after pyrolysis and, particularly, the graphene layer as a constituent of the material was as confirmed by Raman spectroscopy. Raman spectra were acquired upon excitation with a visible laser at 514 nm, recording a series of Raman spectra at different parts of the sample using an optical microscope coupled to the Raman spectrophotometer. The Raman spectra of all the series of carbon materials derived from cyclodextrins with or without doping agents were very similar as can be seen in Figure 4.6.

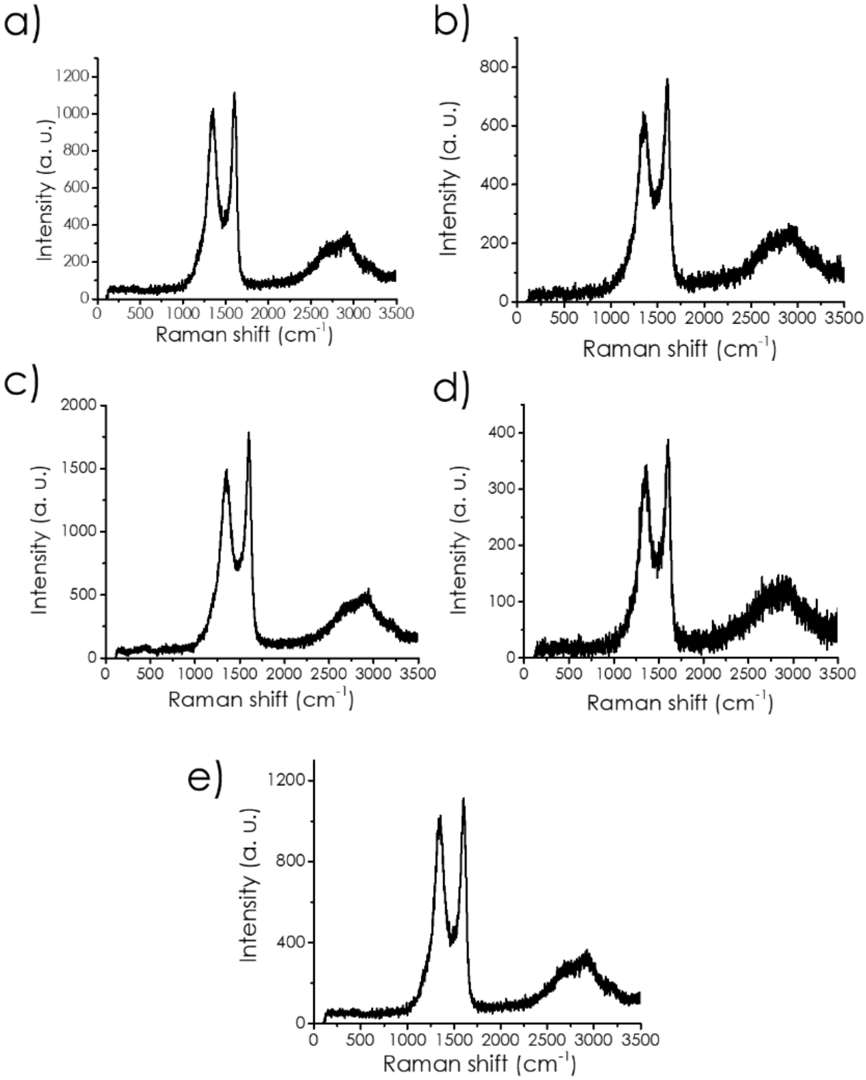

Figure 4.6. Raman spectra of the samples a) (P)C$_\alpha$-2, b) (P)C$_\alpha$-3, c) (P)C$_\alpha$-4, d) (P)C$_\beta$-2 and e) (P)C$_\gamma$-2.

The expected G and D bands were recorded at 1950 and 1350 cm^{-1}, respectively. Remarkably the G band was particularly narrow, and the G and

D bands were well resolved. They were accompanied by a less intense and broader overtone in the region from 3250 to 2500 cm^{-1} that corresponds to the G+D and 2D overtones.[26] In some of the samples, as in the case of (P)C$_\alpha$-2, these overtones were particularly well resolved, this being characteristic of few layers graphenes. The relative intensity of the G versus D band (I_G/I_D) is generally taken as a quantitative indicator of the density of defects of the material. Typical values in the literature for many reduced graphene oxide materials have I_G/I_D ratios of 0.9. In the present case, the relative intensity of the G and D bands was between 1.15 and 1.25, which is in the range previously reported by our group for defective graphenes derived from polysaccharides pyrolysis as in the present case.[27]

The morphology of the mp-(P)C samples and the microporous structure of the nanoparticles was determined by electron microscopy. In Figure 4.7 it can be seen selected FESEM images of the most active sample of the series. EDS analysis of these images shows a coincidence in the distribution of carbon and phosphorous elements, indicating that both elements form a part of the material without observing the presence of segregated phosphorous oxide. At higher resolution, particles of about 20-30 nm were observed. Figure 4.8 shows some images of two different particles. The presence of these particles in the pyrolysis of cyclodextrins was already reported, and it appears that the presence of phosphorous does not influence the morphology of the graphitic carbon residue. These images show the presence of channels in these nanoparticles. From the periodic contrast between the channels and the walls, the dimension of these channels could be obtained. In the case of the material (P)C$_\alpha$-2 derived from α-cyclodextrin, the pore dimension was 0.66 nm, while the size of these channels increases for samples derived from β- and γ-cyclodextrin, which was estimated to be 0.97 and 1.32 nm respectively. Therefore, according to previous reports studying the microporous graphitic carbons derived from cyclodextrins, it appears that the dimension of the channels is related to the diameter of the corresponding cyclodextrin precursor and the number of glucose units that conforms to them. Specifically, the internal diameter of α-, β-, and γ-cyclodextrin have been reported to be 5.7, 7.8, and 9.5 Å,[19] respectively.

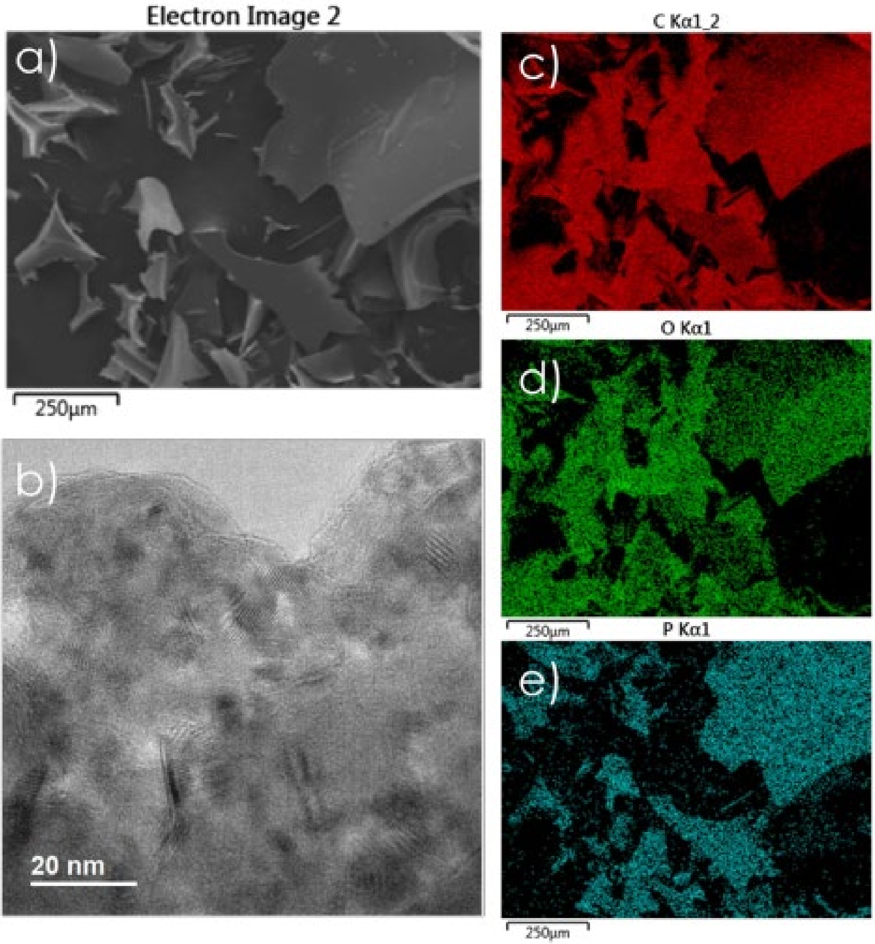

Figure 4.7. a) FESEM image and b) low resolution TEM image of (P)C_α-2. Frames c, d and e correspond to the EDS elemental mapping of image a.

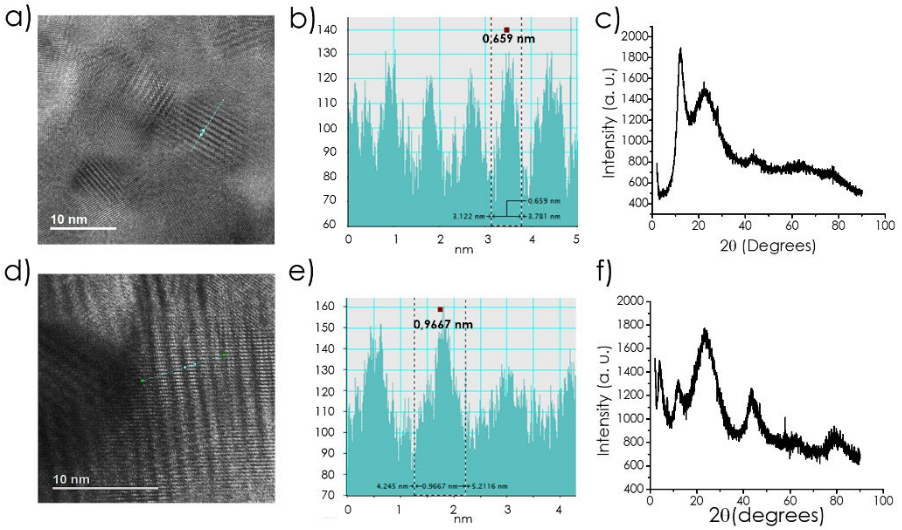

Figure 4.8. HRTEM images of (P)C$_\alpha$-2 a) and (P)C$_\beta$-2 d). b) and e) show the periodic contrast across the line in TEM images to estimate the pore dimension. c) and f) show the XRD patterns of (P)C$_\alpha$-2 and (P)C$_\beta$-2, respectively.

Regarding the channel dimension, it is worth remarking that while nitrogen adoption gives some surface area and porosity for β- and γ- cyclodextrin, this technique fails in the case of α-cyclodextrin due to the lack of nitrogen adsorption. For this reason, surface area measurements presented in Table 4.1 were performed by CO_2 adsorption at 273 K. Under these conditions and due to the smaller kinetic diameter compared to the nitrogen, remarkable values of surface area were measured for (P)C$_\alpha$, close to 2000 $m^2 \times g^{-1}$, corresponding to a complete exfoliated single layer of graphene.

Also, the absence of specific particles due to phosphorous oxide is significant in the electron microscopy images' inspection and elemental analysis. As it would be commented on later, when describing the characterization of the samples by XPS, it seems that mp-(P)C samples contain phosphorous as a dopant element of the carbon and not as independent material.

The analysis by HRTEM agrees well with measurements by dynamic laser scattering of the samples after dispersing the powder in the aqueous phase by extended ultrasound treatment. Scattering of the laser shows the presence of monomodal particles of about 110 nm kinetic diameter. Figure 4.9shows one of these measurements by DLS for the sample (P)C$_\alpha$-2 at neutral pH. Importantly, at neutral pH values, electrochemical Z-potential measurement indicates that the nanoparticles have a negative charge with a potential of -45.2 mV (See Figure 4.9). This considerable potential corresponds to stable and persistent colloids that would not agglomerate upon standing. The negative value also agrees with carboxylates and/or phosphate groups as responsible for surface charges.

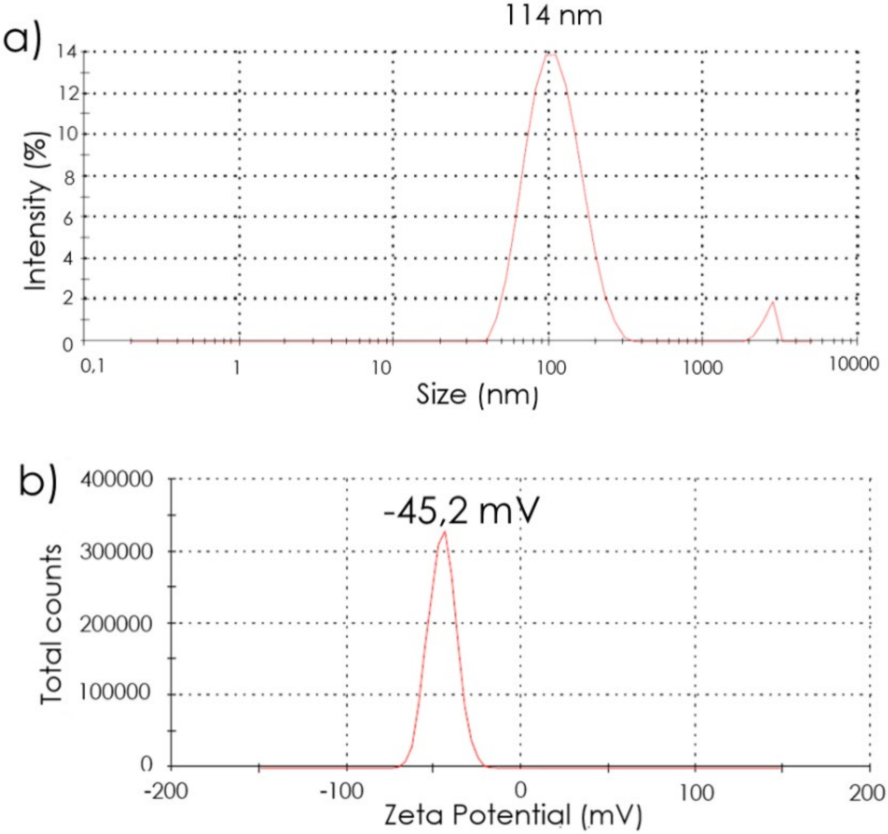

Figure 4.9. a) Particle size distribution and b) Zeta potential of the aqueous suspension of (P)C_α-2 at neutral pH.

Most of the graphitic carbons reported in the literature exhibit two broad bands at about 24 and 42 °, corresponding to the stacking of the 002 planes and 101 diffractions [28-30], respectively. These two peaks are also present in high crystalline pyrolytic graphene as very narrow peaks that are usually taken as a reference for instrument calibration. In the presence of mp-C materials, the XRD spectra were significantly better resolved than is typical for analogous carbon derived from pyrolysis of polysaccharides, probably indicating a better crystallinity. Importantly, besides these two expected bands, mp-(P)C materials also exhibit an additional sharp peak at angles smaller than 15 ° that would propose the alignment of the channels in the particles. Figure 4.8 presents two representatives XRD of the samples. It should be noted that the sharp low angle peak also confirms the remarkable uniformity and regularity of the channels in the mp-(P)C materials. We propose that this regularity is inherited from the shape of the cyclodextrin precursor.

Phosphorous is one element suitable for NMR spectroscopy due to the nuclear spin (S1/2). mp-(P)C samples exhibit similar ^{31}P spectra. These samples show in ^{31}P NMR spectroscopy two peaks, one sharp at about 0 ppm and the other much broader and less intense, centered at about 35 ppm. According to the literature, we assigned these two peaks to graphitic phosphorous (PCCC) and phosphorous oxide bonded to carbon (POCCC). This assignment is based on the similarity of the chemical shifts of these two peaks with those of triphenylphosphine (7.3 ppm) and triphenylphosphine oxide (29.4 ppm). Therefore, according to solid-state ^{31}P NMR spectroscopy, samples mp-(P)C contain two types of families for P atoms depending on whether there is residual oxygen or not in the phosphorous. The presence of oxygen would correspond to a partial reduction of the phosphate groups during the pyrolysis due to the strong reductive conditions.

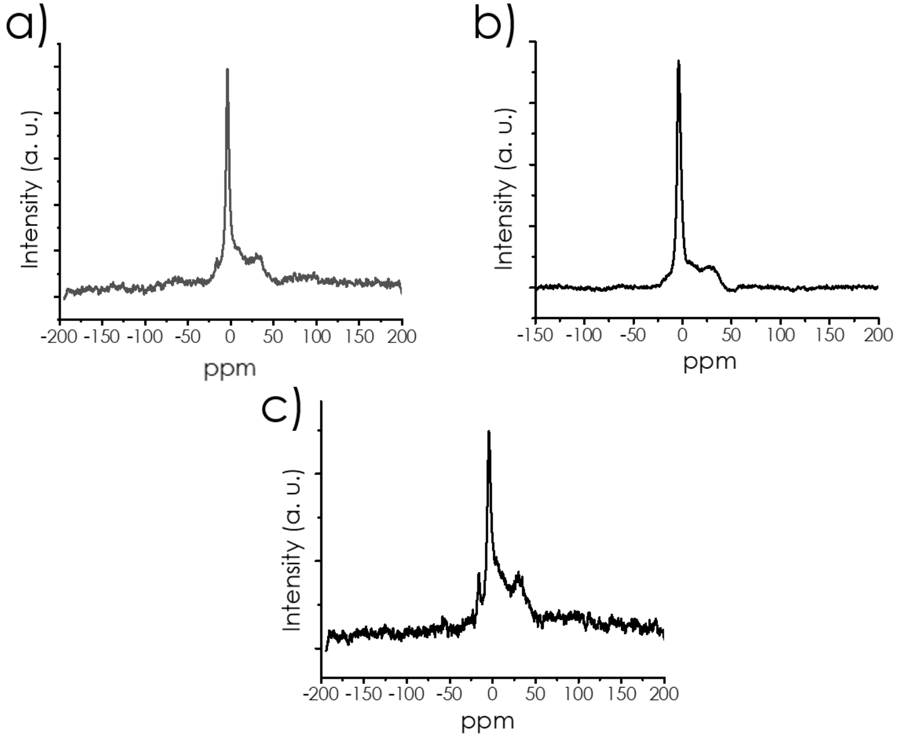

Figure 4.10. Solid state MAS ^{31} P NMR spectra of a) C_α-2, b) C_β-2, and c) C_γ-2.

The coordination of carbon and phosphorous atoms and the distribution among various coordination spheres was determined by XPS spectroscopy. Figure 4.11 shows the high-resolution C1s and P2p peaks determined by XPS, as well as the best deconvolution to individual components with the corresponding coordination and binding energy values. As can be seen in these figures, the carbon 1s peak can be adequately deconvoluted in 3 components appearing at 283.6, 284.5, and 288.0 eV, corresponding respectively to carbon atoms bonded to phosphorous, graphitic carbon, and carboxylate groups,[31] respectively. The two first components accounted for over 90% of the total carbon atoms. Also, the presence of phosphorous as a dopant element can be confirmed indirectly by observation of the carbon atoms bonded to phosphorous that appear at lower binding energies values than graphitic carbon or carbon bonded to oxygen.

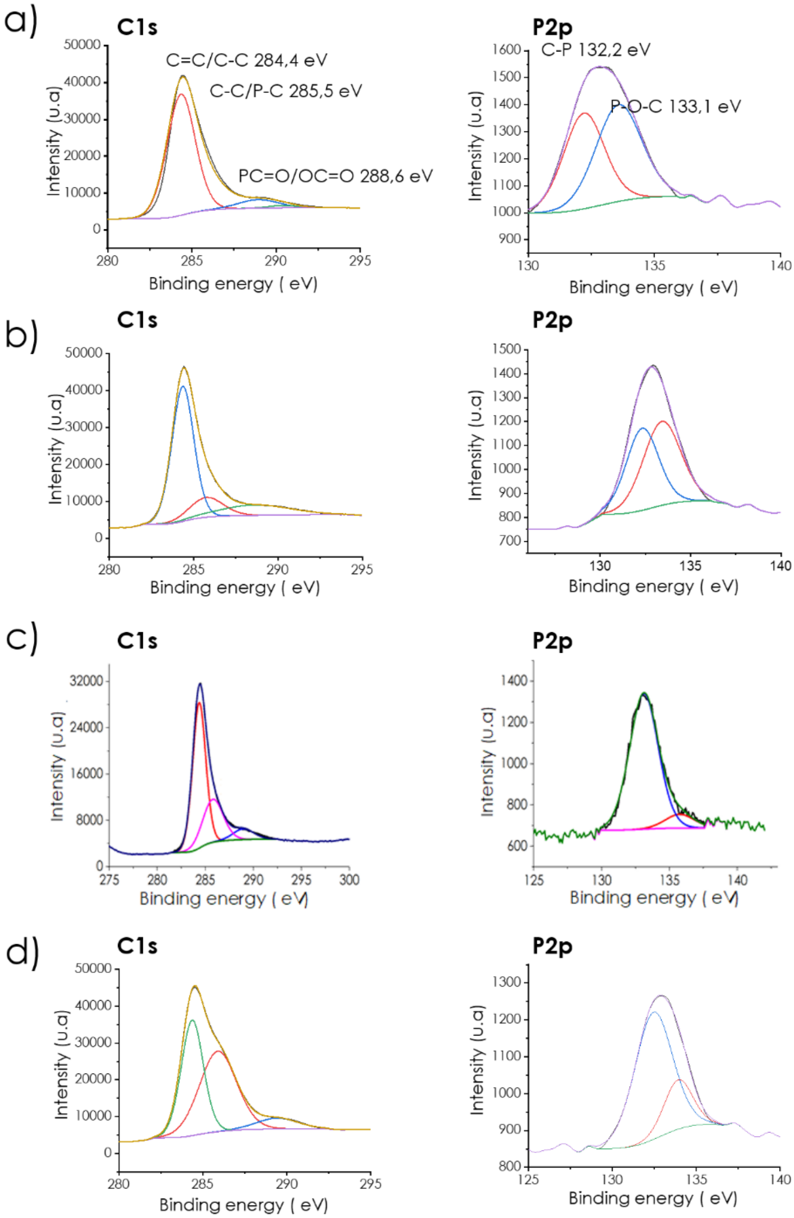

Figure 4.11. High-resolution XPS C1s and P 2p peaks and their best fit to individual components obtained for the samples a) (P)C$_{\alpha}$-2, b) (P)C$_{\alpha}$-4, c) (P)C$_{\beta}$-2, and d) (P)C$_{\gamma}$-2.

Following the previously commented solid-state ^{31}P NMR spectroscopy, XPS analysis also reveals the presence of two different phosphorous families. Deconvolution of the experimental high-resolution XPS P2p peak indicates the presence of two components with binding energies of 131.5 and 132.8 eV attributable to graphitic P and graphitic P oxide, respectively. The proportion of the two types of phosphorous is approximately 40 to 60 for graphitic and oxide, respectively.

For the use of mp-(P)C as a photocatalyst, one important characterization is optical adsorption spectroscopy since it can provide the optical band gap of the materials. The optical band gap is determined by the Tauc plots of the diffuse reflectance UV-Vis absorption spectra. They are shown in Figure 4.12 with the corresponding Tauc plots, assuming they are indirect band semiconductors. These band gap energy characterizations are tabulated in Table 4.1. As can be seen there, the band gap of the samples varies from 3.01 to 4.5 eV for samples (P)C$_\gamma$-2 and (P)C$_\alpha$-1, respectively. The band gap, together with XPS data on the valence band edges of the materials, can be used to determine the conduction band edge.

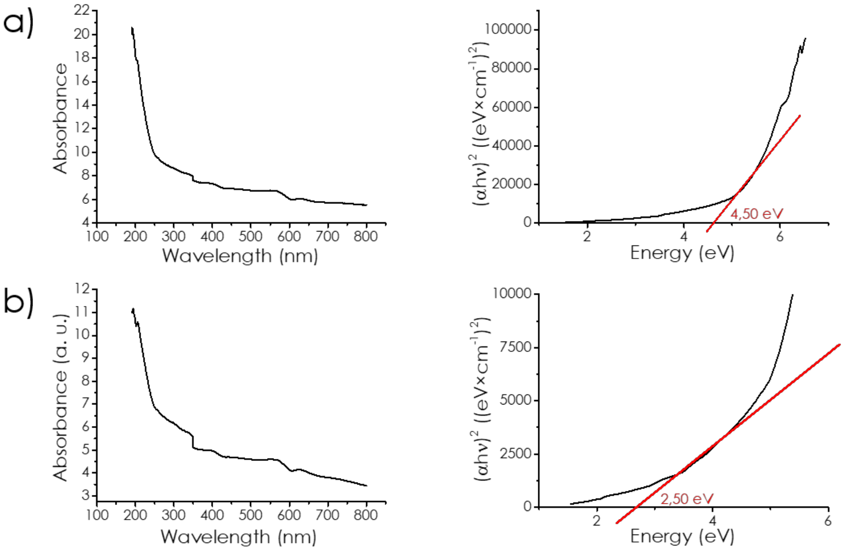

Figure 4.12. Diffuse reflectance UV-Vis absorption spectra and Tauc plots and optical band gap of the samples a) (P)C$_\alpha$-1, b) (P)C$_\alpha$-2.

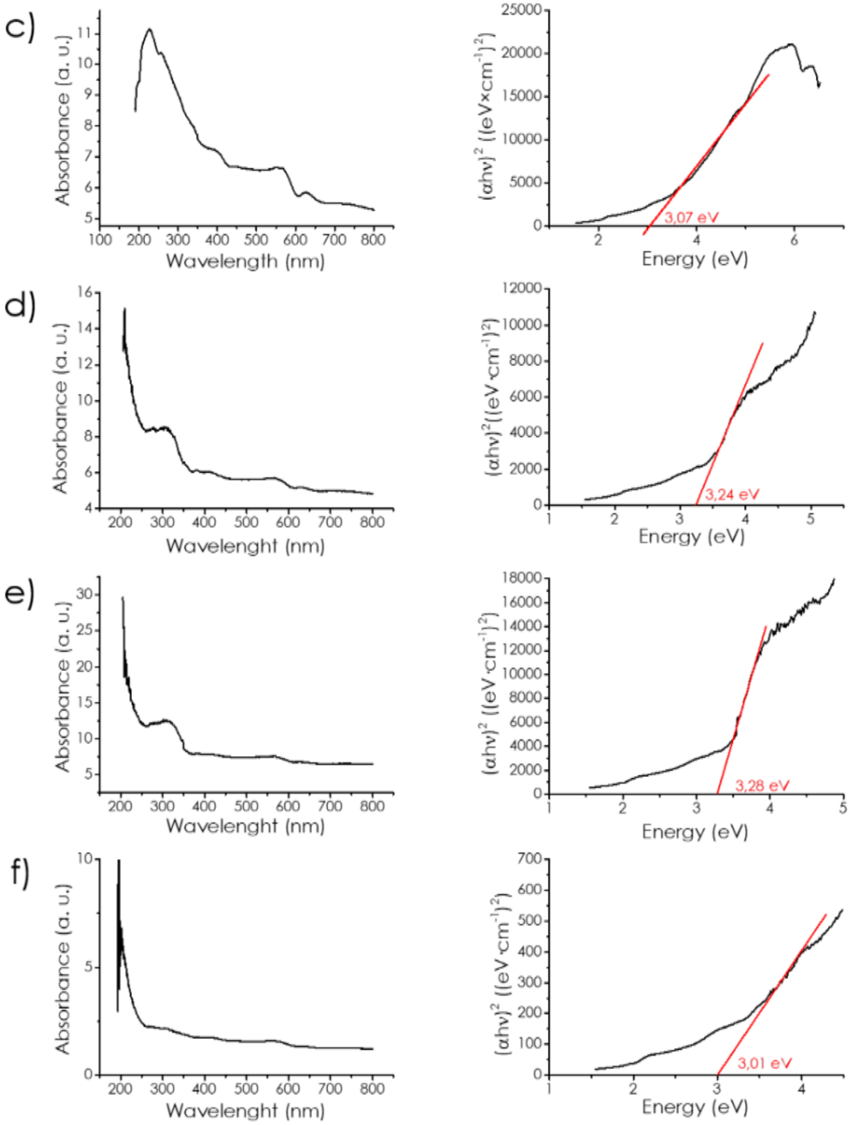

Figure 4.11 (cont). Diffuse reflectance UV-Vis absorption spectra and Tauc plots and optical band gap of the samples c) (P)C$_\alpha$-3, d) (P)C$_\alpha$-4, e) (P)C$_\beta$-2 and f) (P)C$_\gamma$-2.

As an example, Figure 4.13 shows the valence band edge of the most active (P)C$_\alpha$-2 material. This experimental value has to be corrected according to the work function of the instrument, which was determined using silver and gold work functions for calibration, resulting in a value of 4.244 eV.

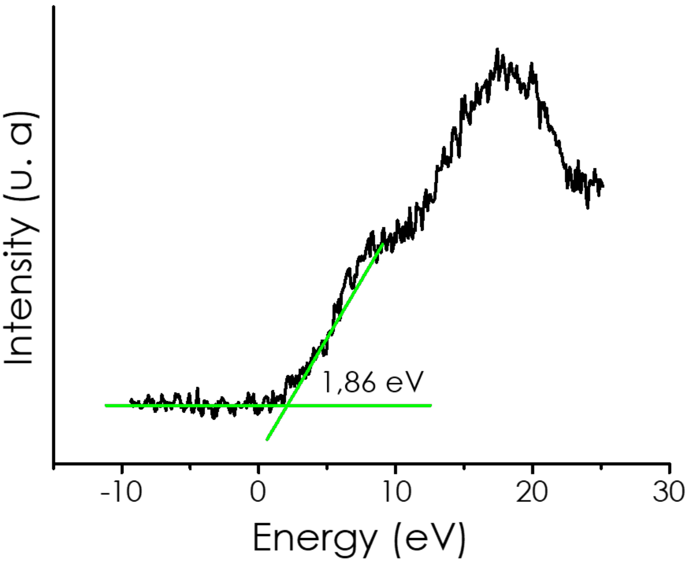

Figure 4.13.Determination of the valence band from the XPS spectra for the sample (P)C$_\alpha$-2.

These valence band edge values can be corrected with respect to the normal hydrogen electron scale by subtracting 4.44 eV, which corresponds to the vacuum level. Equation 4.1 illustrates the calculation used to determine the valence band edges of the materials under study.

$$E_v^{NHE} = E_v^{fv} + \varphi_{sp} - 4.44 \qquad \text{Eq. 4.1}$$

After determining the optical band gap and the valence band edge, it is possible to set the conduction band. Figure 4.14 presents the energy of the conduction and valence band for some of the materials under study, including the reported value for the non-doped mp-C$_\alpha$. Figure 4.14 also includes for reference the relevant potential for water oxidation at 0 and neutral pH and water reduction at the same pH values. From this figure, it can be concluded that the presence of phosphorous increases the value of the valence band potential, which can be interpreted considering that the lone electron pairs of P atoms are contributing to the energy of this valence band edge. The presence of P atoms also increases the conduction band energy in different amounts depending on the phosphorous content. As a general trend, it appears that an increase in phosphorous diminishes the energy of the conduction band. It should be noted at this point that the target of the present chapter was to show how the presence of phosphorous doping is able to modify the frontier orbitals of semiconducting carbons. The semiconducting nature of the mp-(P)C was also confirmed by observation of photoluminescence from (P)C_α too, as presented in Figure 4.15.

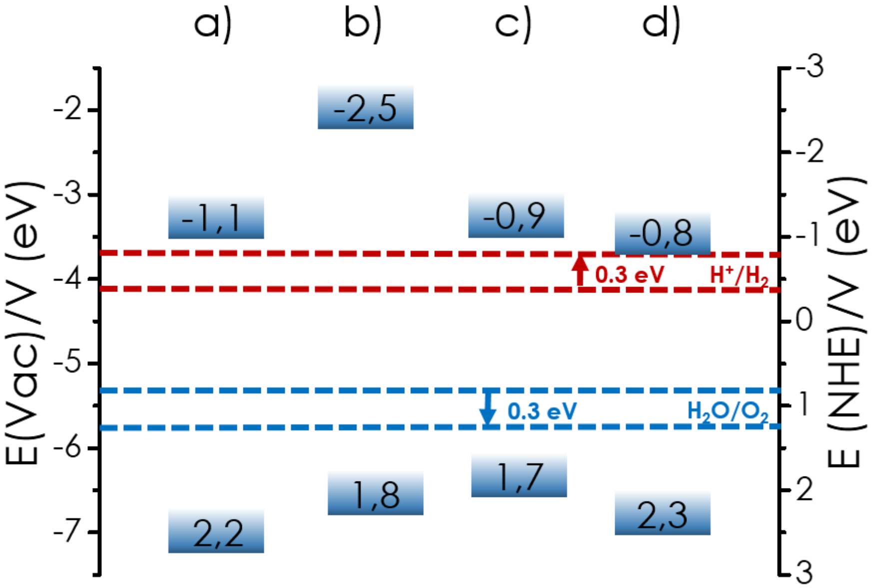

Figure 4.14. Valence and conduction band energy values for a) C_α, b) (P)C_α-1, c) (P)C_α-2, and d) (P)C_α-3; compared with the thermodynamic values of HER and OER potentials at neutral pH and overpotentials.

Data from Figure 4.14 confirm the possibility to have a certain control on the valence and conduction band of semiconducting microporous carbons by introducing P as a dopant element. According to Figure 4.14, all the (P)C_α materials have conduction and valence band energies to promote hydrogen and oxygen evolution from water at neutral pH. This energy diagram is compatible with the experimental observation of photocatalytic overall water splitting in all the (P)C_α samples. Moreover, this diagram also justifies the higher activity of the sample (P)C_α-2 due to the optimal alignment with respect to the overall water splitting potentials. Thus, (P)C_α-2 having a narrow band gap has the conduction band a few mV more negative than that required for HER and the valence band a few mV more positive than the OER. Therefore, having an overpotential of about ± 0.3 V to overcome kinetic barriers. In comparison, another sample such as (P)C_α-1 has too much broadband gap, meaning that the number of harvested photons, particularly in the visible light region, should be lesser, while in contrast, (P)C$_\alpha$-3 has a lesser overpotential for HER, particularly at neutral pH values.

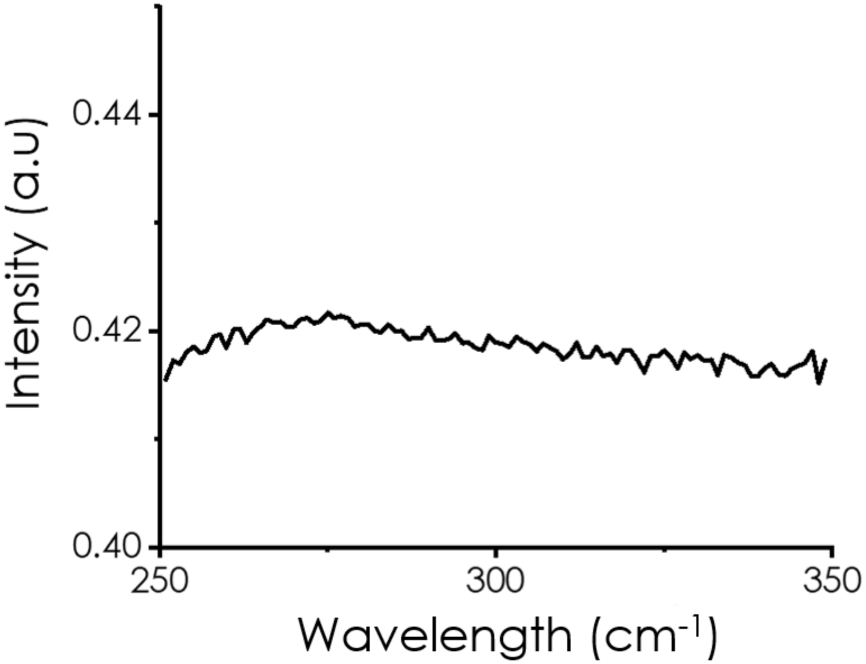

Figure 4.15. Photoluminescence spectrum of (P)C$_\alpha$-2 suspended in acetonitrile in a concentration of 1 mg×mL^{-1} upon excitation at 240 nm.

The Nyquist plot representing the inverse of capacitance square versus polarization potential at various frequencies for electrons made of (P)C$_\alpha$-2 on the FTO electrode showed negative slopes, indicating that (P)C$_\alpha$-2 is a p-type semiconductor. The measurements were carried out in the range of frequencies from 1 to 2 kHz using Na_2SO_4 as electrolyte. Figure 4.16 presents the Nyquist plot as three different frequencies showing a common extrapolation point at a potential of +0.49 V versus Normal Hydrogen Electrode (NHE). This value that should correspond to the potential of the conduction band is much lower than that measured by XPS and presented in Figure 4.14. This discrepancy can be interpreted considering the presence in carbon material of intra-gap stages, which is proposed to be related to the presence of P as a dopant element in the material.

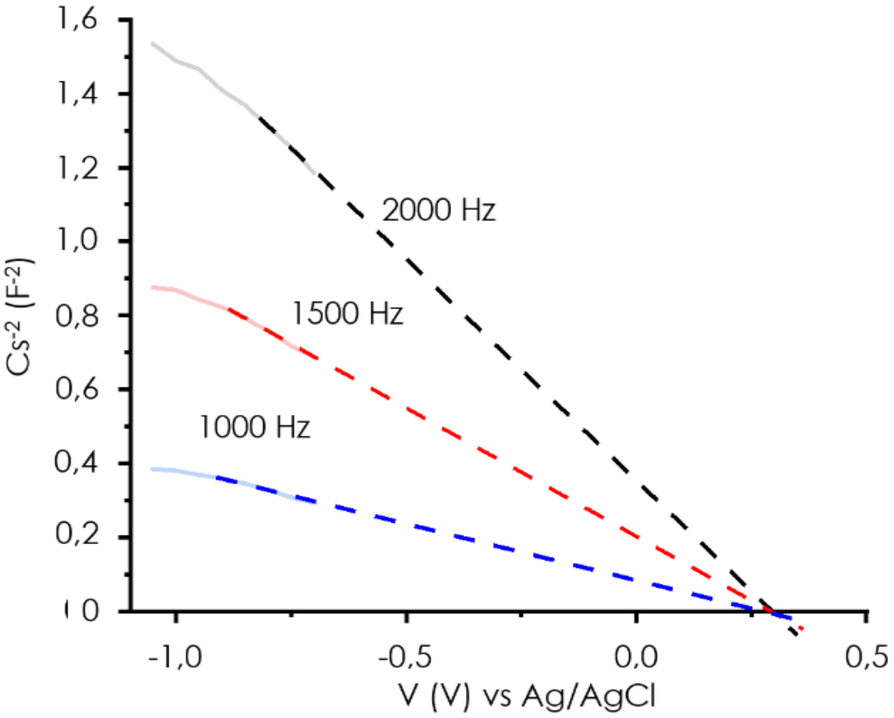

Figure 4.16. Nyquist plot of (P)C_α-2 on FTO using Na_2SO_4 1 M at three different frequencies.

4.2.2 Photocatalytic hydrogen evolution in the presence of sacrificial electron donor

Photocatalytic measurements were carried out suspending in water the corresponding mp-(P)C photocatalyst in a sealed quarts vessel under continuous magnetic stirring upon irradiation with simulated sunlight of one sun power or Xe lamp 300 W with a power of 1.5 suns.

Initial control experiments in the dark under irradiation conditions reveal the evolution of low detectable amounts of hydrogen. It is proposed that this hydrogen derives from the presence in the material of residual quantities of elemental phosphorous that would undergo spontaneous oxidation by water resulting in the generation of some H_2.[23] Elemental phosphorous is reported to be formed during the formation of the graphitic carbon under pyrolysis conditions due to the reduction of phosphate. [23] The process is in accordance with the extreme reducing conditions occurring during the pyrolysis, with the evolution of CO_2 and CO. Our group has coined the term carbochemical reduction to indicate the reduction under similar conditions of transition metals such as Ni^{2+}, Cu^{2+}, and Au^{3+} that it can be reduced to the corresponding metallic element during the graphitization process. [14, 32-35] It is proposed that analogous chemical reduction of phosphate occurs during the pyrolysis forming some quantity of elemental phosphorous on the mp-(P)C_α. In addition, these elemental phosphorous can become incorporated into the graphitic carbon-paying form in the process. The amount of elemental phosphorous has to be very low since this non-metallic element sublimes at temperatures much lower than those of the pyrolysis. However, it should be commented that the dark hydrogen evolution was about 20 times lower than the amount of hydrogen measured in the photocatalytic experiments.

Initially, to determine the photocatalytic activity of the mp-(P)C materials, the experiments were carried out by adding methanol as a sacrificial hole quencher in a proportion of 1:4. Similar or lower values of hydrogen evolution were obtained by replacing methanol with ethanol or even triethanolamine. Figure 4.17 illustrates the temporal profile of hydrogen production for two different sacrificial agents. Optimization of the amount of (P)C_α to maximize hydrogen evolution shows no relationship between the mass of photocatalyst and hydrogen production to get an optimal amount of photocatalyst there being an optimal amount of photocatalyst to reach the highest hydrogen production. In the present case, the optimization of the photocatalyst mass was carried out for (P)C_α-2.

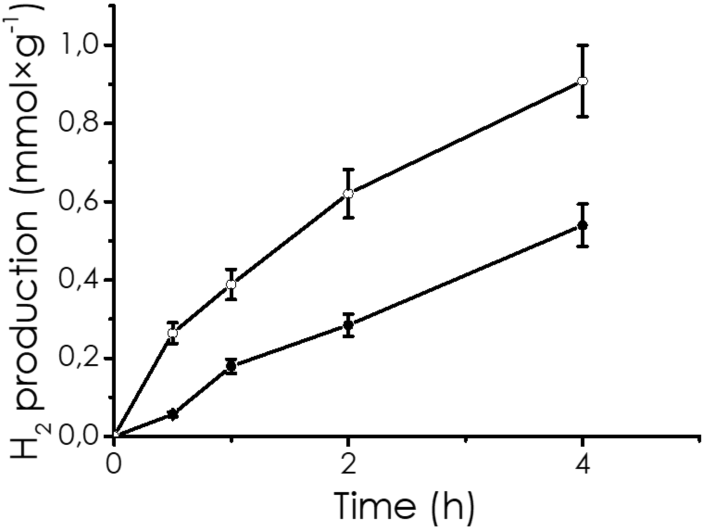

Figure 4.17. H_2 production using triethanolamine (●) or methanol (○) as electron donor under 300 W Xe lamp irradiation using the optimal amount of photocatalyst.

Figure 4.18 shows the temporal profile of hydrogen evolution in water: methanol 4:1 media for a series of concentrations between 0.1 and 2 mg of photocatalyst per mL. As can be seen in this figure, the maximum hydrogen evolution was measured for a concentration of 0.5 mg of (P)C_α-2 per milliliter that evolves 14 µmol of H_2 in 24 h. This corresponds to a production of 1.4 mmol of hydrogen per gram of photocatalyst. Higher and lower concentrations afford lower hydrogen production. These results respond to a well-known phenomenon in photocatalysis by opaque solids and are typically explained by the balance of two opposite factors: on the one hand, increasing the concentration of photocatalyst increases the amount of harvested photons. On the other hand, an increase in the amount of the opaque solid diminishes the transparency of the suspension, resulting in lower light penetration into the media.

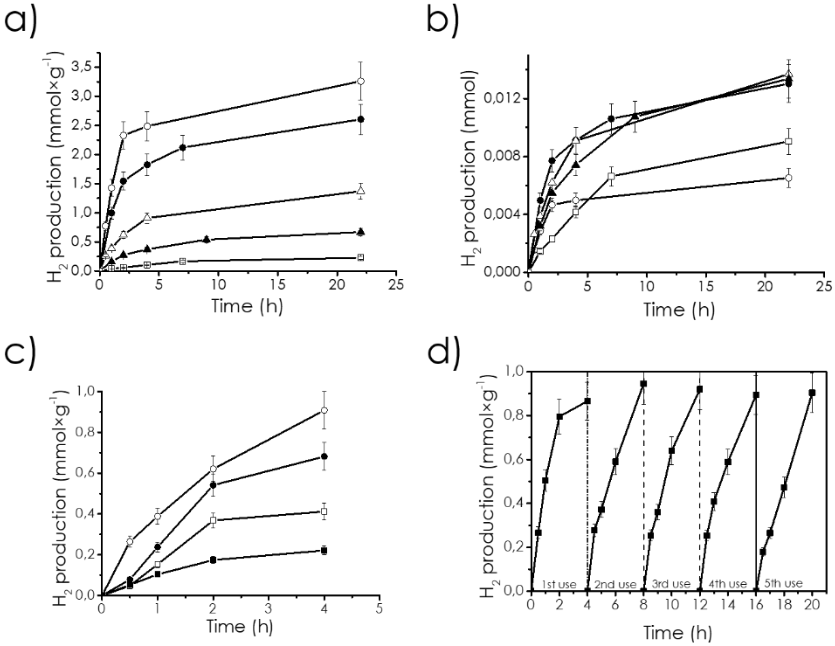

Figure 4.18. Temporal hydrogen evolution a) mmol of H_2 per gram or b) absolute evolution of H_2 using different concentrations of (P)C$_\alpha$-2 (○) 0.1 mg × mL^{-1}, (●) 0.25 mg × mL^{-1}, (△) 0.5 mg × mL^{-1}, (▲) 1 mg × mL^{-1}, and (□) 2 mg × mL^{-1}. c) H_2 evolution using mp-(P)C with different pore size at a concentration of 0.5 mg × mL^{-1}: (○) (P)C$_\alpha$-2, (●) (P)C$_\beta$-2, (□) (P)C$_\gamma$-2, and (■) mp-C$_\alpha$. d) Reuses of (P)C$_\alpha$-2.

At this point, it is worth commenting that photocatalytic activity is generally reported per gram of photocatalyst; even though the activity does not follow a linear relationship with photocatalyst mass, caution has to be taken when photocatalytic activity data are not given for the optimal photocatalyst mass. Thus, in the present case, if the activity is given per mass unit, the best value would be obtained using 0.1 mg of (P)C$_\alpha$-2 even though 5 times higher mass does not result in 5 times higher hydrogen production. In any case, the values shown in Figure 4.19 for hydrogen evolution in the presence of methanol are comparable with the values reported in the literature, despite of in the present case no metals are present in the composition of the material. For a metal-free photocatalyst, as in the present case, the hydrogen evolution values of Figure 4.19 are probably among the highest reported using simulated sunlight at 1 sun power. The previous considerations lead us to select a concentration of 0.5 mg of photocatalyst per mL that gives the highest absolute hydrogen evolution for subsequent photocatalytic measurements.

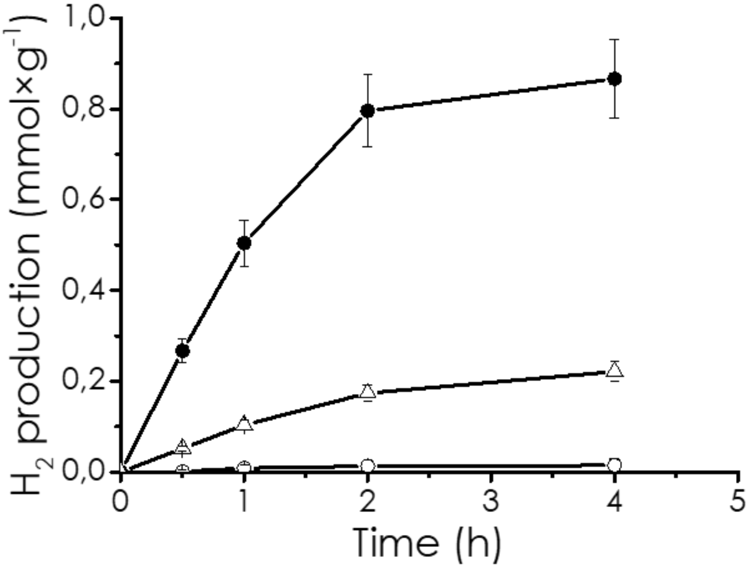

Figure 4.19. Temporal H_2 evolution profile for the sample (P)C$_\alpha$-2 (○) in dark conditions and (●) under irradiation with a Xe lamp with an AM 1.5 filter), (△) mp-Calpha; using a mixture 4:1 of H_2O:methanol.

The influence of P doping and its content was determined by performing the photocatalytic experiment of hydrogen evolution in the presence of methanol as a sacrificial electron donor. For this study, a sample of the microporous carbon prepared analogously but in the absence of phosphate was used for comparison. The results are presented in Figure 4.18. As can be seen there, all the (P)C$_\alpha$ samples results in higher hydrogen evolution than the control C$_\alpha$ microporous carbon devoid of phosphorous. It was found that the sample with the highest photocatalytic activity was (P)C$_\alpha$-2, higher or lower P percentages in the microporous carbon derived from α-cyclodextrin resulted in lesser hydrogen evolution. For the optimal phosphorous content, the photocatalytic activity increases by a factor of 5 concerning the graphitic carbon material without P doping. This result illustrates again that doping is a general strategy to increase the photocatalytic efficiency of carbonaceous materials. It is proposed that the beneficial impact of phosphorous derives from the variation of the optoelectronic properties of the material, such as band gap and frontier band energies.

The influence of pore size on the photocatalytic activity was determined by comparing the performance of a series of materials obtained by the pyrolysis of α-, β-, and γ-cyclodextrins at different phosphorous content. As expected, in the series for each cyclodextrin precursor, the photocatalytic efficiency depended on the P content, as it was observed for the mp-(P)C_α series. At the same or similar P doping, the photocatalytic activity consistently followed the order mp-(P)C_α>mp-(P)C_β>mp-(P)C_γ, indicating that the activity decreases as the pore size decreases. The same trend of the pore size has been observed previously for the photocatalytic activity for the undoped parent microporous graphitic carbon. This photocatalytic efficiency reflects the beneficial influence of confinement on photocatalytic activity. Thus, as the walls of the carbonaceous semiconductor are closer to the diameter of water, the electron transfers from the carbon to the water or vice versa becomes more favorable. This relative photocatalytic performance is consistently measured at any phosphorous content, suggesting that the two factors, P doping and pore size, are independent and can be used to optimize the efficiency of the photocatalyst. In this regard, it is worth commenting that the influence of doping on the photocatalytic activity appears to be less relevant as the pore diameter increases. Figure 4.20 summarizes the temporal hydrogen evolution for the various mp-(P)C samples prepared in the present chapter.

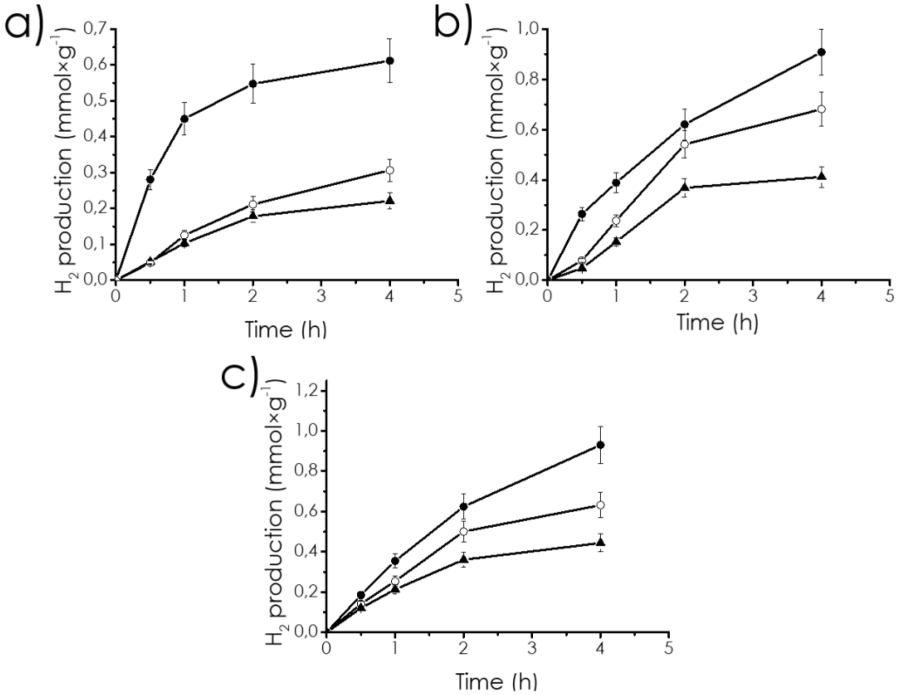

Figure 4.20. H_2 evolution for different P concentration for the 3 cyclodextrin precursor. a) lowamount of P (●) (P)C$_\alpha$-1, (○) (P)C$_\beta$-1 (80.9 % C, 0.1% P), (▲)(P)C$_\gamma$-1 (83.4 % C, 0.1% P); b) medium (●) (P)C$_\alpha$-2, (○) (P)C$_\beta$-2, (▲)(P)C$_\gamma$-2; and c) high amount of P (●) (P)C$_\alpha$-3, (○) (P)C$_\beta$-3 (70.2 % C, 2.1% P), (▲)(P)C$_\gamma$-1 (76.4 % C, 2.1% P).

As commented previously when discussing XPS and ^{31}P NMR spectroscopy, there are two different families of P atoms, differing in the presence or absence of oxygen bonded to P. It is reasonable to assume that variation in the distribution of the two populations of P atoms could affect the photocatalytic activity in H_2 generation. Therefore, it would be expected that the precursor of P atoms in the synthesis of the P-doped carbon can play a role in the distribution of these two P types. Thus, it can be considered that for certain P precursors could be easier to reduce P atoms to graphitic phosphorous, while other P compounds could be more reluctant to become reduced to this state. In addition, the acid properties of the P precursor can also lead to changes in the surface area of the material, as is the case. Table 4.1 shows that the surface area of (P)C$_\alpha$-4 derived from phytic acid is smaller than that obtained from phosphoric acid. To address the influence of this precursor, we prepared an additional sample using phytic acid instead of phosphoric acid as the source of P. As expected, the two materials exhibited different photocatalytic activity, the most efficient being the one obtained from phosphoric acid. The results are presented in Figure 4.21. Since no advantage of using the more expensive phytic acid as a precursor was found, further studies were carried out with samples obtained using phosphoric acid P source.

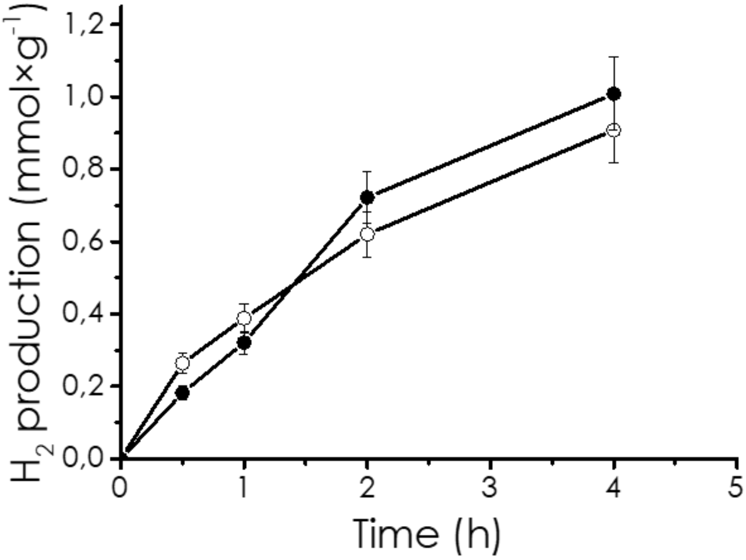

Figure 4.21. Comparison of the H_2 production for the materials prepared using different P source (●) (P)C$_\alpha$-2 (H_3PO_4 as precursor) and (○) (P)C$_\alpha$-4 (phytic acid as precursor).

The stability of the photocatalytic performance was confirmed for the most active material, (P)C$_\alpha$-2, by carrying out a series of consecutive photocatalytic experiments reusing the same sample. After each run, the solid was recovered from the suspension containing methanol and its oxidation by-products by centrifugation and washed with water, and used in subsequent runs. Figure 4.18 presents the temporal profiles in 5 consecutive irradiations. As can be seen in this figure, the initial reaction rate, final hydrogen production, and temporal profile remain substantially unaltered in this stability test. After the fifth use, the (P)C$_\alpha$-2 sample was recovered and submitted to characterization by XRD and HRTEM. Figure 4.22 provides the XRD patterns of the reused and fresh samples and an HRTEM image, including the pore diameter measurement of the five-times-used photocatalyst. Comparison of the characterization data of the five-time-used (P)C$_\alpha$-2 with that of the fresh material shows no differences, confirming again that the structure, morphology, and particle material size are not affected during the photocatalytic reaction.

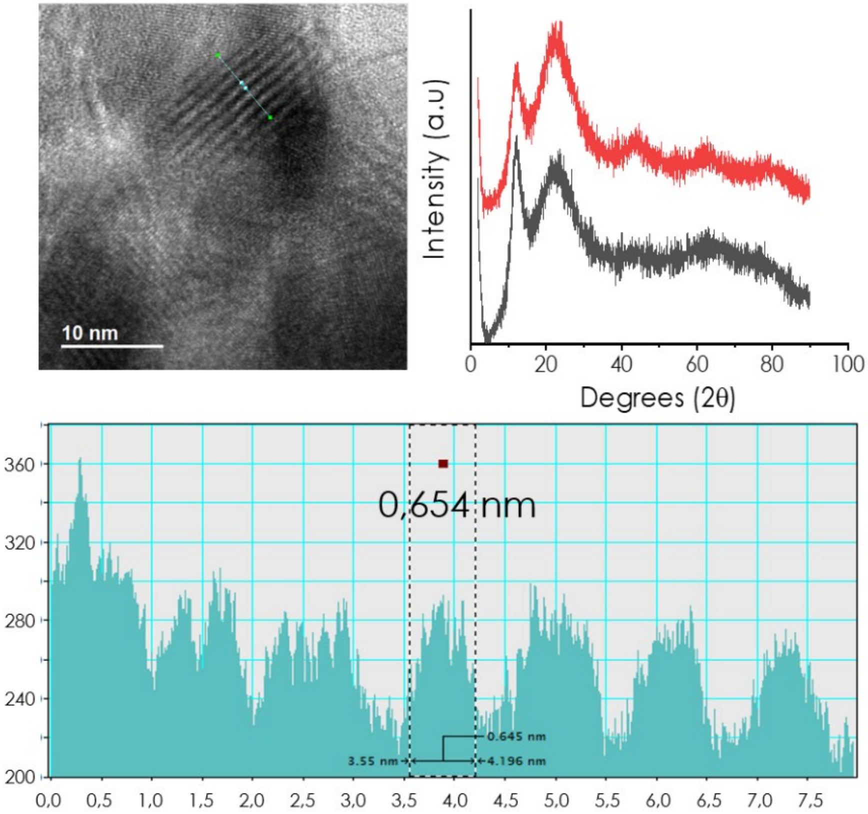

Figure 4.22. a) HRTEM image of the reused material with b) the corresponding pore size measurement. c) XRD pattern of the (P)C$_\alpha$-2 fresh (black) and after 5 consecutive uses (red).

The mp-(P)C under study are black powders, meaning that all photons in the visible range are adsorbed. However, it is frequently observed that the photocatalytic activity of carbon materials derives from certain spectral regions. The photoresponse of the (P)C$_\alpha$-2 was addressed by performing 3 irradiation experiments using either the full output of a Xe lamp through quartz (300 nm to near IR with similar energy for each wavelength); a solar simulator that contains photons from 380 nm (UVA, 4% of total energy) but a larger percentage of visible (40% of the energy) and near IR (66% of the total energy); and filtered light from the Xe lamp in which the UV irradiation and part of the blue light have been removed (λ >420 nm). After correction for the different light intensities (Xe lamp has higher power than 1 sun nominal power), the hydrogen evolution upon irradiation Xe or solar simulator was similar but more than double that of the visible irradiation. These results are presented in Figure 4.23. From this relative photocatalytic efficiency, we can conclude that (P)C$_\alpha$-2 has most of the photoresponse in the UVA and blue light region, although the material has a clear photoresponse, also for longer wavelength. This photoresponse is compatible with the estimated material's bandgap, which is about 3 eV. It is worth commenting that photocatalytic application in the production of hydrogen requires the use of solar light, and in this regard the results presented in Figure 4.23 a highly favorable in comparison with the usage of artificial sunlight.

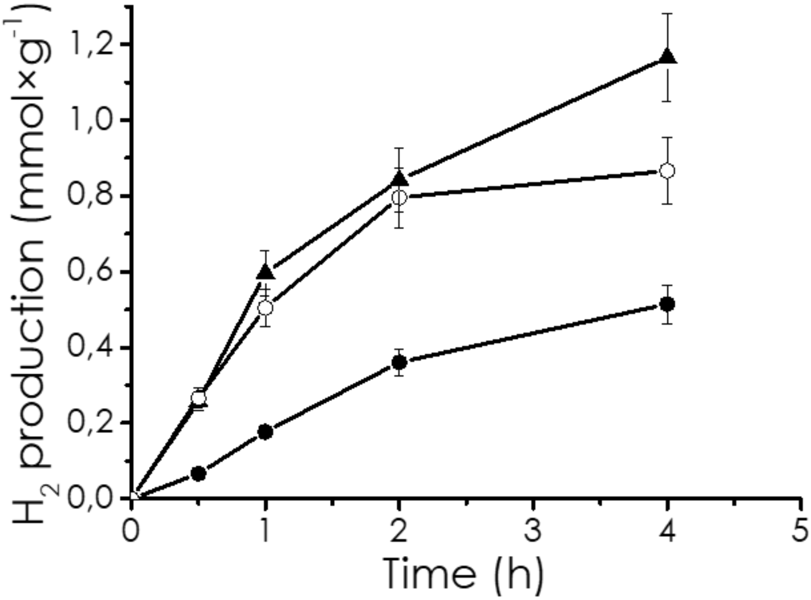

Figure 4.23. H_2 production using different light sources: (○) Xe lamp, (●) filtered Xe lamp (420 nm) and (▲) solar simulator, using methanol as electron donor and the optimal concentration of (P)C$_\alpha$-2.

4.2.3 Photocatalytic oxygen generation

Overall water splitting requires the combined and simultaneous HER and OER from water. In the previous section of this chapter, we have provided an extensive date on HER under very favorable conditions that correspond to the maximum possible rate for HER under the light spectral distribution and total power of the experiment. Therefore, to advance toward the possibility of photocatalytic overall water splitting, it is necessary to determine the maximum rate for OER under experimental conditions. These measurements were carried out by adding to the aqueous phase cerium ammonium nitrate to accelerate as much as possible conduction band electron quenching. Under these conditions, the rate of the OER can be measured. Among other possible established electron quenchers in photocatalysis, $Ce(NH_4)_2(NO_3)_6$ was selected since this solid does not produce insoluble metal particles upon reduction by the conduction band electrons, the only expected change is the transformation of hydrate hydrated cerium form into Ce^{3+}. That should produce a minor yellow tint of the solution. The results are presented in Figure 4.24. As can be seen there, in the presence of $Ce(NH_4)_2(NO_3)_6$, the evolution of O_2 upon irradiation of (P)C_α-2 was observed, reaching a production of 0.13 mmol×g^{-1} at 4 h. This production value is much lower than that achieved in the most favorable HER conditions, which is about 2.25 mmol× g^{-1} at 4 hours. This relative evolution rate for hydrogen and oxygen reflects the much slower kinetics of OER as compared to HER under the reaction conditions as it is universally found in the literature. The reason for the lower rate for OER is the requirement of 4 consecutive holes and the formation of O-O bond in the mechanism.

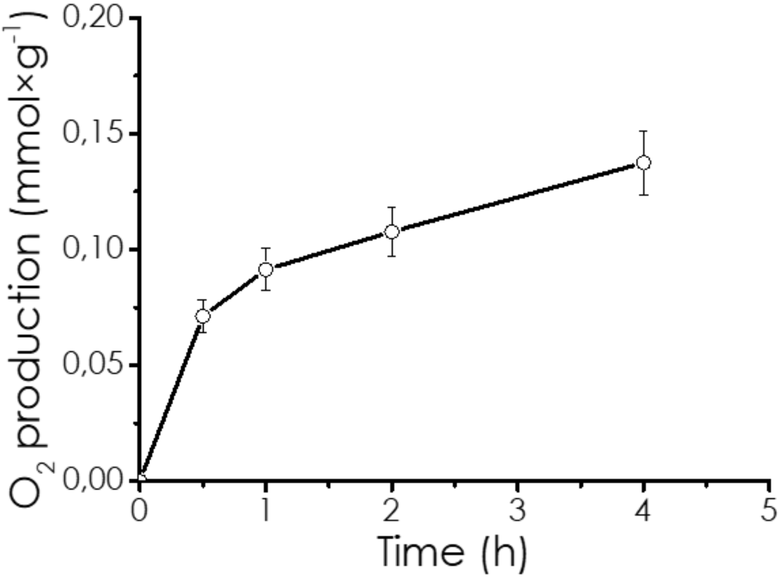

Figure 4.24. O_2 evolution using Ce^{IV} as electron acceptor.

4.2.4 Photocatalytic overall water splitting

After having studied independently HER and OER under the corresponding most favorable conditions, photocatalytic overall water splitting of pure H_2 in the absence of any additive was carried out using the best photocatalyst in this series and under simulated sunlight. As presented in Figure 4.25, while H_2 evolution started at the initial time, the presence of evolved oxygen was not detectable until 2 hours of irradiation. This would indicate that at the beginning of the photocatalytic experiment photogenerated holes or the nascent oxygen molecules are consumed by some quencher present in the system, phosphorous being an obvious one. In the literature, it is commonly observed that hydrogen and oxygen evolution does not follow strictly stoichiometric proportions and this has been attributed to spurious oxidation processes. In the present case, it could also be that oxygen is preferentially absorbed into the micropores of (P)C_α-2 with respect to hydrogen. In any case, at a longer reaction time, the amount of oxygen formed is also quasi-stoichiometric with respect to the amount of H_2 evolved. It should be noted at this point that after 20 hours of irradiation 300 µmol H_2× g^{-1} of catalyst was achieved. Although this value may not seem high compared to other photocatalysts in which hydrogen productions, over 1 mmolH_2 × g^{-1} at 2 hours of irradiation with simulated sunlight are achieved, it should be considered that in the present case, no metals are present. It is well known in the state of the art that the deposition of metal nanoparticles and metal oxides on the semiconductor favors considerably, sometimes even 2 order of magnitude, overall water splitting When comparing photocatalytic efficiency, it should be taken into account that no metals or metal oxides have been deposited on (P)C_{α}-2.

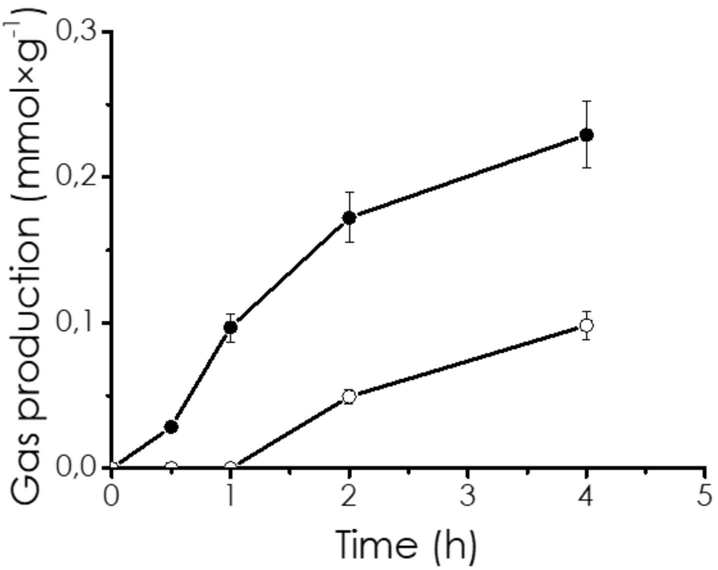

Figure 4.25. Gas evolution of the overall water splitting (●) H_2 and (○) O_2.

To provide a better assessment of the efficiency of (P)C_{α}-2 photocatalyst, the apparent quantum yield for overall water splitting was determined using monochromatic light, giving a value of 1.16% at 300 nm. It should also be commented here that a target in the area is to achieve overall solar energy to the hydrogen conversion efficiency of 5% since above this limit is considered that the process would be economically available.

Comparing the hydrogen evolution in the absence and presence of methanol a decrease in the hydrogen amount of about 6 times is determined. Figure 4.26 shows the temporal profiles of hydrogen evolution under these conditions. This decrease is due to the slow rate of OER, comparing oxygen production in overall water splitting or in the presence of cerium ammonium nitrate comparatively similar values are measured. These considerations reinforce again in the previous comments that it is OER the slower photocatalytic process that is limiting the efficiency of overall water splitting.

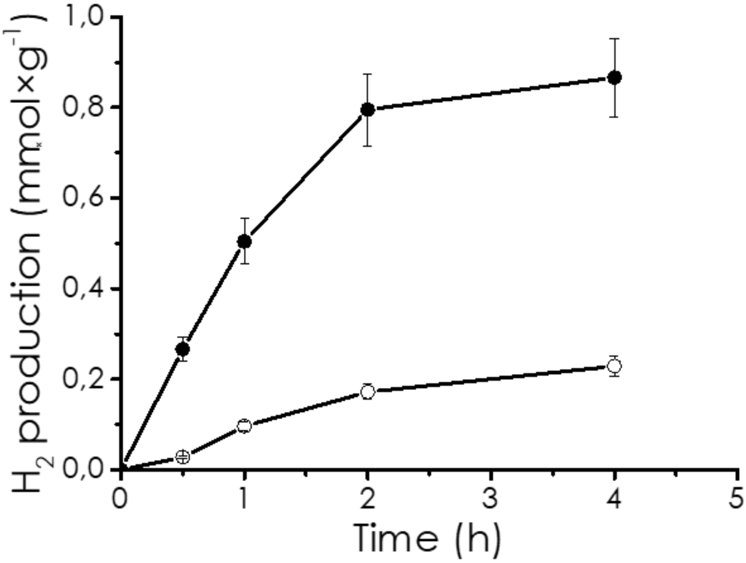

Figure 4.26. H_2 production (●) with electron donor and (○) overall reaction under 300 W Xe lamp irradiation, with the optimal amount of photocatalyst.

4.2.5 Metal or metal oxide photodeposition

Upon light absorption of a semiconductor, a photoinduced charge separation state is generated. This transient state in which electrons populate the conduction band and electron-holes generated in the valence band is crucial in photocatalysis. One of the best experimental evidence to convincingly demonstrate charge separation is metal or metal-oxide photodeposition. [36] In these experiments, a soluble metal salt is present during the illumination of the photocatalyst together with a sacrificial agent that provides electrons or quenches the photogenerated electrons. Under these circumstances, depending on the metal salt reduction or oxidation resulting in the formation of insoluble particles occurs. The detection of these photogenerated metal or metal oxide nanoparticles by electron microscopy constitutes firm experimental support of the occurrence for charge separation. Furthermore, in certain semiconductors with special morphology, a different location of the metal nanoparticles formed by reduction and metal oxides produced by oxidation have been observed. This different location has been correlated with the crystallographic planes of the semiconductor and has been justified by a different preferential migration of electrons and holes through the well-defined crystal.

Typical combinations in photodeposition are the use of noble metals such as platinum and gold and some proportion of methanol as an electron donor. Upon illumination, conduction band electrons reduce the noble metal, while holes are quenched by methanol or an amine. This photodeposition is very convenient considering the tendency of noble metal to undergo reduction and the stability of the resulting noble metal nanoparticles that, on the other hand, are easily detectable by electron microscopy due to their high atomic mass. [36]

Photodeposition to determine the generation of holes is less frequently reported in the literature. In this process, a meal ion soluble in water in lower oxidation states becomes oxidized to a higher oxidation state that, immediately in water, becomes hydrolyzed to the corresponding metal oxide that is insoluble and forms a particle in the place in which holes are located. Typical combinations are second-row transition metals, particularly Ru^{2+} which becomes oxidized to RuO_2. [37] In these photodeposition experiments, oxygen is the electron quencher and, therefore, they are performed in the open ambient. In the present case, due to the morphology of the $(P)C_{\alpha}$-2 photocatalyst, no special preferential deposition for oxidation and reduction should be expected.

In the present case, photodeposition of Pt nanoparticles was carried out starting with 1 mM aqueous solution of K_2PtCl_3 adding 20 % (v:v) of methanol. The system was purged by Ar to avoid the presence of oxygen, and the irradiation was carried out with visible light for 15 min. After this time, the solid was collected, washed, and submitted for chemical analysis, showing the presence of 0.12 % of Pt. Importantly, TEM images reveal the presence of Pt nanoparticles with an average size between 1 and 2 nm. Figure (8) presents a selected image showing the presence of Pt nanoparticles on the semiconductor. Importantly, a control experiment performed simultaneously in dark conditions shows the absence of Pt by analysis and the absence of nanoparticles by TEM.

Having Pt nanoparticles deposited on (P)C$_\alpha$-2, it was considered interesting to determine what is the influence of this metal presence as a co-catalyst promoting hydrogen evolution. The results are presented in Figure 4.27, in which the temporal hydrogen evolution upon solar light irradiation in the presence of methanol accelerates the held process are presented. As it can be seen there, as expected, the presence of Pt nanoparticles favors somewhat the hydrogen evolution that under these conditions increases from 0.8 mmol H_2 x g^{-1} for the pristine (P)C$_\alpha$-2 to 1.3 mmol H_2 x g^{-1} for the Pt-modified (P)C$_\alpha$-2 at 4 hours of irradiation. This increment in hydrogen production is relatively minor compared to other cases reported in the literature in which a factor of 50 or higher has been reported for the enhancement of hydrogen evolution. Again, these results indicate that in the present case H_2 evolution is particularly favorable and not much accelerated by the presence of a noble metal co-catalyst managing reductive processes.

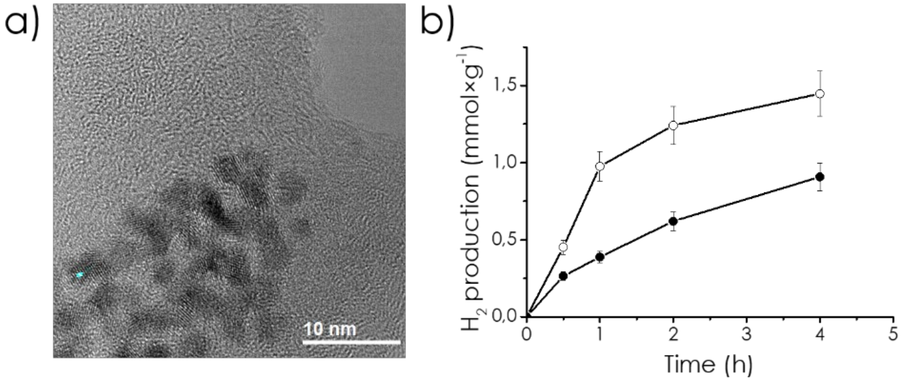

Figure 4.27. a) High-resolution transmission electron microscopy images of the photodeposited Pt on the photocatalyst, and b) H_2 evolution using (○) Pt/(P)C$_\alpha$-s and (●)C$_\alpha$-2.

To determine the formation of positive holes able to promote oxidations, an analogous photodeposition experiment with a 0.1 M aqueous solution of$CrCl_2$ was irradiated in the presence of (P)C$_\alpha$-2 as a photocatalyst in the open air for 15 min. At the end of the photodeposition experiment, the solid was collected and washed. EDS analysis indicates the presence of 0.13 % of Cr. Figure 4.28 shows the EDS analysis of the chromium deposited on (P)C$_\alpha$-2. This Cr_2O_3 being a transition metal oxide with various available redox states is suitable to act as a co-catalyst for oxygen evolution when deposited on (P)C$_\alpha$-2. For this reason, it was interesting to evaluate the performance of

Cr_2O_3/(P)C_α-2 as a photocatalyst for the mentioned reaction, using cerium ammonium nitrate as an electron acceptor. The results are presented in Figure 4.28. This figure shows that the O_2 evolution increases by a factor of 4 by the presence of Cr_2O_3 on the P-doped microporous carbon. Compared to the 1.5 enhancement on H_2 generation achieved by platinum deposition, the effect of Cr_2O_3 is significantly higher. This can be rationalized as explained earlier considering that the slowest semi reaction in overall water slitting is the OER and that, even though it is probably not the best, the presence of Cr_2O_3 nanoparticles accelerates this process.

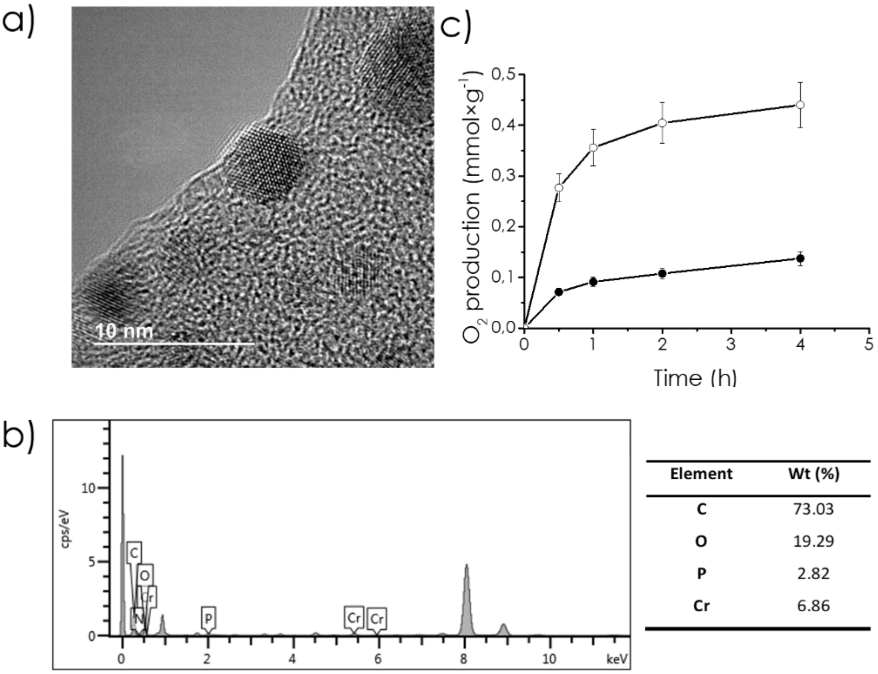

Element	Wt (%)
C	73.03
O	19.29
P	2.82
Cr	6.86

Figure 4.28. a) HRTEM image of the photodeposited Cr_2O_3 nanoparticles with b) its EDS analysis. c) O_2 production using Ce^{IV} as electron acceptor under irradiation (○) Cr_2O_3/(P)C_α-2 and (●) (P)C_α-2.

4.2.6 Photocurrent measurements

Electrochemical measurements by depositing photocatalyst on transparent conductive electrodes provide important information about redox processes in the material which are common in the photocatalytic and electrochemical processes. Cyclic voltammetry for (P)C_α-2 acquired in aqueous 1 M KCl electrolyte shows a reduction peak at -0.95 V and an oxidation peak at about 1.55 V to Ag/AgCl reference electrode. These redox peaks are probably related to the oxidation states of P and O heteroatoms grafted on electrically conductive graphitic carbon metrics. These 2 redox peaks are comprised of potential requirements for water discharge that have been observed with onset at -1.55 V vs Ag/AgCl for H_2 evolution and +2.0. V vs Ag/AgCl for oxygen evolution from water. Figure 10 presents the cyclic voltammetry measured for (P)C_α-2 electrode in which the two redox peaks due to the electrochemistry of the photocatalyst can be seen between the two major discharge peaks corresponding to water decomposition.

Deposition of the black (P)C_α-2 as a thin film on a transparent conductive FTO electrode allows also to determine the photocurrent generation upon illumination of these materials. Compared to photocatalytic studies, photocurrent measurements allow to easily determine the photoresponse of the material by measuring photocurrent intensity at different polarization potentials. The high sensitivity of current density measurement allows irradiation with much less intense light sources and specifically, the use of a monochromator to determine the current generated at each specific wavelength. In the present case, the current (P)C_α-2 electrode follows the same sense as that of an analogous electrode made by TiO_2, indicating that (P)C_α-2 is an n-type semiconductor, in which electrons in the conduction band are the faster charge carrier.

The photocurrent was determined by cycles of light on-light off of 1 min each, determining the increase in current intensity when the electrode is under illumination compared to the dark. This photocurrent depends on the light intensity, the nature and the amount of photocatalyst but also, on the polarization potential at which the photoelectrode is submitted. Figure 4.29 shows the evolution of the photocurrent as a function of the polarization potential. This polarization potential has to be in the window allowed by the water discharge previously commented that was determined by cyclic voltammetry. As can be seen in Figure 4.29, the polarization of the electrode was 0.60 V vs Ag/AgCl, and the photocurrent was very minor, even though observable, below 10 mA/g. This photocurrent increases in intensity along the polarization voltage, reaching a maximum when the polarization was +1.4 V, indicating that at this voltage or beyond all the possible charge carriers generated in the photoactive material have been extracted. Figure

4.29 also presents an expansion of the photocurrent compared to the dark current at 1 V polarization voltage.

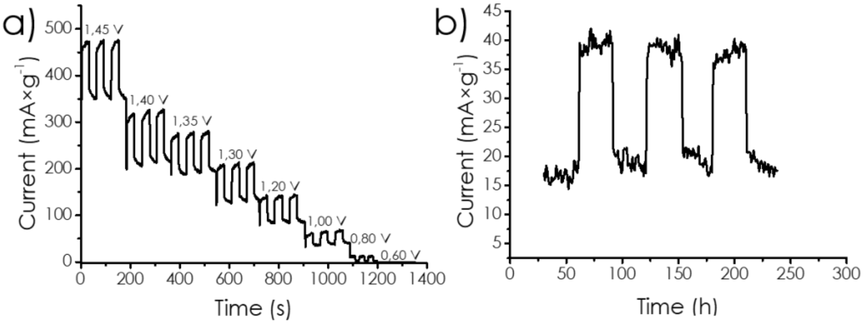

Figure 4.29. Linear chronoamperometric measurement of the sample (P)C$_{\alpha}$-2 and b) response in open circuit.

The performance of (P)C$_{\alpha}$-2 as an n-type semiconductor was supported by carrying out similar photocurrent measurements in the presence of Cerium ammonium nitrate as an electron quencher. If electrons in the conductions band are the major charge carrier with higher mobility in (P)C$_{\alpha}$-2, then, the presence in the electrolyte of Ce^{IV} should diminish the photocurrent by trapping some electrons from the photocatalyst that cannot be extracted to the external circuit. Figure 4.30 presents analogous photocurrent measurements as those previously measured in KCl electrolyte but having Ce (IV) in the solution. As shown in this figure, no photoresponse appears for polarization voltages below 1.00 V vs Ag/AgCl, and at higher polarization voltages the photocurrent magnitude was lower than in the absence of Ce (IV). For a better comparison, Figure 4.30 also shows the current density at 1.00 V vs Ag/. That is about 4 mA x g^{-1}, much lower than the 25 mA measured in the absence of Ce^{IV}.

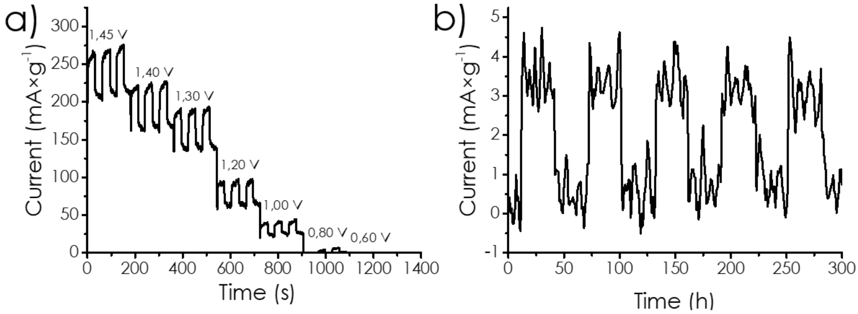

Figure 4.30. Linear chronoamperometric measurement of (P)C_α-2 and b) response in open circuit using Ce^{IV}.

The high sensitivity of the photocurrent measurement allows also to determine the photo response spectrum of the material. These photoaction spectrums are presented in Figure 4.31. As it can be seen there, two major responses, one in the UV at about 300 nm and the other in the visible at about 450 nm were measured. This response in the visible agrees with the photocatalytic experiments that also show the visible light response for (P)C_α-2. However, this visible light response maximum does not agree well with the optical absorption spectrum of (P)C_α-2, which does not exhibit any absorption band with maximum at 550 nm. To reconsider both contrasting experimental observations, i.e., a band with a maximum photo response of 550 nm and no corresponding optical adoption band at this wavelength we propose that this mismatch is due to a higher power of the excitation light at this wavelength that should provide more photons.

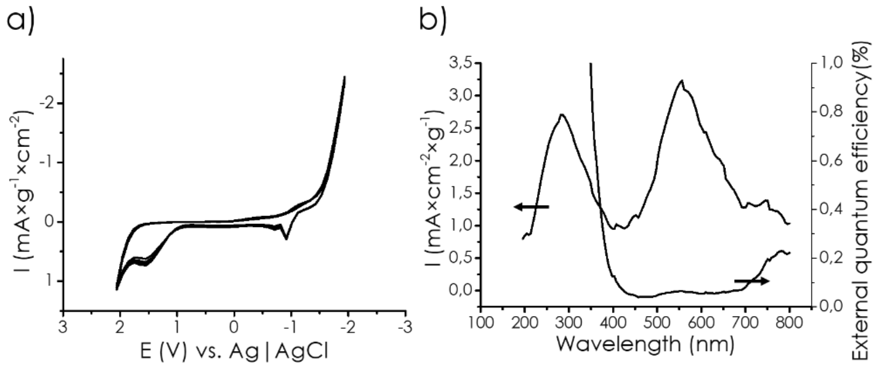

Figure 4.31. a) Cyclic voltammetry of P(C)$_{\alpha}$-2 in 1 M KCl electrolyte with scan rate of 20 mV × s^{-1} and b) Photoresponse (left axis) and external quantum efficiency (right axis) of a thin film deposited on FTO, scan rate 5 nm × s^{-1} with a 500 W Xe lamp coupled with aZolix Omni-λ300D monochromator.

The above electrochemical data with the experimental observation of photogeneration of charges, that can be extracted to the external circuit allows to propose a plausible mechanism for overall water splitting. This mechanism is sketched in Scheme 4.3 according to this proposal, photon adsorption in the UV or the visible region produces an electronic transition from the valence to the conduction band with the generation of an oxidizing hole and one electron with the potential to promote chemical reductions. In this way, the holes will cause water oxidation and oxygen evolution, while electrons in the conduction band will be responsible for the hydrogen evolution from water.

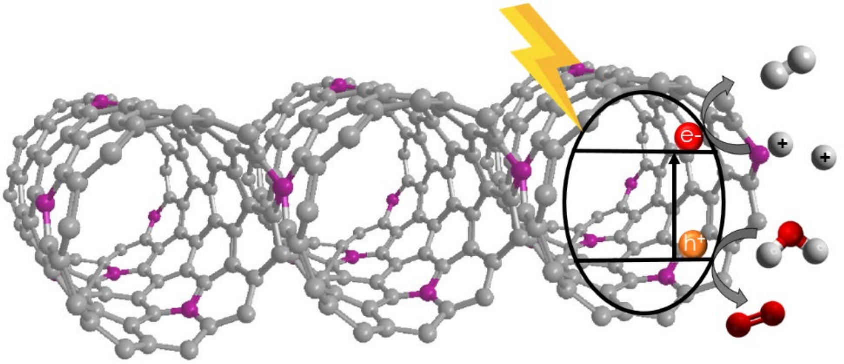

Scheme 4.3. Proposal of photocatalytic overall water splitting on P-doped microporous carbons.

4.3 Conclusions

The present results have illustrated the power of doping to tune the band gap potentials of microporous graphitic carbons derived from cyclodextrins pyrolysis in a certain range In general, it has been observed that phosphorous doping causes a larger influence on increasing the valence band maximum, a fact that can be rationalized considering the contribution of the p-lone electron pair to the valence band edge. In fact, by p-doping, the efficiency for H_2 generation in the presence of methanol as a sacrificial electron donor has been increased by a factor of 5.5 compared to the efficiency of the undoped microporous graphitic carbon, reaching a maximum hydrogen amount of 2.5 mmol × g^{-1} of catalyst at 24 h, irradiated with simulated sunlight for a photocatalyst concentration of 0.5 mg × mL^{-1}. This value is remarkable considering that this is a metal-free photocatalyst and that a significant proportion of the photocatalytic activity derives from photons of the visible region as can be seen in Figure 4.31. The P doped graphitic carbon photocatalyst is stable and reusable with no significant decay in its photocatalytic activity at the initial or final time and in the temporal evolution. The P-doped microporous carbons are also able to promote overall water splitting under simulated sunlight irradiation, reaching in 4 h production of 200 µmol × g^{-1} of catalyst. Kinetic evidence indicates that, as expected, the limiting semi reaction is oxygen evolution. This reaction can be increased by a factor of 5 by the photodeposition of Cr_2O_3 nanoparticles. Overall, the performance of the most efficient material derived from α-cyclodextrin pyrolysis compares favorably with that of related metal-free photocatalysts with graphene or graphitic carbon nitride structure. Table 4.2 provides a comparison between the hydrogen production of (P)C_α-2 and other metal-free photocatalysts previously reported. Although this comparison has to be taken cautiously due to unavoidable differences in the photoreactor set-up and reaction conditions, it can be concluded that with the present information the concept of doping can produce microporous graphitic carbon with high photocatalytic overall water splitting activity in the absence of metals.

Table 4.2. Comparison of the presented results about photocatalytic water splitting by (P)C$_\alpha$-2 in the optimal condition with the data reported in the literature.

Catalyst	Conditions	H_2 production (μmol × g^{-1} × L^{-1})	Ref
Phosphorous doped g-C_3N_4 (PCN)	0.5 g × L^{-1}, 1 wt% Pt, 10% TEOA, 300 W Xe lamp	2610.8	38
Boron doped C_3N_4nanodots/ P-doped C_3N_4	0.5 g × L^{-1}, 3 wt% Pt, 10 % TEOA, 300 W Xe lamp	2387.62	39
3D g-C_3N_4 NS	0.5 g × L^{-1}, 1 wt% Pt, 3 wt% IrO_2, no sacrificial agent, 300 W Xe lamp	101.4	40
RP/CN van der Waals	0.125 g × L^{-1}, no sacrificial agent, 300 W Xe lamp	367.0	41
Amorphous/ crystalline red phosphorous	0.5 g × L^{-1}, 5% methanol, 300 W Xe lamp	1.6	42
P-doped graphene	0.16 g × L^{-1}, 30% TEOA, 300W Xe lamp	100	23
Phosphorous doped graphene	0.2 g × L^{-1}, 0.75 M Na_2S and 1.05 M Na_2SO_3 (sacrificial reagents), 300 W Xe lamp	372.3	43
(P)C$_\alpha$-2	0.1 g × L^{-1}, 20% methanol, 300 W Xe lamp	622	44

4.4 References

1. Wang, Z.; Li, C.; Domen, K., Recent developments in heterogeneous photocatalysts for solar-driven overall water splitting. *Chemical Society Reviews* **2019,** *48* (7), 2109-2125.
2. George, W. C.; Mildred, S. D.; Michelle, V. B., The Hydrogen Economy. *Physics Today* **2004,** *57* (12), 39-44.
3. Fujishima, A.; Honda, K., Electrochemical Photolysis of Water at a Semiconductor Electrode. *Nature* **1972,** *238* (5358), 37-38.
4. Maeda, K.; Domen, K., Photocatalytic Water Splitting: Recent Progress and Future Challenges. *The Journal of Physical Chemistry Letters* **2010,** *1* (18), 2655-2661.
5. Comission, E. Raw materials, metals, minerals and forest-based industries: Critical raw materials. (accessed 16/09/2022).
6. Zhu, B.; Cheng, B.; Zhang, L.; Yu, J., Review on DFT calculation of s-triazine-based carbon nitride. *Carbon Energy* **2019,** *1* (1), 32-56.
7. Wang, X.; Blechert, S.; Antonietti, M., Polymeric Graphitic Carbon Nitride for Heterogeneous Photocatalysis. *ACS Catalysis* **2012,** *2* (8), 1596-1606.
8. Wang, X.; Maeda, K.; Thomas, A.; Takanabe, K.; Xin, G.; Carlsson, J. M.; Domen, K.; Antonietti, M., A metal-free polymeric photocatalyst for hydrogen production from water under visible light. *Nature materials* **2009,** *8* (1), 76-80.
9. Yang, J.; Wang, D.; Han, H.; Li, C., Roles of Cocatalysts in Photocatalysis and Photoelectrocatalysis. *Accounts of Chemical Research* **2013,** *46* (8), 1900-1909.
10. Xiang, Q.; Yu, J.; Jaroniec, M., Graphene-based semiconductor photocatalysts. *Chemical Society Reviews* **2012,** *41* (2), 782-796.
11. Albero, J.; Vidal, A.; Migani, A.; Concepción, P.; Blancafort, L.; García, H., Phosphorus-Doped Graphene as a Metal-Free Material for Thermochemical Water Reforming at Unusually Mild Conditions. *ACS Sustainable Chemistry & Engineering* **2019,** *7* (1), 838-846.
12. Yeh, T.-F.; Cihlář, J.; Chang, C.-Y.; Cheng, C.; Teng, H., Roles of graphene oxide in photocatalytic water splitting. *Materials Today* **2013,** *16* (3), 78-84.
13. Xiang, Q.; Cheng, B.; Yu, J., Graphene-Based Photocatalysts for Solar-Fuel Generation. *Angewandte Chemie International Edition* **2015,** *54* (39), 11350-11366.
14. Mateo, D.; Esteve-Adell, I.; Albero, J.; Royo, J. F. S.; Primo, A.; Garcia, H., 111 oriented gold nanoplatelets on multilayer graphene as visible light

photocatalyst for overall water splitting. *Nature Communications* **2016,** *7* (1), 11819.

15. Moissette, A.; Hureau, M.; Vezin, H.; Lobo, R. F., Chapter 14 - Electron Transfers Under Confinement in Channel-Type Zeolites. In *Chemistry of Silica and Zeolite-Based Materials*, Douhal, A.; Anpo, M., Eds. Elsevier: 2019; Vol. 2, pp 249-271.

16. Li, Z.; Jeanmairet, G.; Méndez-Morales, T.; Burbano, M.; Haefele, M.; Salanne, M., Confinement Effects on an Electron Transfer Reaction in Nanoporous Carbon Electrodes. *The Journal of Physical Chemistry Letters* **2017,** *8* (9), 1925-1931.

17. Primo, A.; Atienzar, P.; Sanchez, E.; Delgado, J. M.; García, H., From biomass wastes to large-area, high-quality, N-doped graphene: catalyst-free carbonization of chitosan coatings on arbitrary substrates. *Chemical Communications* **2012,** *48* (74), 9254-9256.

18. Peng, Y.; Rendón-Patiño, A.; Franconetti, A.; Albero, J.; Primo, A.; García, H., Photocatalytic Overall Water Splitting Activity of Templateless Structured Graphitic Nanoparticles Obtained from Cyclodextrins. *ACS Applied Energy Materials* **2020,** *3* (7), 6623-6632.

19. Rendón-Patiño, A.; Santiago-Portillo, A.; Vallés-Garcia, C.; Palomino, M.; Navalón, S.; Franconetti, A.; Primo, A.; Garcia, H., Templateless Synthesis of Ultra-Microporous 3D Graphitic Carbon from Cyclodextrins and Their Use as Selective Catalyst for Oxygen Activation. *Small Methods* **2020,** *4* (3), 1900721.

20. Putri, L. K.; Ong, W.-J.; Chang, W. S.; Chai, S.-P., Heteroatom doped graphene in photocatalysis: A review. *Applied Surface Science* **2015,** *358*, 2-14.

21. Yu, H.; Shi, R.; Zhao, Y.; Bian, T.; Zhao, Y.; Zhou, C.; Waterhouse, G. I. N.; Wu, L.-Z.; Tung, C.-H.; Zhang, T., Alkali-Assisted Synthesis of Nitrogen Deficient Graphitic Carbon Nitride with Tunable Band Structures for Efficient Visible-Light-Driven Hydrogen Evolution. *Advanced Materials* **2017,** *29* (16), 1605148.

22. Qi, Y.; Xu, J.; Wang, C.; Zhan, T.; Wang, L., Synthesis of Holey Graphitic Carbon Nitride with Highly Enhanced Photocatalytic Reduction Activity via Melamine-cyanuric Acid Precursor Route. *Chemical Research in Chinese Universities* **2020,** *36* (6), 1024-1031.

23. Latorre-Sánchez, M.; Primo, A.; García, H., P-Doped Graphene Obtained by Pyrolysis of Modified Alginate as a Photocatalyst for Hydrogen Generation from Water–Methanol Mixtures. *Angewandte Chemie International Edition* **2013,** *52* (45), 11813-11816.

24. Abellán, G.; Latorre-Sánchez, M.; Fornés, V.; Ribera, A.; García, H., Graphene as a carbon source effects the nanometallurgy of nickel in Ni,Mn layered double hydroxide–graphene oxide composites. *Chemical Communications* **2012,** *48* (93), 11416-11418.

25. Latorre-Sanchez, M.; Atienzar, P.; Abellán, G.; Puche, M.; Fornés, V.; Ribera, A.; García, H., The synthesis of a hybrid graphene–nickel/manganese mixed oxide and its performance in lithium-ion batteries. *Carbon* **2012,** *50* (2), 518-525.

26. Ferrari, A. C.; Meyer, J. C.; Scardaci, V.; Casiraghi, C.; Lazzeri, M.; Mauri, F.; Piscanec, S.; Jiang, D.; Novoselov, K. S.; Roth, S.; Geim, A. K., Raman Spectrum of Graphene and Graphene Layers. *Physical Review Letters* **2006,** *97* (18), 187401.

27. Primo, A.; Sánchez, E.; Delgado, J. M.; García, H., High-yield production of N-doped graphitic platelets by aqueous exfoliation of pyrolyzed chitosan. *Carbon* **2014,** *68*, 777-783.

28. Liou, Y.-J.; Huang, W.-J., Quantitative Analysis of Graphene Sheet Content in Wood Char Powders during Catalytic Pyrolysis. *Journal of Materials Science & Technology* **2013,** *29* (5), 406-410.

29. Tang, L.; Wang, Y.; Li, Y.; Feng, H.; Lu, J.; Li, J., Preparation, Structure, and Electrochemical Properties of Reduced Graphene Sheet Films. *Advanced Functional Materials* **2009,** *19* (17), 2782-2789.

30. Stobinski, L.; Lesiak, B.; Malolepszy, A.; Mazurkiewicz, M.; Mierzwa, B.; Zemek, J.; Jiricek, P.; Bieloshapka, I., Graphene oxide and reduced graphene oxide studied by the XRD, TEM and electron spectroscopy methods. *Journal of Electron Spectroscopy and Related Phenomena* **2014,** *195*, 145-154.

31. Rendón-Patiño, A.; Torres, F.; Primo, A.; García, H., Band gap alignment of structured microporous graphitic carbons by N doping and its influence on photocatalytic overall water splitting. *Sustainable Energy & Fuels* **2022,** *6* (9), 2170-2178.

32. Mateo, D.; Albero, J.; García, H., Graphene supported NiO/Ni nanoparticles as efficient photocatalyst for gas phase CO2 reduction with hydrogen. *Applied Catalysis B: Environmental* **2018,** *224*, 563-571.

33. Mateo, D.; Albero, J.; García, H., Photoassisted methanation using Cu2O nanoparticles supported on graphene as a photocatalyst. *Energy & Environmental Science* **2017,** *10* (11), 2392-2400.

34. Mateo, D.; Esteve-Adell, I.; Albero, J.; Primo, A.; García, H., Oriented 2.0.0 Cu2O nanoplatelets supported on few-layers graphene as efficient visible light photocatalyst for overall water splitting. *Applied Catalysis B: Environmental* **2017,** *201*, 582-590.

35. Neaţu, Ş.; Maciá-Agulló, J. A.; Concepción, P.; Garcia, H., Gold–Copper Nanoalloys Supported on TiO2 as Photocatalysts for CO2 Reduction by Water. *Journal of the American Chemical Society* **2014,** *136* (45), 15969-15976.

36. Jiang, Z.; Zhang, Z.; Shangguan, W.; Isaacs, M. A.; Durndell, L. J.; Parlett, C. M. A.; Lee, A. F., Photodeposition as a facile route to tunable Pt photocatalysts for hydrogen production: on the role of methanol. *Catalysis Science & Technology* **2016,** *6* (1), 81-88.

37. Wenderich, K.; Mul, G., Methods, Mechanism, and Applications of Photodeposition in Photocatalysis: A Review. *Chemical Reviews* **2016,** *116* (23), 14587-14619.

38. Fang, X.-X.; Ma, L.-B.; Liang, K.; Zhao, S.-J.; Jiang, Y.-F.; Ling, C.; Zhao, T.; Cheang, T.-Y.; Xu, A.-W., The doping of phosphorus atoms into graphitic carbon nitride for highly enhanced photocatalytic hydrogen evolution. *Journal of Materials Chemistry A* **2019,** *7* (18), 11506-11512.

39. Liu, M.; Jiao, Y.; Qin, J.; Li, Z.; Wang, J., Boron doped C3N4 nanodots/nonmetal element (S, P, F, Br) doped C3N4 nanosheets heterojunction with synergistic effect to boost the photocatalytic hydrogen production performance. *Applied Surface Science* **2021,** *541*, 148558.

40. Chen, X.; Shi, R.; Chen, Q.; Zhang, Z.; Jiang, W.; Zhu, Y.; Zhang, T., Three-dimensional porous g-C3N4 for highly efficient photocatalytic overall water splitting. *Nano Energy* **2019**.

41. Wang, M.; Qin, Z.; Diao, Z.; Li, R.; Zhong, J.; Ma, D.; Chen, Y., Red Phosphorus/Carbon Nitride van der Waals Heterostructure for Photocatalytic Pure Water Splitting under Wide-Spectrum Light Irradiation. *ACS Sustainable Chemistry & Engineering* **2020,** *8* (35), 13459-13466.

42. Wang, F.; Ng, W. K. H.; Yu, J. C.; Zhu, H.; Li, C.; Zhang, L.; Liu, Z.; Li, Q., Red phosphorus: An elemental photocatalyst for hydrogen formation from water. *Applied Catalysis B: Environmental* **2012,** *111-112*, 409-414.

43. Wu, Y.; Cao, C.; Qiao, C.; Wu, Y.; Yang, L.; Younas, W., Bandgap-tunable phosphorus-doped monolayer graphene with enhanced visible-light photocatalytic H2-production activity. *Journal of Materials Chemistry C* **2019,** *7* (34), 10613-10622.

44. Garcia-Mulero, A.; Asiri, A. M.; Albero, J.; Primo, A.; Garcia, H., All-carbon microporous graphitic photocatalyst-promoted reduction of CO2 to CO in the absence of metals or dopant elements. *Nanoscale* **2022,** *14* (32), 11575-11582.

CHAPTER 5.

ALL CARBON, METAL-FREE, AND DOPED MICROPOROUS GRAPHITIC CARBON AS PHOTOCATALYST FOR THE SELECTIVE CO_2 REDUCTION TO CO

5.1 Introduction

As commented in the introduction, photocatalysis has been dominated by transition metal semiconductors. [1-2] Still, for the sake of sustainability and proper use of resources, there is an increasing interest in developing metal-free photocatalysts, [3-6] particularly those based on the most abundant elements, such as carbon. [7] Graphitic carbon nitride and graphene-derived photocatalysts are two of the most widely studied metal-free photocatalyst. [8-11] In the previous chapter, we studied H_2 evolution from water in the presence and absence of an electron donor, showing that, for this particular reaction, doping with phosphorous increases the photocatalytic activity by a factor of 5 compared with the undoped material. The effect has been attributed to the presence of heteroatoms on conduction and valence band redox potential.

A logical evolution of these metal-free photocatalyst is to explore the photocatalytic efficiency of these materials for CO_2 reduction. In comparison with H_2 production from water, photocatalytic CO_2 reduction is more challenging due to the higher reduction potential needed for the process, the more complex reaction mechanism involving the concerted transfer of several electrons and protons, the lower CO_2 adsorption compared to water, and the possibility to obtain different products, including H_2 formed from water which is always simultaneously present during photocatalytic CO_2 reduction. [12] From previous studies, our group has shown that microporous graphitic carbons obtained by pyrolysis of cyclodextrins may exhibit higher catalytic and photocatalytic activity than analogous 2D graphenes due to the so-called confinement effect. [13-15] This effect derives from the proximity between the atoms of the porous material and the absorbed molecules when there is a tight fit between the incorporated guest with the host voids. The proximity favors interaction with the active sites and charge-transfer processes. For this reason, in agreement with the theoretical calculations, it has been observed that microporous carbons derived from the α-cyclodextrin are more efficient for H_2 generation and molecular oxygen activation than analogous materials derived from β- or γ- cyclodextrin. [13] According to this, it is also necessary to check if this confinement effect, in which pre-activation of the substrate within the micropores favors the chemical reaction, also operates in the case of photocatalytic CO_2 reduction. On the other hand, the effect of heteroatom doping on this photocatalytic reaction is also worth to be studied.

Therefore, the aim of this chapter is to describe the results of the photocatalytic activity of undoped and doped microporous graphitic carbons as selective photocatalysts under simulated sunlight irradiation for the selective reduction of CO_2 to CO. Following the trend already observed in Chapter 4 and the literature, a positive influence diminishing the pore dimension in the photocatalytic activity has been observed.

5.2 Results and discussion

As in the previous chapter, a series of microporous graphitic carbons were prepared by pyrolysis of α-, β- and γ-cyclodextrin, the series of samples under study were completed by also synthesizing two materials from α-cyclodextrin containing nitrogen or phosphorous as dopant elements. These heteroatoms were introduced by adding urea or phosphoric acid as precursors during the synthesis. The chemical composition of the samples was determined by elemental combustion chemical analysis and ICP-OES for the P-containing. As can be seen in Table 5.1. , and in agreement with previous results from the group, C_α is constituted mainly of carbon (over 98%) with some residual hydrogen (1%), meaning that oxygen should be almost absent in this material. In comparison, graphitic carbon derived from β- or γ-cyclodextrin should contain over 10% of oxygen atoms. The percentage of carbon decreases to 89 and about 87% for mp-C_β and mp-C_γ, respectively. This fact has been rationalized considering that the presence of oxygen in the structure generating defects requires larger pore dimensions to occur.

Table 5.1. Analytical data, surface area, and band gap of the materials under study.

Material	% C	% H	% N	% P	Surface area (m^2 x g^{-1})	Band gap (eV)
mp-C_α	98.2	1	0	0	572	3.3
mp-C_β	89.2	1.2	0	0	597	3.0
mp-C_γ	87.0	0.6	0	0	630	2.8
mp-(P)C_α	87.4	1.1	0	1.9	1928	3.1
mp-(N)C_α	80.9	0.9	3.4	0	540	2

The presence of nitrogen or phosphorous in mp-(N)C_α or mp-(P)C_α, respectively, was also quantified by chemical analysis. The introduction of nitrogen or phosphorous in the structure is also accompanied by a substantially increased oxygen content above 10%. This oxygen is associated partially with the dopant heteroatoms.

Isothermal N_2 adsorption was initially used to determine the specific surface area for undoped graphitic carbons. Figure 5.1 presents these measurements for mp-C_β and mp-C_γ. In the case of mp-C_α, no N_2 absorption was observed. This fact has already been reported and attributed to the small pore dimension of mp-C_α (0.64 nm) that impedes N_2 diffusion at the low temperature of the measurement (-196 °C). [16] For this reason, and to provide the datum of the porosity of mp-C_α, the specific surface area was also determined by CO_2 adsorption experiments at 0 °C. [16] Under these conditions, a specific surface of 572 m^2 x g^{-1} was determined. The specific surface area measurements for the samples under study determined in all cases with CO_2 adsorption are provided in Table 5.1. It worth noting that while for most of the samples the surface area is around 600 $m^2 \times g^{-1}$, in the case of the P-doped material, a surface area of about 2000 $m^2 \times g^{-1}$ was measured. It is proposed that this high surface area is derived from the effect of phosphoric acid during the pyrolysis that produces corrosion of the graphene walls with the generation of carbon vacancies and defects.

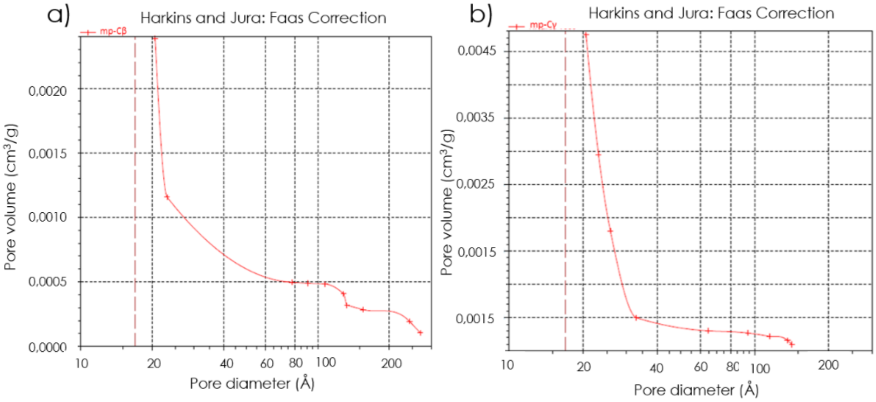

Figure 5.1. Pore distribution for a) mp-C_β and b) mp-C_γ, measured from the isothermal N_2 desorption branch.

The graphitic nature of the materials was easily demonstrated by Raman spectroscopy. Figure 5.2 shows the Raman spectra of the samples under study. As can be seen, they were almost coincident in shape and also very similar to those previously reported for defective graphenes derived from the pyrolysis of polysaccharides. [17] These spectra present 3 bands, corresponding to the G and D bands of defective graphenes and their overtones. In our case, the G band appears as a narrower peak at 1590 cm^{-1}, while the D band is broader and is unresolved with the G band, being recorded at about 1350 cm^{-1}. The overtones are registered as a much less intense and wider adsorption band from 2500 to 3200 cm^{-1}. [18-19] The relative intensity of the G versus the D band is frequently reported in the literature as indicative of the density of defects. It is considered higher as the intensity of the G band decreases compared with the intensity of the D band (I_G/I_D). In the present case, the I_G/I_D is about 1.1, a typical value for defective graphenes from polysaccharides. [19-20] Interestingly, the presence of dopant elements does not introduce any signature in Raman spectroscopy.

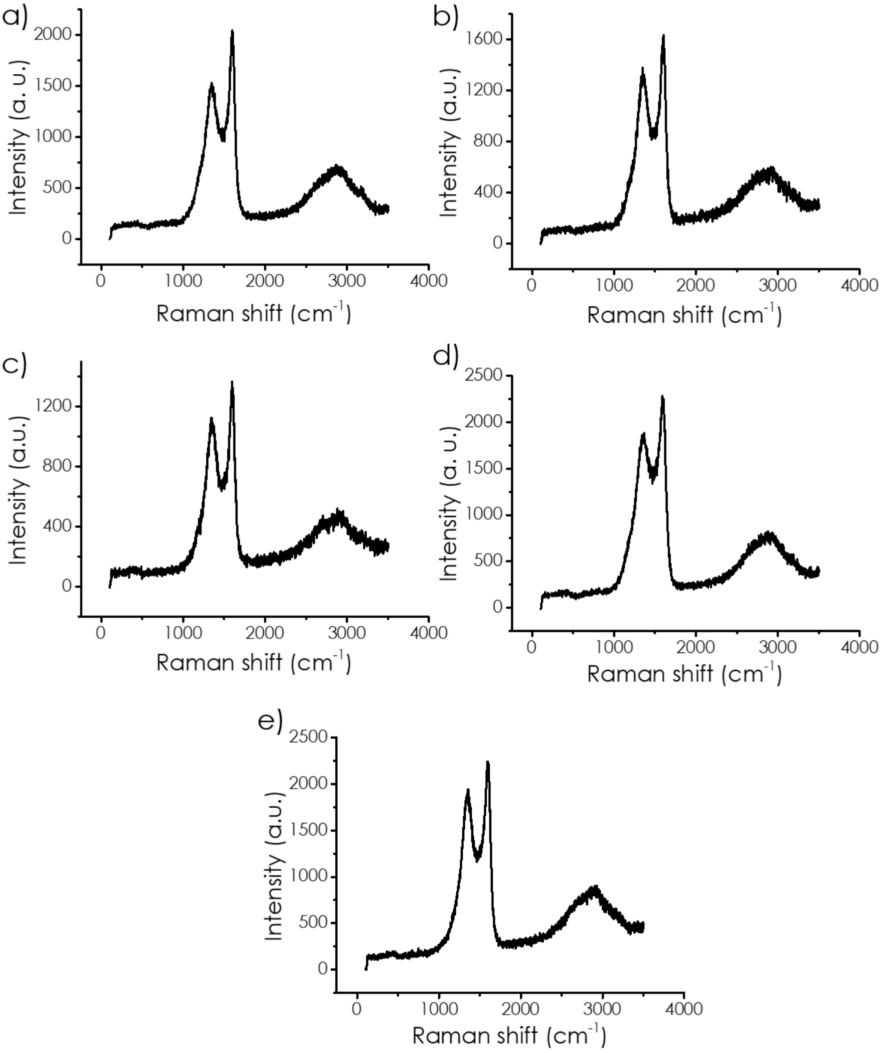

Figure 5.2. Raman spectra of a) mp-C_α, b) mp-C_β, c) mp-C_γ, d) mp-(N)C_α, and e) mp-(P)C_α.

XRD patterns are usually recorded to determine the crystallinity and structure of the materials. Also, in the present case in Figure 5.3, the XRD patterns of the five samples under study are similar. They consist of 3 broad peaks at about 26 °, 45 °, and 61 °, characteristic of graphitic materials of low crystallinity that would correspond to the diffraction along the 002, 004, and 110 planes of graphite. In our materials, these three peaks present in the graphitic carbon materials are accompanied by a sharper diffraction peak at low angles. [13] The absence of this band in graphite has been proposed to be due to the presence of channels in the graphitic carbons, and the narrow shape would be indicative of a narrow pore-size distribution. This is in accordance with the shape and morphology of cyclodextrin precursor, a hollowed molecule which, upon aggregation, would define channels of strictly regular dimension.

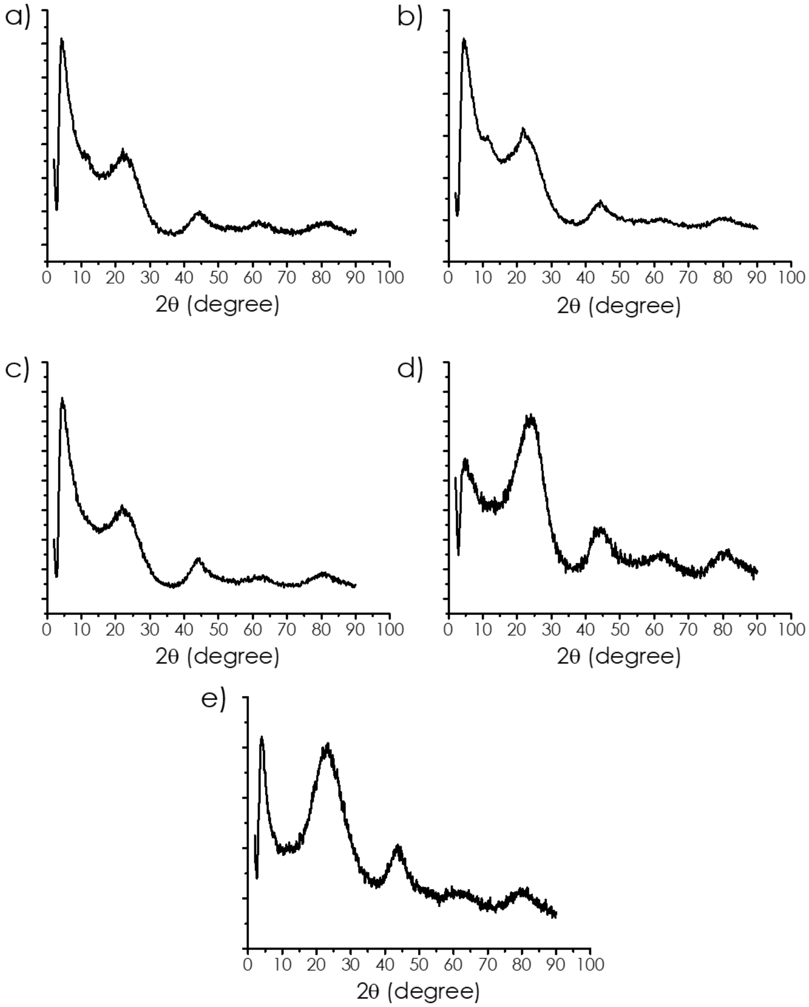

Figure 5.3. XRD spectra of the samples a) mp-C_α, b) mp-C_β, c) mp-C_γ, d) mp-(N)C_α, and e) mp-(P)C_α.

During the pyrolysis and due to the melting of the cyclodextrins at about 300 °C, lower than necessary for the chemical transformation into graphite, the powder sample forms a thick crust on the crucible. FESEM images of this crust show that it is constituted by grains agglomerated as tubes longer than 1 micron and a width of about 80 nm. It is proposed that this alignment reflects the stacking of the truncated cones of cyclodextrin one on top of the other, defining a preferential alignment of the tubes. Figure 5.4 shows selected FESEM images of the samples under study. Upon dispersion of the carbon residue, TEM images of the photocatalysts could be recorded. A selection of them is presented in the same figure. These images reveal that the samples are constituted by particles of about 20 nm, which contain channels. By the difference between the clear and dark contrast of the pore and walls, the micropore dimension could be estimated as 0.66, 0.86, and 0.97 nm for mp-C_{α}, mp-C_{β}, and mp-C_{γ}, respectively. These pore dimension values are compatible with those previously reported by our group for the micropores of mp-C_{α}, mp-C_{β}, and mp-C_{γ}. They are also in good accordance with the diameter of the corresponding cyclodextrin used as the precursor.

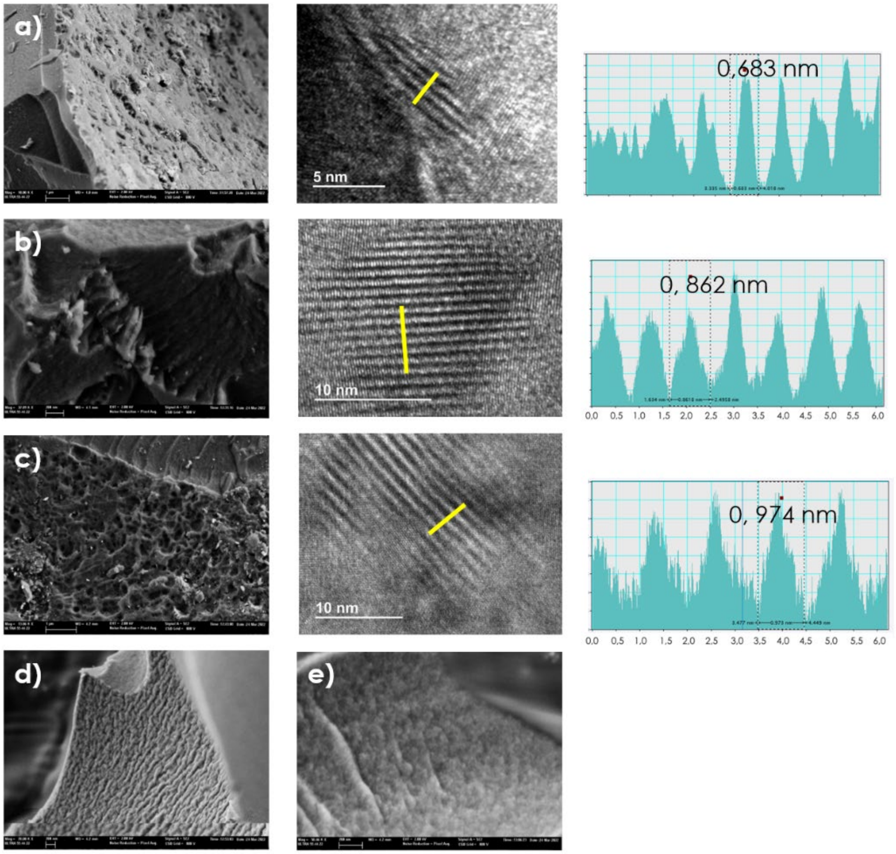

Figure 5.4. Electron microscopy images (TEM and FESEM) of the samples a) mp-C$_{\alpha}$, b) mp-C$_{\beta}$, c) mp-C$_{\gamma}$, d) mp-(N)C$_{\alpha}$, and e) mp-(P)C$_{\alpha}$.

Regarding the photocatalytic activity, the target of the present chapter, light adsorption by the material is a property of significant importance. This information corresponds to the optical absorption spectra of the materials. In the case of solid samples, light adsorption can be obtained by the diffuse reflectance mode, in which upon illumination of a surface with white light, the reflected spectral radiation is analyzed. In the present case, the microporous graphitic carbon inhibits continuous adsorption with growing intensity from the near-infrared toward the UV. Some weak relative adsorption maxima were recorded at about 600, 550, 400, and 280 nm, coincidentally for all the samples. These relative adsorption maxima can be ascribed to the presence in the materials of different domains corresponding to polycyclic condensed aromatics active as isolated chromophores in certain regions. The influence of N and P doping on light adsorption mainly affects in the UV region with the appearance of more intense adsorption bands extending to 350 and 300 nm for (N)C_α and (P)C_α, respectively. The influence of doping in the visible region was not very notable.

Figure 5.5 presents the diffuse reflectance UV-Vis spectra of the samples. From these spectra, it is possible to estimate the band gap of the materials by plotting the Tauc function and considering the samples as indirect semiconductors. Table 5.1 list the optical bandgap resulting from these Tauc plots. It should be commented that the absence of well-defined adsorption bands determines a considerable degree of uncertainty in the estimation of the band gap. This absence is due to the graphitic carbons' inhomogeneous structure with numerous defects populating the intraband gap.

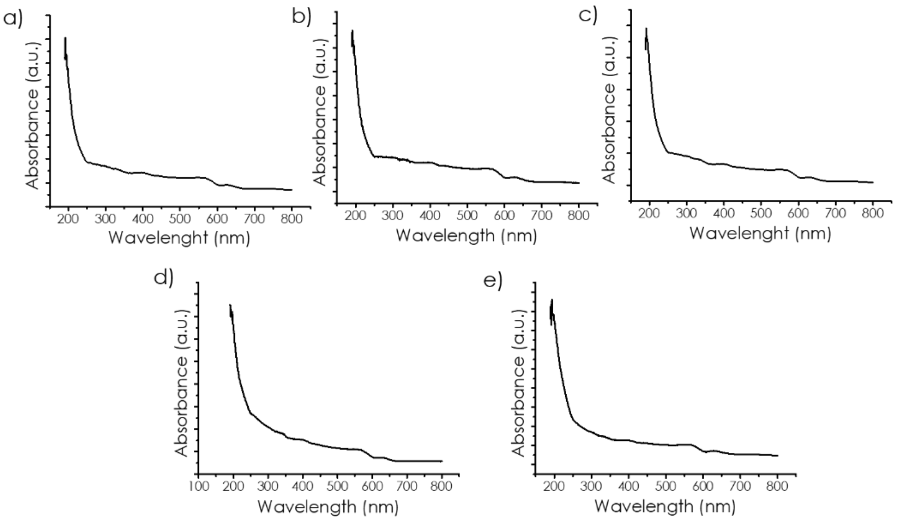

Figure 5.5. UV-Vis spectra of all the studied samples: a) mp-C_α, b) mp-C_β, c) mp-C_γ, d) mp-(N)C_α, e) mp-(P)C_α.

5.2.1 Photocatalytic activity

Photocatalytic CO_2 reduction experiments were carried out upon irradiation with a 300 W Xe lamp that provides the radiation from the UV starting at 300 nm to the near IR region. The experiments were carried out by suspending the photocatalyst in a 3:1 mixture of acetonitrile:water. Here, 4 mL of triethanolamine (TEOA) were added as the sacrificial electron donor. The presence of water is necessary to ensure a high concentration of protons required for CO_2 reduction. Acetonitrile, on the other hand, provides a high concentration of CO_2 that is highly soluble in this solvent. The reaction was carried out at room temperature.

The nature of the products in the gas phase and their evolution align with the irradiation time was determined by injecting aliquots periodically from the photoreactor's headspace in a microGC apparatus coupled with two columns that allow analyzing CO_2, CO, H_2, O_2, CH_4, and light hydrocarbons. Chapter 7 provides additional details of the photoreactor, set-up and analysis, and experimental conditions of these photocatalytic experiments.

The only products observed in the gas phase were H_2 and CO in roughly similar amounts, accompanied by a much lower concentration of CH_4. Analysis of the liquid phase by liquid ^1H and ^{13}C NMR spectroscopy did not allow the detection of any reaction product dissolved in the liquid phase. Figure 5.6 presents the temporal profiles of the 3 products observed in the gas phase depending on the sample used as the photocatalyst.

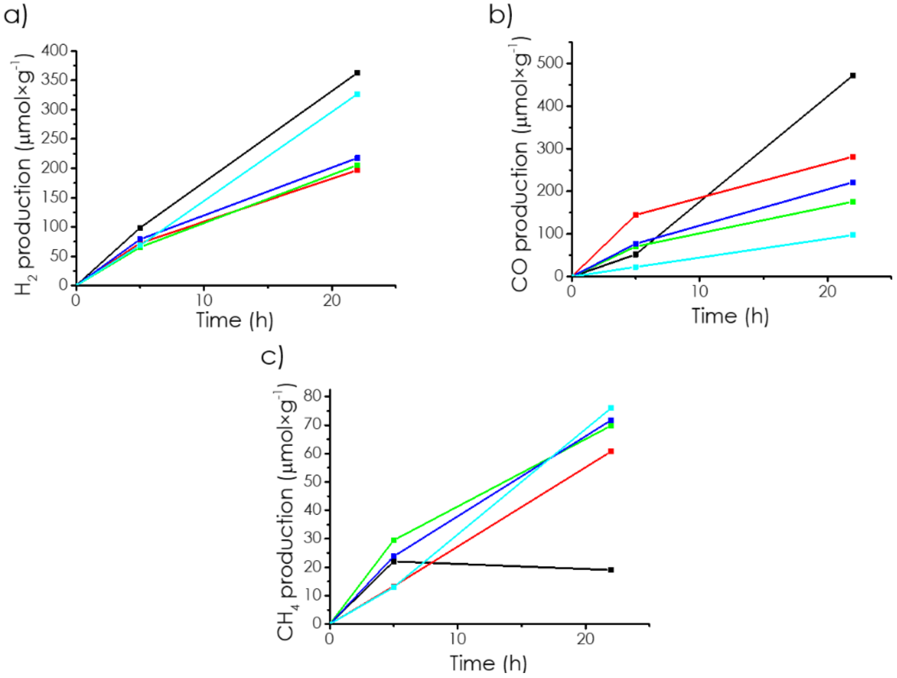

Figure 5.6. Comparative of the temporal evolution of a) H_2, b) CO and c) CH_4 of mp-C_α (black), mp-C_β (red), C_γ (green), mp-(N)C_α and mp-(P)C_α.

Control experiments by measuring the gas evolved from a suspension of mp-C_α in dark conditions, with light and absence of TEOA, or with light and TEOA but no photocatalyst showed a negligible formation of any products as can be seen in Figure 5.7. These control experiments, therefore, indicate the need for photons, photocatalyst CO_2 and TEOA in the product formation.

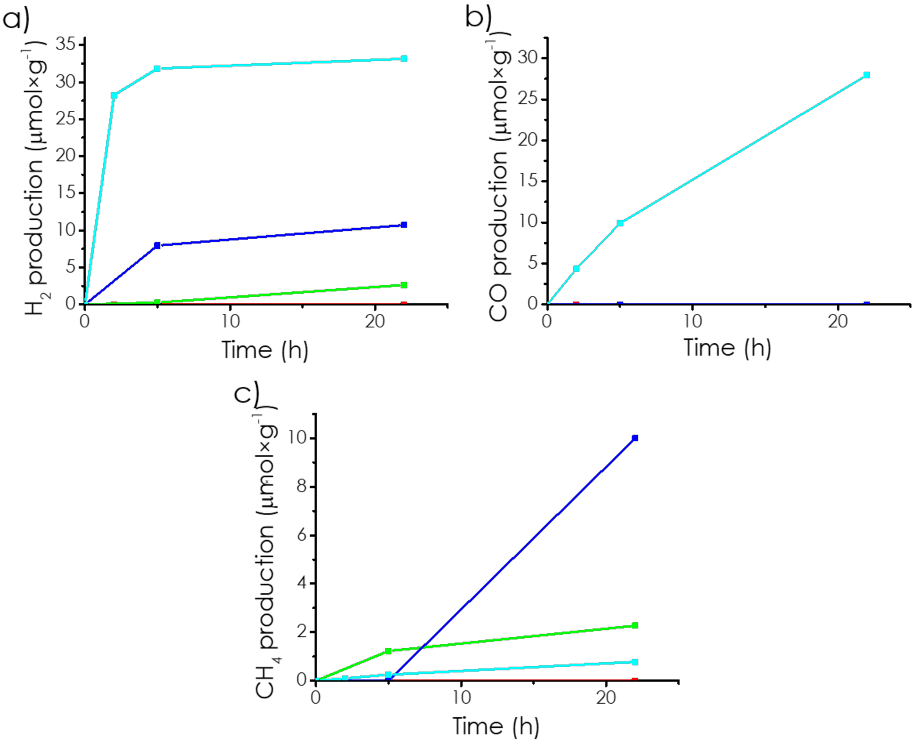

Figure 5.7. Gas production in the blank reactions a) H_2, b) CO and c) CH_4. In the absence of light (red), photocatalyst (green), CO_2 (blue) and TEOA (cyan).

As shown in Figure 5.6, in which the profiles of product evolution have been presented for each of the prepared materials in the present chapter, the photocatalytic activity, measured by the amount of H_2+CO evolved in the process, follows the order $C_\gamma \approx C_\beta < C_\alpha$. This order has also been observed in previous studies for HER [21] and in the previous chapter regarding the influence of doping and pore size on H_2 evolution. [14] The same justification previously proposed to rationalize the photocatalytic activity order can also be applied here to explain the relative activity. Accordingly, the relative activity of the materials would indicate the operation of a spatial confinement effect in which the tight fit of CO_2 with the pore walls of the photocatalyst should favor the electron transfer from the photocatalyst in the charge-separated state with CO_2. As the dimension of the pores increases, the transfer of electrons between the walls and the substrate would be disfavored and, therefore, the photocatalytic activity would decrease. Beyond a certain pore diameter, no influence because of the pore size would be observed. In support of this explanation, it has to be reminded that CO_2 can access C_α micropores while N_2, having a kinetic diameter slightly larger (3.3 Å for the first one and 3.64 Å for the N_2) [22] does not access the internal pores as experimentally determined in the isothermal gas adsorption measurements.

Regarding the influence of doping that was the subject of the previous chapter, in the case of the photocatalytic CO_2 reduction, it was observed in Figure 5.6 that the amount of CO in C_α is higher than that achieved for mp-(N)C_α and mp-(P)C_α. Therefore, in the present case doping has an adverse effect. To understand this, it is proposed that, since TEOA is present as the electron donor and the reaction is performed with UV and visible irradiation, no influence of the band gap should be expected. All the materials meet the thermodynamic requirements of having the conduction band edge potential, being higher than that of the required in the CO_2/CO reduction value (-0.106 V vs NHE). [23] Figure 5.8 presents the energy values of the valence and conduction band for each of the 5 materials under study. The figure includes the thermodynamic reduction potential of the CO_2/CO pair as a reference.

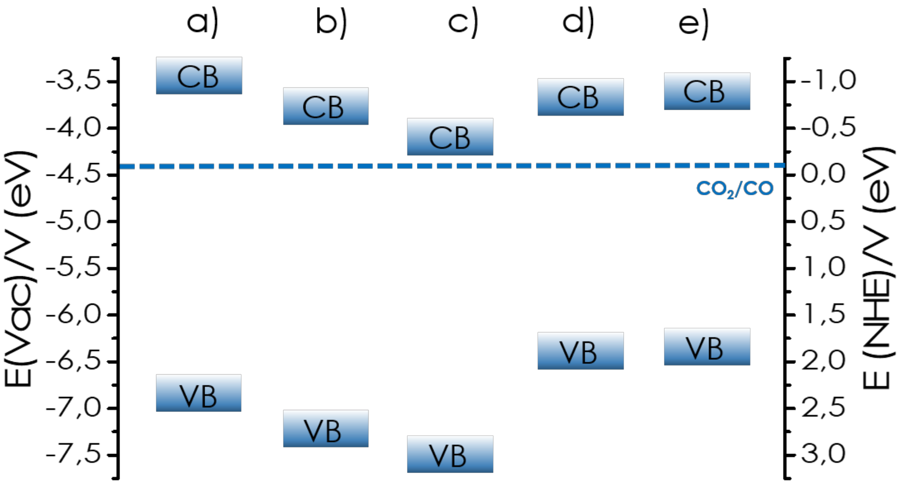

Figure 5.8. Positioning of the valence band (VB) and conduction band (CB) of a) mp-C$_\alpha$, b) mp-C$_\beta$, c) mp-C$_\gamma$, d) mp-(N)C$_\alpha$, and e) mp-(P)C$_\alpha$.

The results shown in Figure 5.6 are notabe considering that the photocatalyst C$_\alpha$, the most active, is constituted by C in 98 % and does not contain any metal. As commented in previous chapters, metal nanoparticles can decrease the photocatalytic activity of materials by increasing the efficiency of charge separation and also by catalyzing dark reactions involved in gas evolution. It is notable also that doping does not increase the catalytic efficiency. In this regard, it seems that the main factor controlling activity in the present case is the confinement effect. Regarding doping, it also needs to be commented that the amount of dopant elements is crucial to achieving optimal photocatalytic activity since lower or higher amounts typically disfavor the photocatalytic process. A quantitative indicator of the efficiency of a photocatalyst is the apparent quantum yield, obtained by determining the number of photons that form a given amount of product and taking into account the stoichiometry of the process. In the case of mp-C$_\alpha$, the apparent quantum yield measured with monochromatic light of 380 nm was estimated to be 0.03%.

The stability of the material under reaction conditions was studied for mp-C$_\alpha$, the most active material, by performing a series of 4 consecutive uses of the same sample. The results are presented in Figure 5.9, showing no decrease in the initial reaction rate or the final amount of photoproducts, the temporal profiles for each photoproduct being unchanged upon reuse. Additional information about photocatalyst stability was obtained by TEM images of the four-times-used material and showed no changes in the morphology or average particle dimension of the C_α after use. The particles of the used materials also exhibit the characteristic uniform channels with the same pore diameter (0.67 nm) as that of the fresh sample, thus confirming structural stability.

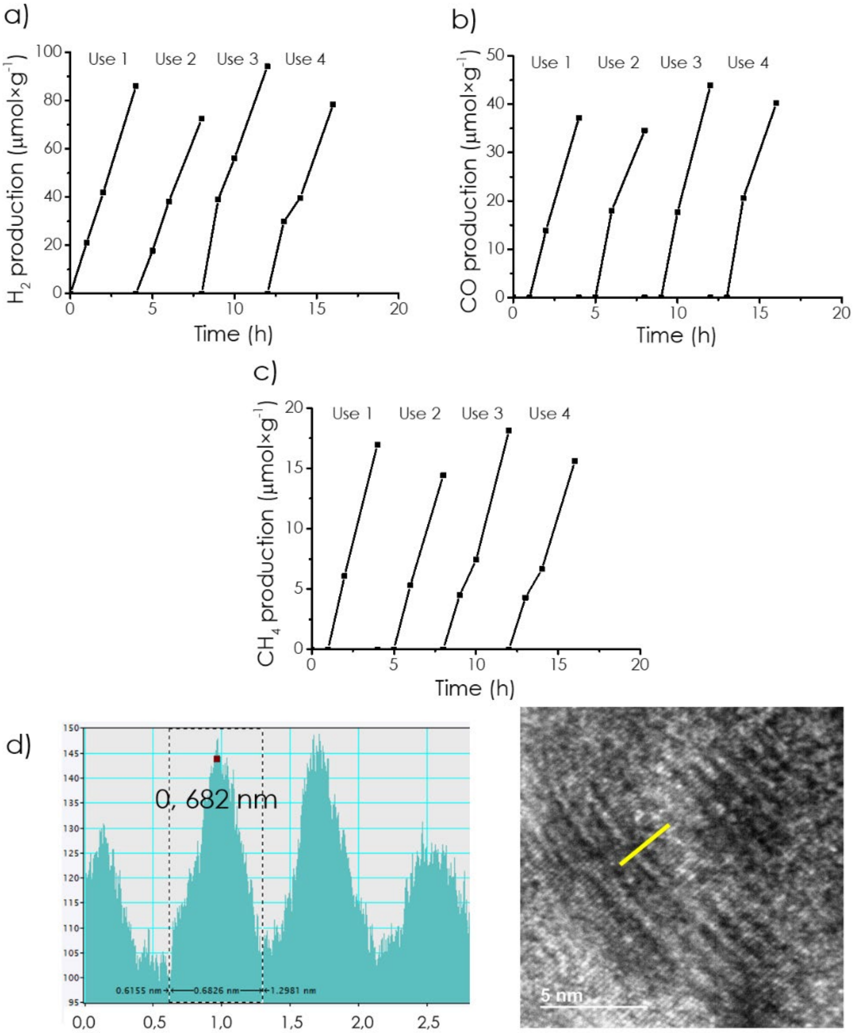

Figure 5.9. Gas evolution for 4 consecutive uses of the mp-C_α: a) H_2, b) CO, c) CH_4, and d) HRTEM images after the uses.

Besides irradiation with Xe lamp, photocatalytic CO_2 reduction by C_α photocatalyst was also performed using simulated sunlight. The results are presented in Figure 5.10. As can be seen there, CO and H_2 evolution diminishes significantly using a solar simulator as the light source. This evolution indicates that a substantial proportion of the mp-C_α photoresponse derives from the UV light in the range from 300 to 380 nm.

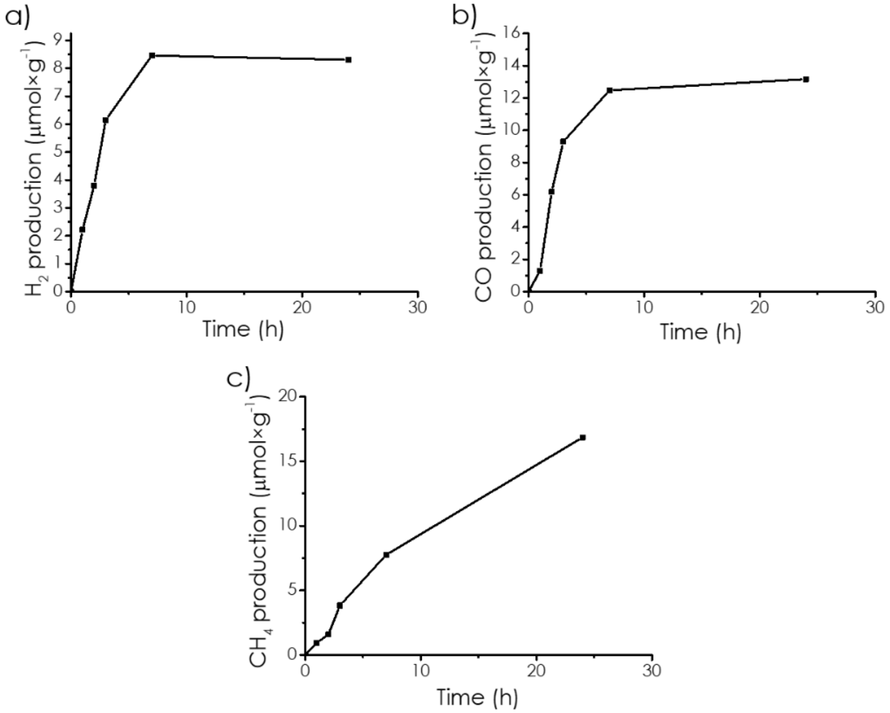

Figure 5.10. Gas production of the sample mp-C_α with simulated solar light irradiation a) H_2, b) CO and c) CH_4.

An effect of the different spectral distributions of the radiation was a change in the product distribution. In the case of solar light irradiation, methane was the major product (17 µmol × g^{-1}), with H_2 (8.5 µmol × g^{-1}) and CO (13 µmol × h^{-1}) being formed in much lesser amounts. Since in the photocatalytic CO_2 reduction CO is a primary intermediate that can be desorbed or can undergo further reduction down to CH_4, the change in product distribution as a function of the irradiation wavelength could indicate that CO is formed in those sites on mp-C_α adsorbing deep in the UV and having low CO adsorption affinity. In contrast, methane will be formed, in lesser amounts, in those sites having stringer CO adsorption and being activated at longer wavelengths. Accordingly, under solar light irradiation, these will be the only sites responsible for the photocatalytic activity, while under Xe lamp irradiation, all the sites, including the most active adsorbing in the deep UV, will be operative.

The origin of CO and CH_4 was demonstrated by the previously commented control experiments, in which CO_2 was absent and acetonitrile/water/TEOA solution was purged by Ar, whereby no CO and CH_4 were observed except in the cases of mp-(N)C_α and mp-(P)C_α. As previously commented in the control experiments, a small production of CO and CH_4 was observed for these doped microporous carbons. Additional firm confirmation of CO_2 as the source of CO and CH_4 was obtained using C^{13} labeled CO_2 and analyzing the products by mass spectroscopy. The mass spectrum of this isotopic of these experiments is presented in Figure 5.11. It is observed there that the peak corresponding to CO appears at m/z 29 mau (mass atomic unit) corresponding to ^{13}CO. No peak at m/z 28 mau was recorded. Thus confirming the absence of ^{12}CO. These isotopic labeling experiments strongly confirm that CO is derived from CO_2.

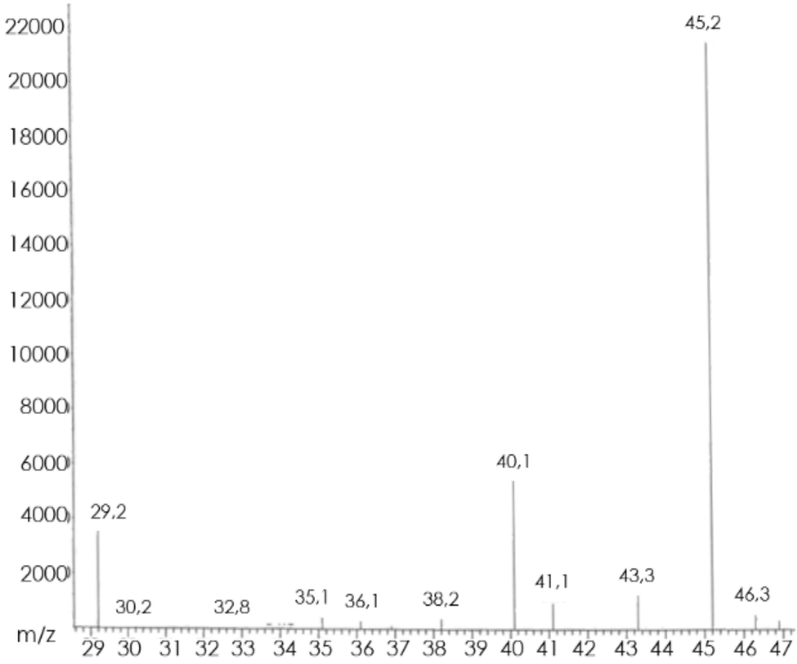

Figure 5.11. Mass spectra from the test using $^{13}CO_2$ as the substrate and mp-C_α as photocatalyst.

The possibility that mp-C_α can also promote artificial photosynthesis in which water is the source of electrons and protons was also studied by performing analogous experiments in the absence of TEOA as the sacrificial electron donor. All other conditions of the photocatalytic experiments were maintained except that the volume of TEOA was replaced by the same volume of H_2O. The results are presented in Figure 5.7. As can be seen there, under these conditions, H_2 was the major photoproduct (32 µmol× g^{-1}), accompanied by a smaller percentage of CO (27 µmol× g^{-1}). The formation of methane barely could be detected under these conditions. These results are in line with those presented in the previous chapter, in which the absence of a sacrificial electron donor decreases considerably the evolution of the photoreduction products. The observation of oxygen confirms that H_2O is acting as an electron source. It is remarkable that in the absence of any metal, a material constituted almost exclusively by carbon with minor percentages of hydrogen and oxygen can perform photocatalytic CO_2

reduction, although it is clear that the efficiency has still to be improved considerably.

5.2.2 Photocurrent measurements

As in the previous chapter, photocurrent measurements were carried out for the undoped mp-C$_\alpha$ sample to a certain occurrence of charge separation or the generation of electron-holes under irradiation with a Xe lamp. Electrodes were prepared by depositing the ink containing mp-C$_\alpha$ onto a transparent FTO electrode. The electrode containing mp-C$_\alpha$ behaves as a working electrode, while graphite and Ag/AgCl were the counter and reference electrodes, respectively. Photocurrent measurements were carried out in a single-compartment electrochemical cell using 1 M aqueous $KHCO_3$ as electrolyte. The cell was purged with N_2 before the measurements. Chapter 10 contains further experimental details on electrode experimental preparation, power meter, type of lamp, and other set-up and operation conditions. The results of the photocurrent measurements are presented in Figure 5.12.

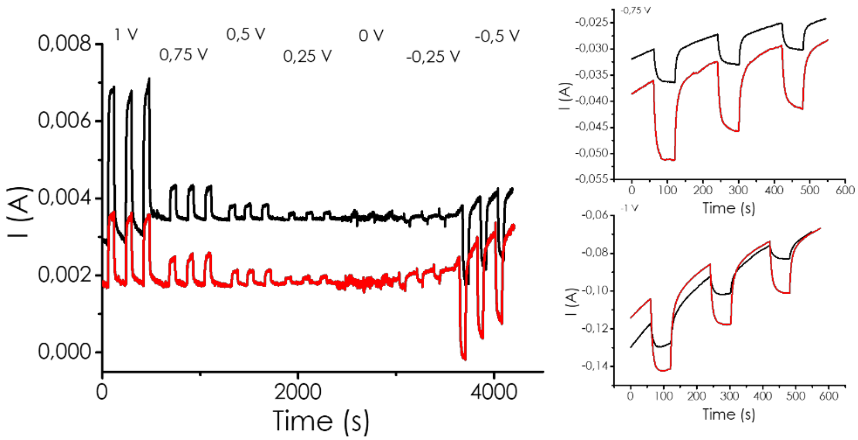

Figure 5.12. Photocurrent measurements with N2 atmosphere (black) and Co2 atmosphere (red). On the right there is an expansion of the -0.75 V and -1 V.

Preliminary measurements of the polarization corps determine that mp-C$_\alpha$ electrodes can be studied in the range of potential from 1 to - 0.5 V vs Ag/AgCl electrode. At more negative potential, strong currents due to the discharge of the electrode with the formation of H_2 take place. Thus, making electrochemical measurements stable due to the evolution of those bubbles.

Measurements were carried out under N_2 and CO_2 atmosphere, providing evidence of the influence of the presence of CO_2. Measurements were carried out by alternative one mini period of light on and light off of 1 min each to determine dark current. Photocurrent measurements were carried out in 3 polarization voltages, working at 1 V vs Ag/AgCl large photocurrents were measured, with no difference between the measurements under N_2 or CO_2. It is proposed that under these conditions, all the charge carriers generated in the photochemical process are mobilized and extracted by the polarization of the electrode. In comparison, much lower currents were measured at polarization 0.5 or 0.25 V vs Ag/AgCl, meaning that not all the maximum charge carrier density possible in the electrode has not been reached. Under these conditions, larger photocurrent values were measured when the atmosphere is CO_2 compared to N_2. These indicate the beneficial effect of the presence of CO_2 as well as the participation of CO_2 in the photocurrent intensity. At 0 V vs Ag/AgCl of bias potential, no charge extraction could be observed and a change of the sense of the current form positive to negative was observed beyond -0.25 V vs Ag/AgCl. This potential should be close to the conduction band edge energy for mp-C_α. Beyond this crossover of the current sense from positive to negative, the current was negative and had always higher intensity in the presence of CO_2 as compared to the N_2. Figure 5.12 provides adequate expansions to visualize how CO_2 affects the photocurrent intensity in comparison to N_2.

In summary, the photocurrent study is compatible with the concurrence of charge separation in the mp-C_α electrode under illumination and the current direction confirms mp-C_α as an n-type semiconductor. The comparison of the response in the presence of CO_2 or N_2 clearly shows that CO_2 is interacting with the photocatalyst contributing to a higher current intensity in comparison to N_2 as an inert gas.

5.2.3 Transient adsorption spectroscopy study

Transient absorption spectroscopy is one of the most powerful photophysical characterization techniques since it allows the detection of photogenerated electronic excited stages and another type of transients, determining the lifetime and the interaction with quenchers. In transient adsorption spectroscopy, a short laser pulse is used to excite the sample, generating a micromolar concentration of photogenerated species monitored by transmission or diffuse reflectance optical spectroscopy. In the present case, a nanosecond Nd:YAG laser operating with the third harmonic (355 nm) with a pulse of 7 ns FWHM (Full width at half maximum) was used to excite microporous graphitic carbons suspended in acetonitrile. In all cases, the generation of a transient signal decaying in the microsecond time scale was observed. Figure 5.13 presents some transient signal decays to illustrate the intensity and the temporal window of the transients. In all cases, the transient spectra consist of continuous adsorption spanning the whole spectral window available to our monochromator (280-760 nm).

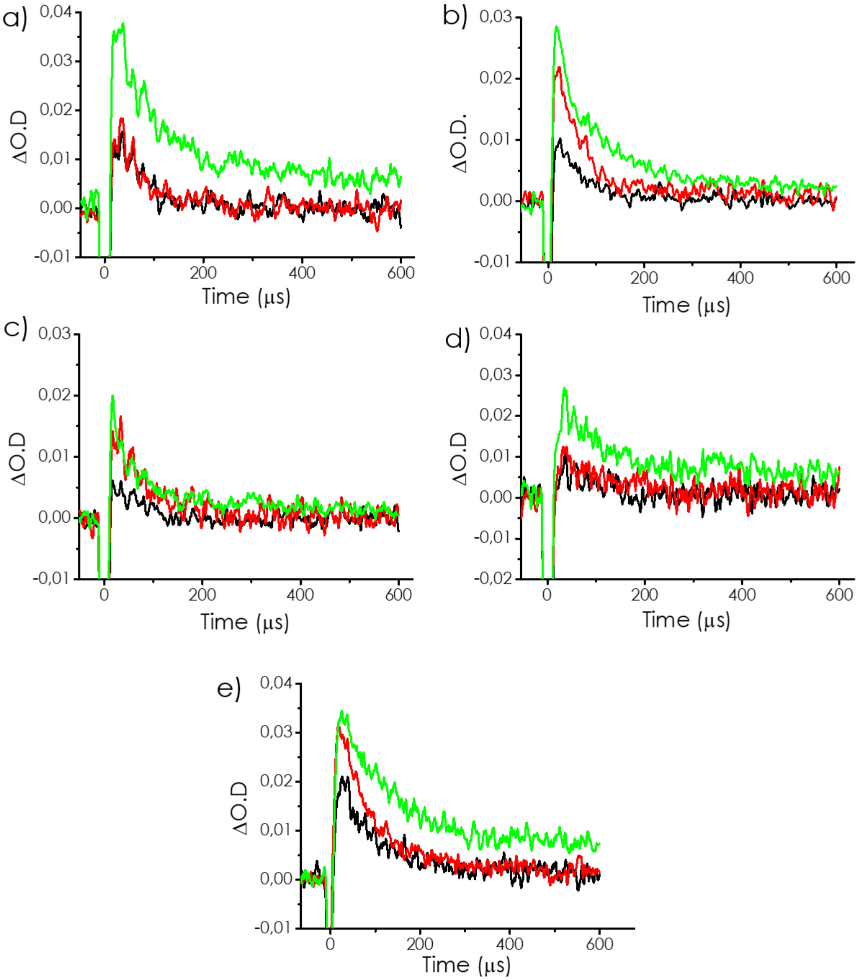

Figure 5.13. Transient signal decay was monitored at 400 nm for a) mp-C_α, b) mp-C_β, c) mp-C_γ, d) mp-(N)C_α and e) mp-(P)C_α in absence of any quencher (black), with O_2 (red) and CO_2 as quenching electrons (green).

This continuous adsorption is reminiscent of the optical light adsorption recorded for the ground stages of the material. Analysis of the temporal profiles at different wavelengths shows coincident plots, indicating that they correspond to a single transient species or that if there are two or more they decay by recombination and mutual annihilation. These temporal profiles could be fitted to a monoexponential decay with a lifetime of 60 µs. The transient spectra of all the samples were very similar. Figure 5.14 presents a series of transient spectra for the samples recorded at different decay time after the laser pulse. No substantial differences as a function of the pore size or doping were observed except that the signal for mp-C$_{\alpha}$ was more intense at initial times after the laser pulse. This higher intensity could be related to a more efficient generation of transient states or a higher absorptivity of the photogenerated transients.

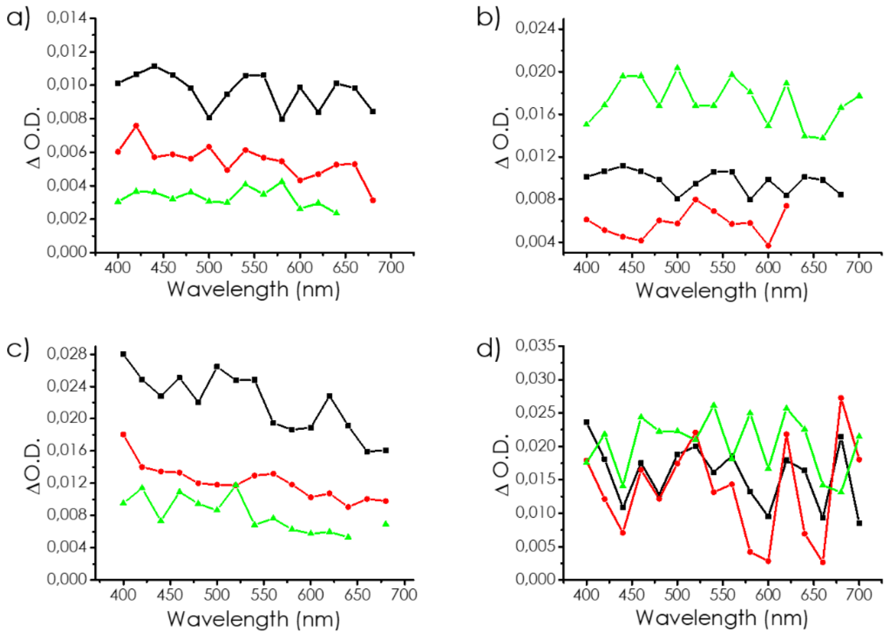

Figure 5.14. Spectra recorded at 50 µs of the samples mp-C$_{\alpha}$ (black), mp-C$_{\beta}$ (red) and mp-C$_{\gamma}$ (green) in a) N_2 and c) CO_2; and the samples mp-C$_{\alpha}$ (black), mp-(N)C$_{\alpha}$ (red) and mp-(P)C$_{\alpha}$ (green) in b) N_2 and d) CO_2.

Information on the nature of the photogenerated transient states can be indirectly obtained by quenching studies. In these quenching studies, the influence of certain substances at different concentrations on the temporal profile of the transient signal is monitored, and the changes rationalized as derived from the interaction of the quencher with the photogenerated states. In the present case, it is presumed that light irradiation would result in the formation of a charge separation state with the appearance of electrons in the conduction band and valence band electron holes. To support this claim initial quenching experiments were carried out comparing the temporal profile of the signal under an inert atmosphere and in the presence of O_2. In the case of mp-C_α minor changes caused by the presence of oxygen were observed. In comparison, mp-C_β exhibited more evident changes in the transient signal due to the presence of O_2. Specifically, the transient signal in the short wavelength region from 400-480 nm increase in intensity, while signals at longer wavelength such as 640 nm are almost unaltered. This behavior has been previously seen in the literature and interpreted considering that the transient signal is a contribution of the adsorption of electrons and holes. If in the present case light adsorption due to holes contributes in a larger proportion in the short wavelength range, then the presence of O_2 should increase the signal intensity by quenching photogenerated electrons. Since O_2 traps efficiently conduction band electrons (this is the reason why photocatalytic experiments should be carried out in absence of O_2 and air), then, the presence of oxygen would decrease prompting the electron/holes recombination and, consequently, an increase in the population of holes should occur. It is proposed that this excess of holes is responsible for the increase of the intensity in the 400-480 nm. The fact that this effect is not so remarkable in the case of mp-C_α would be a reflection that oxygen has diffusion limitations in this material due to its small pore size. As already commented, N_2 does not diffuse to the internal pore of mp-C_α and the kinetic diameter of N_2 and O_2 is very similar.

To provide some support to the previous interpretation of the influence of O_2 on the transient signal, similar quenching experiments were carried out using CO_2. As commented earlier, CO_2 can diffuse inside the mp-C_α micropores. In agreement with our proposal, a similar behavior of the transient signal of CO_2 or O_2 was observed. I. e. an increase of the signal intensity in the range of short wavelength accompanied by an increase in the signal decay and no changes at a long wavelength in the transient spectra. The changes in the intensity at temporal evolution in the short wavelength range would indicate that the reaction of CO_2 with conduction band electrons leaves higher population of holes. The lack of response at long wavelength would indicate that this region should correspond to electron and electron/holes trapped in the material but unable to react to either O_2 or CO_2. Figure 5.15 presents a summary of these quenching measurements by CO_2. It I worth mentioning that the influence of CO_2 is even larger than that of O_2, an unexpected result, due to the more negative reduction potential of the CO_2 concerning to O_2, but that can be interpreted assuming the previously commented diffusion limitations. Accordingly, even though CO_2 should react with a fraction of electrons that have more negative potentials, this molecule would be able to access the interior of the mp-C_α particles. On the contrary, even though O_2 is easier to be reduced, this gas molecule will not have access to the pores.

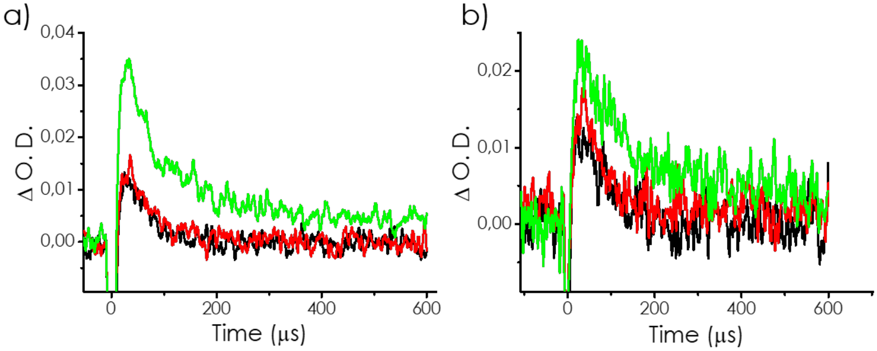

Figure 5.15. Deactivation kinetics were monitored using N_2 (black), O_2 (red), and CO_2 (green) at a) 500 nm and b) 600 nm.

The influence of dopant elements on the transient adsorption spectrum deserves some specific comments. In the case of mp-(N)C_α the transient signal was notably smaller. This can be interpreted considering that for the sample under study the presence of nitrogen favors fast e^-/h^+ recombination and the population of this charge-separated state reaching the microsecond time scale would be lower. It is well known in the literature that the presence of excessive amounts of dopant elements disfavors photocatalytic reactions since at these high concentrations dopant elements are predominantly acting as charge recombination centers. It is proposed that this is the case for the mp-(N)C_α sample under study, In the case of mp-(P)C_α stronger signals were observed after the laser pulse. However, no quenching of these signals was detected either in the presence of O_2 or CO_2 that perform it seems that electrons in the case of mp-(P)C_α do no react with O_2 or CO_2. In the first case, O_2 should not diffuse in the particles and, in the case of CO_2; the reduction potential of electrons may not be enough to be transferred to the CO_2.

Overall the results of the transient adsorption measurements serve to rationalize the photocatalytic experiments, particularly the absence of a positive influence of dopants elements. However, the reasons why the presence of N or P does not increase the photocatalytic activity would be different. In the case of N, this element would act in the mp-(N)C_α sample as recombination centers. In the case of mp-(P)C_α, the reduction potential of excited state electrons would be insufficient to reduce CO_2 and thus, the transient signal results unchanged in the presence or absence of these molecules.

5.3 Conclusions

The present chapter has shown that microporous graphitic carbons can promote photocatalytic CO_2 reduction to CO in the presence of a sacrificial electron donor with a response in the visible region. The process is accompanied by the simultaneous generation of H_2. The origin of CO from CO_2 was confirmed by ^{13}C isotopic labeling experiments. In line with previous studies including Chapter 3, the most efficient material was the one having a small pore size obtained by pyrolysis of α-cyclodextrin. Photocurrent measurements confirmed the photogeneration of electrons and holes that upon illumination the electrode can generate a current that depends on the applied bias potential. Transient adsorption spectroscopy has been used to rationalize why in the present case, no positive influence of the N or P doping is observed. In the case of N doping heteroatoms, the lifetime of the excited states decreases, apparently acting as charge recombination centers. In the case of P doping, interaction with CO_2 as a quencher was not detected and the transient signal of the photogenerated carriers appeared unaffected by the presence of this compound. Overall, the present data illustrate the remarkable potential of microporous graphitic carbons constituted almost exclusively by carbon atoms for the use as photocatalyst for solar fuel production.

5.4 References

1. Hashimoto, K.; Irie, H.; Fujishima, A., TiO2 as Photocatalysis: A Historical Overview and Future Prospects. *Japanese Journal of Applied Physics* **2005,** *44* (12), 8269-8285.

2. Bard, A. J., Photoelectrochemistry and heterogeneous photo-catalysis at semiconductors. *Journal of Photochemistry* **1979,** *10* (1), 59-75.

3. Navalon, S.; Dhakshinamoorthy, A.; Alvaro, M.; Antonietti, M.; García, H., Active sites on graphene-based materials as metal-free catalysts. *Chemical Society Reviews* **2017,** *46* (15), 4501-4529.

4. Navalon, S.; Dhakshinamoorthy, A.; Alvaro, M.; Garcia, H., Carbocatalysis by Graphene-Based Materials. *Chemical Reviews* **2014,** *114* (12), 6179-6212.

5. Su , D. S.; Zhang, J.; Frank, B.; Thomas, A.; Wang, X.; Paraknowitsch, J.; Schlögl, R., Metal-Free Heterogeneous Catalysis for Sustainable Chemistry. *ChemSusChem* **2010,** *3* (2), 169-180.

6. Li, C.; Xu, Y.; Tu, W.; Chen, G.; Xu, R., Metal-free photocatalysts for various applications in energy conversion and environmental purification. *Green Chemistry* **2017,** *19* (4), 882-899.

7. Shen, H.; Peppel, T.; Stunk, J.; Sun, Z., Photocatalytic Reduction of CO2 by Metal-Free Based Materials: Recent Advances and Future Perspective. *Solar RRL* **2020,** *4*.

8. Wang, X.; Blechert, S.; Antonietti, M., Polymeric Graphitic Carbon Nitride for Heterogeneous Photocatalysis. *ACS Catalysis* **2012,** *2* (8), 1596-1606.

9. Wang, X.; Maeda, K.; Thomas, A.; Takanabe, K.; Xin, G.; Carlsson, J. M.; Domen, K.; Antonietti, M., A metal-free polymeric photocatalyst for hydrogen production from water under visible light. *Nature materials* **2009,** *8* (1), 76-80.

10. Albero, J.; Mateo, D.; García, H., Graphene-Based Materials as Efficient Photocatalysts for Water Splitting. *Molecules* **2019,** *24* (5).

11. Mateo, D.; Esteve-Adell, I.; Albero, J.; Royo, J. F. S.; Primo, A.; Garcia, H., 111 oriented gold nanoplatelets on multilayer graphene as visible light photocatalyst for overall water splitting. *Nature Communications* **2016,** *7* (1), 11819.

12. Albero, J.; Peng, Y.; García, H., Photocatalytic CO2 Reduction to C2+ Products. *ACS Catalysis* **2020,** *10* (10), 5734-5749.

13. Rendón-Patiño, A.; Santiago Portillo, A.; Vallés-García, C.; Palomino, M.; Navalon, S.; Franconetti, A.; Primo, A.; Garcia, H., Templateless Synthesis

of Ultra-Microporous 3D Graphitic Carbon from Cyclodextrins and Their Use as Selective Catalyst for Oxygen Activation. *Small Methods* **2020,** *4*.

14. García-Mulero, A.; Rendón-Patiño, A.; Asiri, A. M.; Primo, A.; Garcia, H., Band Engineering of Semiconducting Microporous Graphitic Carbons by Phosphorous Doping: Enhancing of Photocatalytic Overall Water Splitting. *ACS Applied Materials & Interfaces* **2021,** *13* (41), 48753-48763.

15. Rendón-Patiño, A.; Torres, F.; Primo, A.; Garcia, H., Band gap alignment of structured microporous graphitic carbons by N doping and its influence on the photocatalytic overall water splitting. *Sustainable Energy & Fuels* **2022**.

16. Rouquerol, F. R., J.; Sing, K.S.W.; Llewellyn, P.; Maurin, G. , *Adsorption by Powders and Porous Solids Principles, Methodology and Applications*. Second ed.; Elsevier: 2014.

17. Primo, A.; Atienzar, P.; Sanchez, E.; Delgado, J. M.; García, H., From biomass wastes to large-area, high-quality, N-doped graphene: catalyst-free carbonization of chitosan coatings on arbitrary substrates. *Chemical Communications* **2012,** *48* (74), 9254-9256.

18. Baldovi, H. G.; Krüger, M.; Reinsch, H.; Alvaro, M.; Stock, N.; Garcia, H., Transient absorption spectroscopy and photochemical reactivity of CAU-8. *Journal of Materials Chemistry C* **2015,** *3* (15), 3607-3613.

19. Esteve-Adell, I.; He, J.; Ramiro, F.; Atienzar, P.; Primo, A.; García, H., Catalyst-free one step synthesis of large area vertically stacked N-doped graphene-boron nitride heterostructures from biomass source. *Nanoscale* **2018,** *10* (9), 4391-4397.

20. Seehra, M. S.; Narang, V.; Geddam, U. K.; Stefaniak, A. B., Correlation between X-ray diffraction and Raman spectra of 16 commercial graphene–based materials and their resulting classification. *Carbon* **2017,** *111*, 380-385.

21. Peng, Y.; Rendón-Patiño, A.; Franconetti, A.; Albero, J.; Primo, A.; García, H., Photocatalytic Overall Water Splitting Activity of Templateless Structured Graphitic Nanoparticles Obtained from Cyclodextrins. *ACS Applied Energy Materials* **2020,** *3* (7), 6623-6632.

22. Scholes, C.; Kentish, S.; Stevens, G., Carbon Dioxide Separation through Polymeric Membrane Systems for Flue Gas Applications. *Recent Patents on Chemical Engineering* **2010,** *1*.

23. Cao, Y.; Chen, Q.; Shen, C.; He, L., Polyoxometalate-Based Catalysts for CO2 Conversion. *Molecules* **2019,** *24*, 2069.

CHAPTER 6.

ELECTROCATALYTIC ACTIVITY OF MICROPOROUS GRAPHITIC CARBONS FOR CO_2 REDUCTION

6.1 Introduction

Having already reported the photocatalytic activity of microporous graphitic carbons from different cyclodextrins for hydrogen evolution and CO_2 reduction, it was of interest to determine their activity as electrocatalyst. Photocatalysis and electrocatalysis share substrates redox reactions and defer in the activation energy, either photons in photocatalysis or electric fields in the case of electrochemistry. [1] Particularly, it is interesting to see the performance of these microporous graphitic carbons for CO_2 reduction. In the literature, there is an ample number of reports showing that doped carbons can be employed as electrocatalysts. [2] For these applications, carbon enjoys a high electrical conductivity together with the presence of active sites, mainly at dopant elements and structural defects. In this regard, using N-doped graphene as an electrocatalyst has been a hot area in electrochemistry. [3-5]

Considering the importance of electrocatalysis in developing new electrochemical processes in which green renewable electricity is used to obtain fuels and chemical compounds, the present chapter describes the results of the CO_2 electrochemical reduction using microporous graphitic carbons derived from α-cyclodextrin pyrolysis. Specifically, the current chapter has selected C_α and $(P)C_\alpha$ as materials to evaluate their electrocatalytic performance. This selection was based on the enhanced activity of mp-C_α compared to analogous graphitic carbons derived from the pyrolysis of other cyclodextrins. In addition, the doping effect will be screened by selecting mp-(P)C_α at the intermediate doping level, which was the most efficient material for photocatalytic water splitting. The purpose is to provide a preliminary screening of the activity of these two carbon materials.

6.2 Results and discussion

The samples under study mp-C_α and mp-(P)C_α correspond to those previously characterized in Chapters 4 and 5. As previously indicated, α-cyclodextrin in the absence and in the presence of phosphoric acid as a precursor of P element was pyrolyzed at 900 °C heating from room temperature at a temperature ramp rate of 10 °C × min^{-1}. Chemical analysis, Raman spectra, XPS data, and TEM images correspond to those previously described in Chapters 4 and 5 too.

These materials were used as electrocatalysts by coating Ti foil with a thin film of the corresponding microporous graphitic carbons using PVDF as a binder and N-methylpyrrolidone (NMP) as a solvent to prepare the ink. The binder and the graphic carbon were previously milled together to obtain a homogeneous mixture. This paste was used to form a thin coating on once-cleaned Ti foil with ethanol. A square 1 x 1 cm surface was covered with the ink and then, this was dried at 60 °C overnight to increase the adherence to the metal surface.

For the measurements, a single-compartment electrochemical cell using the carbon-coated Ti foil, graphite, and saturated Calomelanos electrode (SCE) electrodes were used as working, counter and reference electrodes respectively. The measurements were carried out using an aqueous 0.5 M solution of Na_2SO_4 as electrolyte under inert (He) or CO_2 atmosphere. Electrochemical measurements were carried out after the equilibration of the working electrode with the electrolyte by immersing it into the electrolyte solution for at least 24 h before the measurements. Note that CO_2 atmosphere changes the pH value of the electrolyte from quasi-neutral 6.5 to 4.5 units. Further experimental details are given in Chapter 7.

Electrical conductivity measurements of the electrodes were determined for the coatings under study. The electrical resistance values were obtained from the response of voltage at different applied intensities and applying the Ohm law for the linear region. These values of conductivity were found to vary from one material to another and even for the same electrode upon repeating the measurement. For this reason, at least 12 measurements for each of the two materials were performed. The mean results are given in Table 6.1 with the corresponding standard deviation. As can be seen there, the presence of phosphorous substantially decreases the electrical conductivity of the material.

Table 6.1. Conductivity of the materials under study.

Material	**mp-C$_{\alpha}$**		**mp- (P)C$_{\alpha}$**		**mp-(P)C$_{\alpha Ex}$**	
Thickness (mm)	0,12		0,08		0,1	
Slope (Ω)	491,9		1385		1253,7	
Current (mA)	**Mean**	**Desv**	**Mean**	**Desv**	**Mean**	**Desv**
0,25	0,132	0,035	0,609	0,131	0,755	0,156
0,5	0,258	0,067	1,118	0,227	1,817	0,379
1	0,515	0,124	2,002	0,374	2,220	0,453
1,5	0,760	0,192	2,708	0,483	2,895	0,572
2	0,966	0,218	3,280	0,535	3,424	0,683
2,5	1,166	0,258	3,747	0,585	3,893	0,813
3	1,358	0,303	4,190	0,617	4,236	0,873
4	1,686	0,331	4,849	0,706	4,878	1,034
5	1,928	0,327	5,353	0,758	5,414	1,111
6	2,157	0,316	5,719	0,781	5,831	1,108
7	2,367	0,312	6,021	0,902	5,913	0,801
Conductivity (S × m^{-1})	4,83		1,47		1,66	

Electrodes of mp-C$_{\alpha}$ and mp- (P)C$_{\alpha}$ were screened regarding the cyclic voltammetry response electrolyte. In the case of mp-C$_{\alpha}$, starting at neutral potential and increasing polarization to positive voltages, a pretty flat response with no increase in current was recorded. This behavior is similar to that of metallic conductors, in which voltages variations can be performed practically with 0 current. After reaching 600 mV and going towards negative potentials, an increase of the current density was recorded, the maximum current density value being -180 mA × cm^{-2} × g^{-1}, corresponding to a resistive material in which there should be a linear variation of the intensity with applied polarization. Importantly, the cyclic voltammetry response was very stable after 10 cycles and could be reproduced even after extensive exposure of the electrode to +0.4 V. No much influence of the presence of CO$_2$ was observed in the cyclic voltammetry response of C$_\alpha$ Figure 6.1 shows the cyclic voltammetry of C$_\alpha$ and the reproducibility of the profile after chronoamperometry for 4 h.

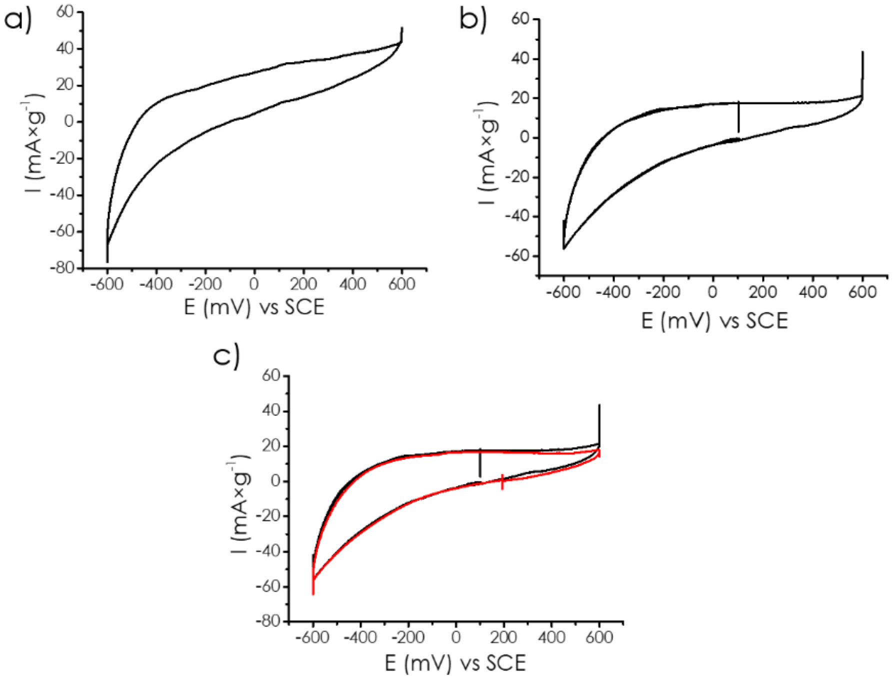

Figure 6.1. Cyclic voltammetry for the mp-C$_\alpha$ in a) He atmosphere, b) CO$_2$, and c) comparative of the CVs before (black) and after (red) 4 h of chronoamperometry

Similar electrochemical experiments were carried out also for mp-(P)C$_\alpha$ electrodes. Selected cyclic voltammetry responses are presented in Figure **6.2**. In contrast to the case of C$_\alpha$ and in agreement with its lower conductivity, mp-(P)C$_\alpha$ showed a resistive behavior both scanning towards positive potentials from natural voltage as well as to going to negative polarizations.

Also, as can be seen in Figure 6.2, mp-(P)C_α electrodes, was undergoing variations depending on the time of the electrochemical tests. Particularly remarkable is the changes in the cyclic voltammetry after submitting the samples to chronoamperometry for 2 hours. As can be seen in Figure 6.2, the electrical conductivity of the sample seems to increase upon the electrochemical treatment. In any case, these measurements indicate the lack of electrochemical stability of mp-(P)C_α, one possible reason could be the restructuration of the material and partial leaching of P atoms from the material. This hypothesis will be in agreement with a gradual loss of P in mp-(P)C_α going towards mp-C_α. In favor of this proposal, is the fact that the electrochemical voltammetry after electrical stress of mp-(P)C_α resembles the shape of the CV of the mp-C_α.

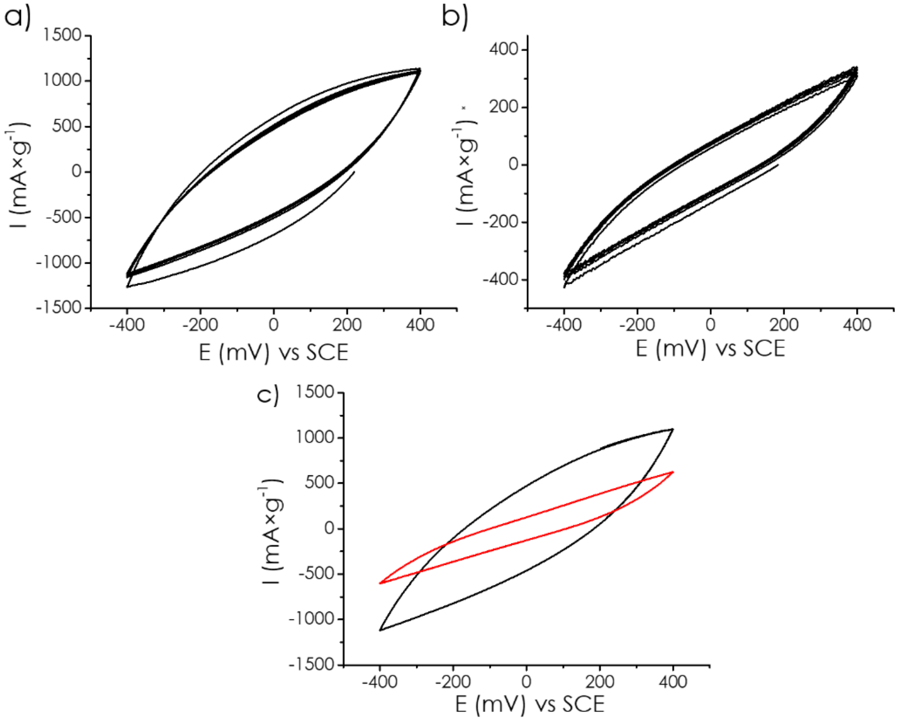

Figure 6.2. Cyclic voltammetry for the mp-(P)C_α in a) He atmosphere and b) CO_2, and c) comparative before (black) and after (red) 4 h of chronoamperometry.

Further information of the different electrochemical performance between mp-C_α and mp-(P)C_α electrodes were obtained from the Nyquist plot from from 0.3 Hz to 100 MHz which shows at lower arc radius for mp-C_α in comparison to mp-(P)C_α indicating that the charge transfers between the electrode and the electrolyte has lesser resistance in the case of the mp-C_α electrode. A comparison of the Nyquist plot is provided in Figure 6.3.

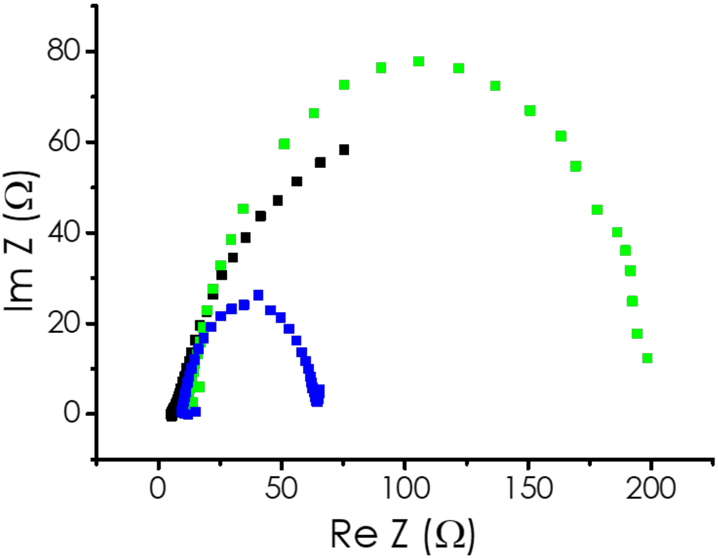

Figure 6.3. Nyquist plot for the samples mp-C_α (black), mp-(P)C_α (green) and mp-(P) $C_{\alpha Ex}$ (blue).

6.2.1 Electrochemical evidence of CO_2 reduction by microporous graphitic carbons

Polarization curves scanning to cathodic potentials in the range from 0 to -1.9 V were performed for C_α and (P)C_α electrodes both under He atmosphere and in the presence of CO_2. In these measurements, the occurrence of CO_2 reduction is revealed by recording higher cathodic currents in the presence of CO_2 with respect to an inert atmosphere under otherwise identical experimental conditions. Since the initial results using mp-C_α did not show significant differences in the current intensity in the absence or presence of CO_2, the mp-C_α powder were submitted to prior sonication treatment to better disperse and deaggregate mp-C_α particles, looking for lower average particle size, higher specific surface area and, therefore, higher electrochemical response. Using mp-C_α materials previously dispersed by ultrasounds we were able to record differences in the cathodic response depending on the presence or absence of CO_2. Figure

6.4 shows these linear scanning voltammetry curves showing an increase of current intensity and negative polarization potential when CO_2 was present in the electrolyte.

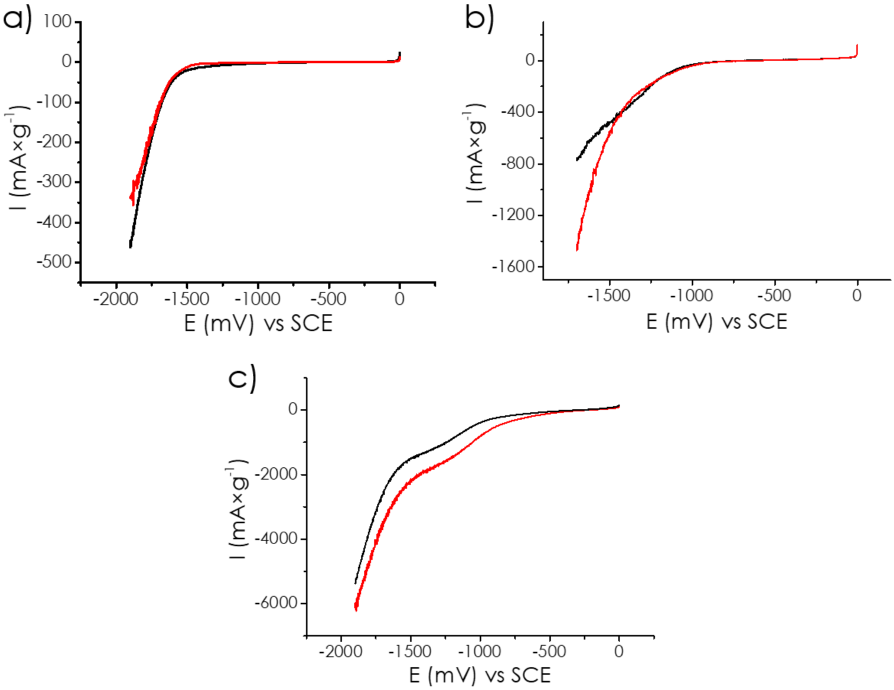

Figure 6.4. Linear sweep voltammetry for a) mp-C_α with He (red) and CO_2 (black) and b) mp-(P)C_α with He (red) and CO_2 (black) and c) mp-(P)$C_{\alpha Ex}$ with He (red) and CO_2 (black).

Larger differences in the LSV were recorded for the mp-(P)C_α electrodes, indicating that mp-(P)C_α could be a better electrocatalyst for CO_2 electroreduction. The polarization curves for this material are also presented in Figure 6.4.

Complementary electrochemical measurements leading to the same conclusion, i. e. that mp-(P)C_α is an electrocatalyst for CO_2 reduction were also reached by chronoamperometry tests. In these chronoamperometric measurements, the electrode was summited to a constant potential (- 1.3 V vs SCE), and during the curse of the chronoamperometry, a change on the atmosphere of the electrode by replacing He for CO_2 was made once the anodic current was stationary. This chronoamperometric profile is showed in Figure 6.5. As can be seen there, admission of CO_2 in the electrochemical cell, results in an increase in the cathodic current that was higher as the polarization potential of the electrode was more negative. These results indicate again that CO_2 can be reduced, increasing the current when this gas is present in the system. This increase in cathodic current is higher as the negative polarization potential increases. However, electrochemical stability of mp-(P)C_α after the chronoamperometric experiments shows again changes in the cyclic voltammetry curves in the same direction as previously commented. These changes in cyclic voltammetry indicate again the lack of stability of mp-(P)C_α in the potential and intensity window used in the experiments.

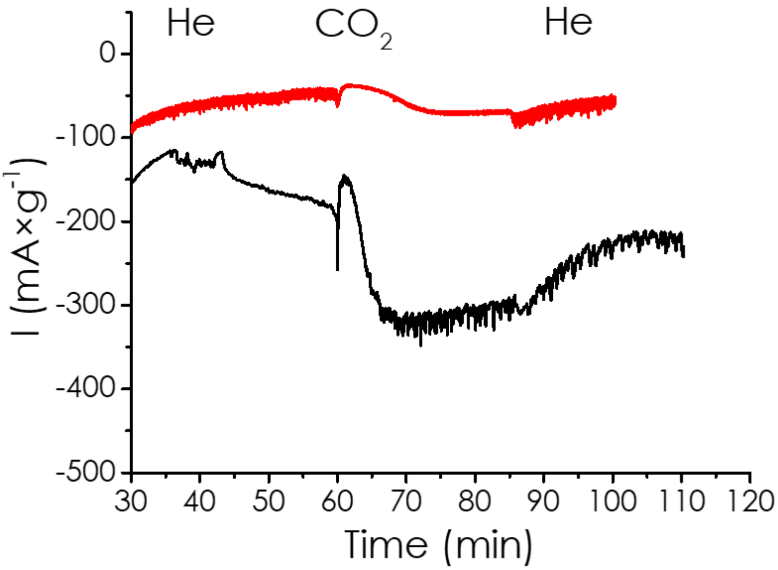

Figure 6.5. Chronoamperometry at -1.3 V vs SCE fo mp-(P)C_α (red) and mp-(P)$C_{\alpha Ex}$ (black) changing the gas bubbling in the electrolyte. For the sample mp-C_α there was no evident change in the current.

6.2.2 Electrochemical CO_2 reduction

To confirm by detection and quantification of products evolved the electrochemical CO_2 reduction due to the electrocatalytic effect of microporous graphitic carbons, electrolytic reactions were carried out using microporous graphitic carbons as cathodes and graphite as the counter electrode. Analysis of the evolved gas phase was carried out by gas chromatography using a mole sieve as the stationary phase in a microGC with a thermoconductivity detector (TCD) and He as carrier gas. The only gases detected in the gas phase were CO and H_2. Figure 6.6 presents the temporal profiles for gas evolution (CO and H_2) depending on electrodes. As can be seen there, the highest electrocatalytic activity was recorded for mp-(P)C_α, particularly after ultrasound treatment that has an activity for CO evolution or H_2 evolution between 4 and 5 times that of the non-doped mp-C_α electrode. Under the best conditions, a faradic efficiency for CO_2 reduction of about 42 % was achieved for mp-(P)C_α submitted to ultrasounds. It has to be commented that this faradic efficiency is very satisfactory compared to H_2 evolution which has a faradic efficiency, about 57 %. Analysis of the aqueous solution after the electrolysis by liquid 1H NMR spectroscopy did not reveal the presence of any additional product, analysis of the liquid by HPLC however reveal the presence of one product in the liquid phase, although it could not be identified by this technique and UV.

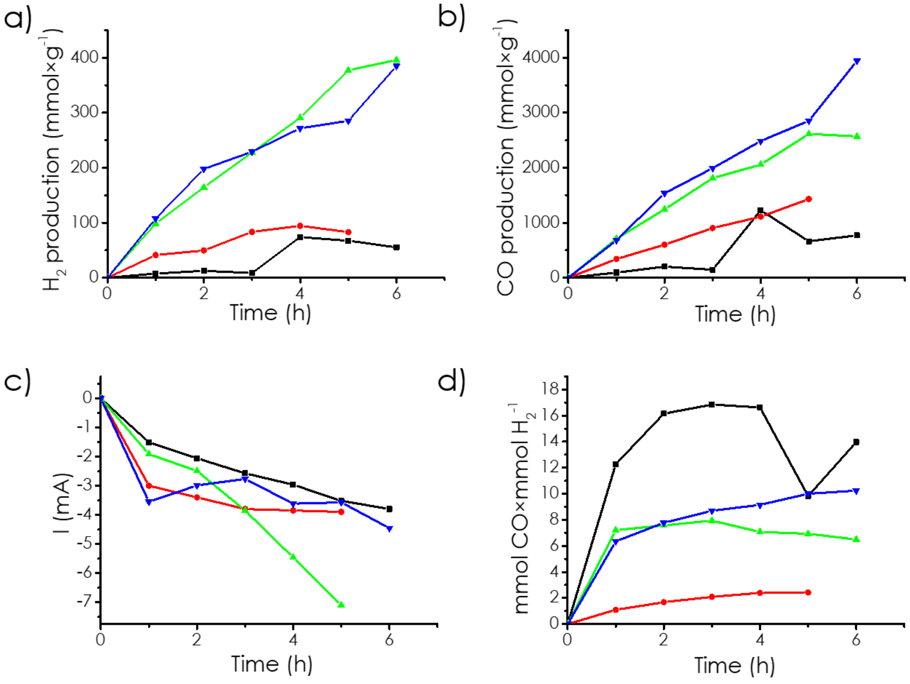

Figure 6.6. a) H_2 production, b) CO production, c) Current density during the experiment and d) ratio CO/H_2 obtained in the CO_2 electroreduction at -1.344 V vs Ag/AgCl of the tested materials mp-C_α (black), mp-$C_{\alpha\ Ex}$ (red), mp-(P)C_α (green) and mp-(P)$C_{\alpha\ Ex}$.

6.3 Conclusions

This chapter has shown the preparation of electrodes based on two selected microporous graphitic carbons. The selection of the materials to be evaluated as electrocatalysts was based on the information provided by the previous chapters. The electrodes of mp-(P)C_α exhibit an apparent electrocatalytic activity for CO_2 reduction as indicated by the higher cathodic current intensity in the presence of CO_2 compared to He and the increase in the chronoamperometric current when CO_2 enters into the electrochemical cell. In fact, analysis of the reaction products under electrolytic conditions shows the appearance of CO as the only products in the gas phase. However, the faradic efficiency of CO_2 reduction is very low, about 4 % compared to H_2 evolution. In addition, electrocatalysts based on mp-(P)C_α is not stable under operation conditions as the deduced by the change in the cyclic voltammetry under extensive electrochemical use. Therefore, the results of the present chapter, although promising the possibility to reduce the CO_2 in the absence of metals, requires much further optimization to increase the electrochemical stability and electrocatalytic efficiency for CO_2 reduction of doped microporous graphitic carbons. As a direction to follow, comparison between doped and non-doped microporous graphitic carbons shows the notable influence of doping on the electrocatalytic activity for CO_2 reduction.

6.4 References

1. Yuan, C.-S.; Ie, I.-R.; Zheng, J.-R.; Hung, C.-H.; Lin, Z.-B.; Shih, C.-H., A Review of Electrical Assisted Photocatalytic Technologies for the Treatment of Multi-Phase Pollutants. *Catalysts* **2021,** *11* (11), 1332.
2. Bonaccorso, F.; Colombo, L.; Yu, G.; Stoller, M.; Tozzini, V.; Ferrari, A. C.; Ruoff, R. S.; Pellegrini, V., Graphene, related two-dimensional crystals, and hybrid systems for energy conversion and storage. *Science* **2015,** *347* (6217), 1246501.
3. Varela, A. S.; Ju, W.; Bagger, A.; Franco, P.; Rossmeisl, J.; Strasser, P., Electrochemical Reduction of CO2 on Metal-Nitrogen-Doped Carbon Catalysts. *ACS Catalysis* **2019,** *9* (8), 7270-7284.
4. Silva, W. O.; Silva, G. C.; Webster, R. F.; Benedetti, T. M.; Tilley, R. D.; Ticianelli, E. A., Electrochemical Reduction of CO2 on Nitrogen-Doped Carbon Catalysts With and Without Iron. *ChemElectroChem* **2019,** *6* (17), 4626-4636.
5. Bandosz, T. J.; Ania, C. O., Origin and Perspectives of the Photochemical Activity of Nanoporous Carbons. *Advanced Science* **2018,** *5* (9), 1800293.

CHAPTER 7.

EXPERIMENTAL SECTION

7.1 Material synthesis

7.1.1 Microporous graphenic carbon using a soft template

The graphene precursor, low molecular weight chitosan (Aldrich), was dissolved in 25 mL of acidified water (MilliQ water) using glacial acetic acid (98%, Aldrich): 5 wt % in the case of the 3DNC22 or 2 wt % for the 3DNCβ. This difference is due to the basicity of the templates. The urea was settled in a concentration of 1.7 wt %. The soft template (hexametilenimine -Aldrich- or tetraethylamonium bromide -Aldrich-) was added in a concentration of 6 wt % under vigorous stirring for 2 h. At this time, the resulting gel was introduced into a 35 mL stainless steel autoclave that was heated at 90 °C for 90 h rotating the mixture at 60 rpm. The resulting yellow-brown solid was washed with abundant water and then dried at 60 °C.

Pyrolysis was carried out on two different devices. One of them was in a horizontal electrical furnace with an Ar flux of 200 mL × min^{-1}. Initially, to anneal the sample, the temperature increase rate was 1 °C × min^{-1} up to 200 °C, holding this temperature for 2 h. After that, a temperature of 900 °C was reached at the same initial rate and held for 2 h. The second system was a microwave oven, with a special ceramic container of silicon carbide. The equipment was purged with a flux of N_2 to reduce de O_2 concentration. The samples were submitted to three consecutive cycles of 1 min of irradiation at 800 W and 2 min dueling time.

7.1.2 Microporous 3D graphenic carbon based on cyclodextrins

The cyclodextrins (Aldrich) pyrolysis was performed in a horizontal electric furnace under an inert atmosphere using 200 mL × min^{-1} of Ar flux. The heating program is the following: the temperature increase slope of 5 °C × min^{-1} until 300 °C for 2 h and then 10 °C × min^{-1} until 900 °C for 2 h. The Ar flux was maintained until the material reached room temperature.

7.1.3 Microporous 3D graphenic carbon doped with heteroatoms

An amount of 200 mg of α-cyclodextrin (0.41 mol, 978.8 g × mol^{-1}, Aldrich) was dissolved in 20 mL of ultrapure water (MilliQ grade). Here, different amounts of phosphoric acid were added as phosphorous element precursors according to Table 7.1. or urea as nitrogen source.

After 24 h of stirring, the solution was dried by heating at 60 °C, obtaining a white powder. This product was pyrolyzed in a horizontal electrical oven by heating at 10 °C × min^{-1} up to 900 °C and held for 2 h under an inert atmosphere (Ar flux) of 200 mL × min^{-1}.

Table 7.1. Added volume of the phosphorous precursors to the materials.

Sample	**V (H_3PO_4) (µL)**	**V ($C_6H_{18}O_{24}P_6$)[a] (µL)**	**m ($CO(NH_2)_2$) (mg)**
mp-C_α	-	-	-
(P)C_α-1 or mp-(P)C_α	27.9	-	-
(P)C_α-2	139.6	-	-
(P)C_α-3	279.3	-	-
(P)C_α-4	0	279.3	-
(P)C_β-2	139.6	-	-
(P)C_γ-2	139.6	-	-
mp-(N)C_α	-	-	60

[a] $C_6H_{18}O_{24}P_6$ corresponds to phytic acid.

In the case of the β-cyclodextrin, 0.352 mmol (1135.0 g × mol^{-1}, Aldrich) were dissolved, and for γ-cyclodextrin, 0.308 mmol (1297.12 g × mol^{-1}, Aldrich) replacing the amount of α-cyclodextrin, using afterwards the same procedure as indicated earlier.

The preparation of the N-doped microporous graphitic carbon was similar to the P-doping replacing the P precursor by urea in the indicated amount in Table 7.1.

7.2 Reaction procedure

7.2.1 Oxidation of benzylamine

The oxidation of benzylamine was carried out by the previous activation of 10 mg of the catalysts in a round bottom flask at 120 °C in vacuum for 24 h. Then, this activated material was placed in a two-neck round bottom flask with 20 mmol of benzylamine (previously purified by redistillation ≥ 99.5 %, Merck), and the mixture was sonicated for 20 min.

The reaction mixture was vigorously stirred, heated to 80 °C, and purged with oxygen (99.999 %) at atmospheric pressure. Aliquots were periodically taken and diluted in a chloroform solution that contained a known amount of nitrobenzene as external standard. Then, they were analyzed by gas chromatography using a 30 m column with phenyl methyl silicone as stationary phase and a flame ionization detector, and the quantification was based on calibration plots considering the response factor and the relative peak areas.

In the case of the reusability tests, the catalyst was recovered by filtration with a polytetrafluoroethylene (PTFE) filter with a 0.2 µm pore diameter. After that, the catalyst was recovered from the filter, washed with chloroform, and dried at 80 °C.

7.2.2 Water splitting reaction

The photocatalytic reactions were carried out in a 51 mL quartz photoreactor fitted with a manometer, with inlet and an outlet valves, as can be seen in Figure 7.1 The irradiation was carried out using a 300 W Xe lamp (Hamamatsu, 1,6 sun power) with UV-Vis light range or simulated sunlight irradiation (OrielTM, 1 sun power).

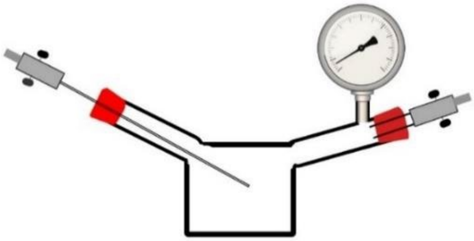

Figure 7.1. Reactor scheme for photocatalytic reactions. As seen, it has 2 valves for purging and sampling as well as a manometer to control de pressure during the reaction.

First, the photocatalyst was dispersed in 30 mL of water (1,5 mg × mL^{-1}) using a Sonic tip (FisherbrandTM Model 705 at 40% of 700 W for 1 h using 1 s on 1 s off sequence). After that, the necessary amount of suspension is introduced into the reactor, added 4 mL of methanol (Aldrich) or 3.5 mL of triethanolamine (Aldrich) as an electron donor, and MilliQ water until a volume of 20 mL of the total mixture is reached. The system was purged with Ar for 10 min to remove air before the irradiation.

In the case of O_2 evolution $(NH_4)_2Ce(NO_3)_6$ (Aldrich) was added as the electron acceptor in a concentration of 1 mM.

The gas phase was analyzed using a gas chromatograph (Agilent 490 MicroGC) equipped with a molecular sieve 5 Å column with TC detector and Ar as carrier gas.

7.2.3 Platinum photodeposition

For the Pt photodeposition, the photocatalyst was dispersed in 30 mL of MilliQ (1.5 mg × mL^{-1}) water using ultrasounds. 7.5 mL of this suspension were introduced into the reactor with 4 mL of methanol as electron donor and H_2PtCl_6, 0,1 mM. After 15 min of irradiation, the solid was recovered by centrifugation (HettichZentrifugen EBA 21) at 6000 rpm for 30 min. The supernatant was removed, and the solid was washed several times with MilliQ water by centrifugation. The material was analyzed by ICP-OES to determine the percentage of Pt and by HRTEM to monitor the Pt nanoparticles and to measure the average particle size. The Pt containing solid was used in an H_2 evolution reaction.

7.2.4 Chromium photodeposition

Chromium oxide photodeposition was carried out for locating the photogenerated holes. In this case, as previously described, the photocatalyst was dispersed in 30 mL of MilliQ water using ultrasounds in a concentration of 1.5 mg × mL^{-1}. 7.5 mL of this suspension were introduced in the photoreactor and, adding also 12.5 mL of MilliQ water with 0.1 mM $CrCl_2$. After 15 min of irradiation using the Xe lamp, the suspension was centrifuged (HettichZentrifugen EBA 21) at 6000 rpm for 30 min. The supernatant was removed and the solid was washed with MilliQ water by centrifugation several times. The material was analysed by ICP-OES to measure the Cr percentaje and by TEM to monitor the CrO_x presenceThe obtained Cr-containing photocatalyst was characterized using HRTEM. Also, this metal-doped material was used in the photocatalytic OER.

7.2.5 CO_2 photoreduction

As in the photocatalytic HER and OER, the photocatalytic reactions are carried out in the 51 mL quartz photoreactor showed in Figure 7.1.

First, 40 mg of the mp-C were dispersed in 30 mL of acetonitrile by ultrasonication tip (FisherbrandTM Model 705 at 40 % of 700 W for 1 h using 1 s on 1 s off sequence). After that, 7.5 mL of the suspension was added to the photoreactor with 4 mL of triethanolamine as a sacrificial agent and 4 mL of water as a proton source. To reach the 20 mL of the liquid phase, 4.5 mL of acetonitrile was added too.

The suspension was purged for 10 min using pure CO_2, heated at 50 °C and pressurized until a manometer pressure of 0.4 bar. Irradiations were carried out using a 300 W Xe lamp (Hamamatsu, 1.6 sun power) with UV-Vis light range or simulated sunlight irradiation (OrielTM, 1 sun power).

The quantum yield value at single wavelengths (AQY) was determined under irradiation with a 150 W Xe lamp equipped with a Czerny Turner monochromator to select the irradiation wavelength.

The gas products were analyzed by a gas chromatograph (Agilent 490 MicroGC) equipped with a molecular sieve 5 Å column with TC detector and Ar as carrier gas. To properly quantify the CO production, the analysis was also carried out with a 7890A chromatograph with a column Carboxen®-

1010 PLOT L × I. D. 30 m × 0.53 mm, average thickness 30 µm with a TC detector and He as the carrier gas.

7.2.6 Electrocatalytic CO_2 reduction

The electrocatalytic tests for the CO_2 reduction were carried out in a single chamber three-electrode electrochemical cell, with a bar of graphite as counter electrode and an Ag/AgCl electrode as reference. The working electrodes were prepared by depositing a thin layer of the mp-C photocatalyst with PVDF as binder on the 1 × 1 cm Ti foil. This cell was connected with a microGC which analyzed the gas phase of the cell's head space. The total volume of the cell is 332 mL. Figure 7. 2 shows a photo of the electrochemical cell and the electrodes.

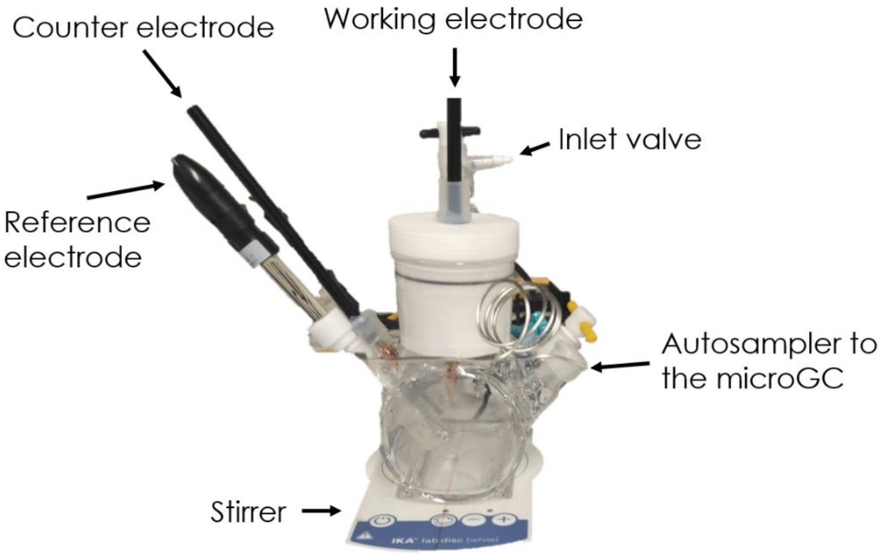

Figure 7.2. Electrochemical cell used in the CO_2 electroreduction, with controlled distances between the electrodes, an inlet valve and a direct connection to the microGC to analyze the gas evolution.

150 mL of $KHCO_3$ 0.5 M were introduced into the cell and pure CO_2 was bubbled for 1 h to ensure the complete saturation of the solution and the cell. After that, the cell was sealed, and using as current source a Keithley device Model 6620. -1.344 V (vs Ag/AgCl electrode) were applied for the 5 h.chronoamperometric test. The gas samples were taken every hour to follow the gas temporal phase evolution. Last, the liquid phase was analyzed

by HPLC of Shimadzu, model LC-20AD, and UV spectroscopy using a Shimadzu device, model UV-2700.

7.3 Electrochemical measurements

7.3.1 Electrode preparation

The inks used to prepare the electrodes were prepared as follows. The photocatalyst was ultrasonicated in water using the same conditions as previously commented and then, the suspension was dried at 60 °C. 10 mg of the material were introduced in 200 µL of ethanol, where 50 µL of Nafion 5% were added too. This ink was deposited on fluorine-doped tin oxide glass (FTO) on an area of 1 × 1 cm. These electrodes were introduced overnight in the electrolyte before their use to ensure the impregnation of all the pores.

In the case of the electrodes for the CO_2 electroreduction, after having the ultrasonicated material completely dry, 27 mg of the material were mixed with 3 mg of polyvinylidene fluoride (PVDF) as binder and 2 drop of N-methylpyrrolidone (NMP) as solvent. A previously cleaned piece of Ti foil 1 × 1 cm was covered with the ink and dried at 60 °C overnight. The cleaning of the Ti foil was performed by sonicating the pieces in ethanol for 5 min to remove any impurity that could be on the surface, followed by drying using compressed air. As previously commented, these electrodes were immersed in the electrolyte solution overnight before their use to ensure a thorough impregnation of the pores.

7.3.2 Photoelectrochemical measurements of the mp-(P)C materials

The cyclic voltamperometry (CV) and chronoamperometry (CA) measurements were carried out in a three-electrode single-compartment electrochemical cell connected to a potentiostat device Solatron. The reference electrode was Ag/AgCl electrode and the counter electrode was Pt. As working electrode, a thin film of the studied material deposited on a 1 × 1 cm of FTO was used. As the electrolyte, an aqueous solution of KCl 1 M was used as electrolyte.

In the case of CV, the scan speed was 20 $mV \times s^{-1}$. With an electrochemical potential window from -1.8 V to 1.8 V vs Ag/AgCl. The CV measurements were performed at least 5 times.

For the external quantum yield efficiency, the scan rate was 5 nm × s^{-1} using a 5000 W Xe lamp, coupled with a Zolix Omni-λ300D monochromator was used as irradiation source.

In the case of the CA measurements, the electrodes were stabilized at the working potential for 5 min before starting at least 5 cycles 1 min light on, 1 min light off. The irradiation source was a 300 W Xe lamp (Hamamatsu, 1.6 sun power).

7.3.3 Conductivity measurements

The conductivity of the prepared electrodes on the Ti foil was measured using a 4 probes head, correlating the measured potential when a current intensity is applied.

Conductivity measurements were carried out on 3 independent prepared electrodes, and, at least, in 4 different regions of the film to get a proper mean value for the material.

The conductivity is obtained from the slope of the linear relation of the potential vs the applied current, corrected by the thickness of the layer of the material according to the following calculation:

$$Conducticity = \frac{Slope}{Correction\ factor} \qquad \text{Eq. 8.1}$$

$$Correction\ factor = \frac{\pi \cdot Thickness}{\ln 2} \qquad \text{Eq. 8.2}$$

7.3.4 Nyquist plots

Nyquist plots were measured using the prepared electrode was measured in the frequencies range from 0.3 Hz to 100 MHz, at a scan rate of 10 mV × s^{-1} acquiring 10 points per decade using graphite as the counter electrode and SCE as the reference electrode. An aqueous solution of Na_2SO_4 0.5 M was used as electrolyte and the device is a VMP-3e Multichannel (10 channels) potentiostat.

7.3.5 Mott-Schottky plots

Mott Schottky plots were recorded for the electrodes containing the deposited material was the working electrode, and a graphite bar as counter electrode and Ag/AgCl as reference electrode. The experiment was carried out from -1 V to 0 V, at the frequencies 1000 Hz, 1500 Hz and 2000 Hz.

7.3.6 Photoelectrochemical measurements of the mp-C_α for CO_2 photoreduction

The photoresponse measurements were carried out using the same cell as previously commented for CV plots, using Ag/AgCl as the reference electrode, graphite as the counter electrode, and the mp-C_α deposited on FTO as the working electrode. $KHCO_3$ 0.5 M was used as electrolyte. Either N_2 or CO_2 was bubbled in the solution to ensure the complete saturation of the electrolyte.

In the case of CV, the scan speed was 20 mV × s^{-1}. Measurements were performed from -1 V to 1 V vs Ag/AgCl, at least 5 times. For the CA tests, the electrode was stabilized for 5 min at the selected potential and then irradiated for 1 min using the same Xe lamp that was used in the photocatalytic tests. Then, the electrode was allowed to relax for 2 min. This cycle was repeated at least 5 times.

7.3.7 Electrochemical characterization for CO_2 electroreduction

A 0.5 M aqueous solution of $KHCO_3$ was employed as electrolyte, using graphite and SCE as counter and reference electrodes, respectively. The working electrodes were those containing a fil of the material deposited on Ti foil previously described and kept overnight in the electrolyte to equilibrate. As potential station, VMP-3e Multichannel (10 channels) potentiostat was employed. It should be noted that each measurement was carried out twice for each electrode and, at least, in two independent prepared electrodes to check the reproducibility of the results. The conditions for the different measurements were the following:

Cyclic voltammetry (CV)

The cyclic voltametries were carried out from -0.6 to +0.6 V vs SCE under inert atmosphere, at a scan speed of 10 mV × s^{-1}, and, for 5 to 10 cycles to check the stability of the electrodes. In addition, to know the influence of the presence of CO_2 on the current intensity, these cycles were repeated for the same electrode, under CO_2 atmosphere

Chronoamperometry (CA)

Once selected the working potential from the LSV plot, the electrode was left for 60 min to reach a stable state under inert atmosphere by bubbling He for

15 min. After that, in order to measure the changes in the current, CO_2 was bubbled through the solution for 15 min. followed other 15 min more in He atmosphere to recover the initial state.

Linear sweep voltammetry (LSV)

LSVs were carried out from 0 V to -1.9 V vs SCE in a scan speed of 20 mV × s^1 under He atmosphere and CO_2 atmosphere, in order to determine what potential is required to reach the CO_2 electroreduction,

7.4 Characterization techniques

7.4.1 Diffuse Reflectance UV-Vis Spectroscopy (DRS) and Fluorescence Spectrocopy

The UV-Visible optical absorption spectroscopy is based on the analysis of electromagnetic radiation in the range of 200 to 800 nm absorbed in opaque solid samples, compared to a reference white solid. $BaSO_4$ was used in the present case as reference. The measurements were carried out in a Cary 5000 Varian spectrophotometer.

In the case of the steady-state fluorescence measurements, a Photon Technology International LPS-220B Spectrofluorometer, equipped with a monochromator in the range of 200 to 700 nm was used. The excitation wavelength was 270 nm, and emission was recorded from 295 to 550 nm. Finally, time-resolved fluorescence measurements were performed with an Easylife X Fluorescence Lifetime fluorimeter with a final decay time of 250 ns, an integration time of 0.1 s and a gain between -1.0 and 1.0. The measurements were performed exciting with a UV diode and interposing a cut-off filter to detect all photons emitted at wavelengths longer than 500 nm.

7.4.2 Combustion elemental analysis

The elemental analysis quantifies the amount of carbon, hydrogen, nitrogen and sulfur in the samples. This technique is based on the thermal oxidation of the material using pure O_2 at high temperatures (170-1800 °C), and quantifying the products CO_2, H_2O, SO_2, and NO formed. In the present measurement, a Euro EA3000 Elemental Analyzer (EuroVector) was used, employing sulfanilamide as calibration compound.

7.4.3 Field Emission Scanning Electron Microscopy (FESEM)

Field Emission Scanning Electron Microscopy provides information of the particle shape, size distribution and composition of the sample surface, scanned with an electron beam while a monitor displays the corresponding information according to the detector.

These images were obtained by a Zeiss Ultra 55 microscope and the elemental analysis by the dispersive X-ray detector (EDX) (Oxford instruments).

7.4.4 Inductive Coupled Plasma-Optical Emission Spectrometry (ICP-OES)

Inductive Coupled Plasma Optical Emission Spectrometry is an analytical technique to determine the composition of a sample by vaporing a liquid solution in a plasma chamber allowing to determine the concentration of cations in varying sample types after digestion with strong corrosive acids. In the present thesis, the ICP-OES was used to know the P content in the different materials using Varian 715-ES, CA, USA.

7.4.5 Isotherm gas adsorption

Isotherm gas adsorption determines the adsorbed gas to calculate the specific surface area of a solid and the pore and shape of the pores. These measurements were carried out with different gases: N_2 and Ar at 77 K and CO_2 at 283 K in a gravimetric analyzer IGA-3.

7.4.6 Raman spectroscopy

In Raman spectroscopy analysis, a beam of monochromatic light is incident on the sample to be characterized. Most of the scattered light has the same frequency as the incident light. However, a small fraction does not, as a result of the interaction of this beam with the material. This radiation of different wavelength as the incident beam is known as Raman scattering and is characteristic of the chemical nature and state of the sample, independent of the incident radiation.

Raman spectra were recorded with 514 nm laser excitation on a Renishaw Raman spectrophotometer (“Reflex”) equipped with a Leica optical microscopy and a charged coupled device camera. The laser power in the sample was 25 mW. Each spectrum was an average of 20 acquisition scan with a resolution of 4 cm^{-1}.

7.4.7 Solid-State Nuclear Magnetic Resonance Spectroscopy

Solid-state ^{31}P NMR spectra were recorded at room temperature using a Bruker AV400WB with $\pi/2$ pulse sequences of $\tau = 5$ µs and a relaxation time of 5 s. The measurements were carried out with magic-angle spinning at the rate of 10 kHz. Each spectra componds to the average between 100 and 400 scans.

7.4.8 Thermogravimetric analysis (TGA)

TGA measures the variation of the mass with the temperature to study the stability of the materials. These analyses were carried out in an equipment Mettler Toledo TGA/SDTA 851e, with a temperature range from 20 to 900 °C, the heating slope of 10 °C × min^{-1} and gas flux (air or N_2) of 20 mL × min^{-1}.

7.4.9 Transient absorption measurements

Transient absorption spectra were recorded using the fourth harmonic of a Q switched YAG: Nd laser (Quantel Brilliant, 266 nm, 15 mJ per pulse, 7 ns fwhp) coupled to mLFP122 Luzchem miniaturized detection equipment. The suspension under study had a concentration of 0.5 mg × mL^{-1} in acetonitrile and was purged with N_2 at least 15 min before the measurement. The suspension was placed in a quartz cuvette capped with septum. This transient absorption spectrometer included a 300 W ceramic Xe lamp, 125 mm monochromator, Tektronix TDS-2001C digitizer, compact photomultiplier, power supply, cell holder, fiber-optic connectors, computer interfaces, and a software package developed in the LabVIEW environment from National Instrument. The laser flash generated 5 V trigger pulses with controlable frequency and delay. The rise time of the detector/digitizer was a few ns at 300 MHz (2.5 GHz sampling). The monitoring beam was provided by a ceramic xenon lamp and delivered through a fiber-optic. The laser pulse was probed by a fiber that synchronized the photomultiplier detection system with the digitizer operating in the pre-trigger.

7.4.10 Transmission Electron Microscopy (TEM)

TEM uses an electron beam that collides with the sample. Depending on its thickness, composition, crystallinity, etc. the electrons will be dispersed or they will pass through it. These electrons are modulated and driven by lenses to create a final image in different tones of grey, corresponding to the dispersion of the incident electrons. Therefore, TEM images can give information about the sample structure, such as crystallinity, orientation plane, particle size, etc.

TEM images were recorded using a microscope JEOL JEM 2100F operating at 200 kV, coupled with a X-Max 80 energy dispersive X-ray detector (EDX) (Oxford instruments). In addition, the microscope is equipped with the STEM unit, dark-field and high-angle field image detectors (HAADF) for easier observation of elements with different atomic numbers.

7.4.11 X-Ray diffraction (XRD)

XRD is based on the measurement of the light reaching a detector at different angle of monochromatic radiation of X-ray going through a sample. The variation of the detection angle let the registration of the diffraction peaks, which correspond to the crystallographic planes of the material. This technique provides information about the structure, crystal size, and preferential orientation, among others. The XRD patterns were obtained with a Cubix-Pro (PANalytical), equipped with the detector PANalyticalX'Celerator. The monochromatic X-ray radiation was Cu Kα (ʎ$_1$= 1.5406 Å, ʎ$_2$= 1.5444 Å, I$_2$/I=0.5), with a voltage of 45 kV and 40 mA. A variable slit with an irradiated sample area of 5 mm is used and the goniometer arm length is 20 mm. Diffractograms were obtained at room temperature in the 2θ angle range between 2 and 90 °, with an increment of 0.02 ° (2θ).

7.4.12 X-Ray Photoelectron Spectroscopy (XPS)

XPS is a technique that involves the excitation by an X-ray beam at an appropriate wavelength of the core electrons of the elements present in a sample. The analysis of the emitted electrons provides information on the energy of each level, obtaining the composition of the surface of the material as well as the chemical state of the elements.

The XP spectra were recorded on a SPECS spectrometer with a Phoibos 150-9MCD detector, using a non-monochromatic Al Kα X-ray source (1483.6 eV) operating at 50 W. Samples were evacuated into a spectrometer pre-chamber at 9-10 mbar. The quantification and processing of the spectra are carried out with CASA XPS software, and the charge correction is based on coinciding as internal reference the carbon C 1s signal, whose binding energy corresponds to the binding energy value of 284.5 eV.

The samples were prepared by suspending 5 mg of the material in 20 mL of water and sonicating using a Sonic tip (FisherbrandTM Model 705 at 40 % of 700 W for 15 min using 1 s on 1 s off pulses). After that, one or two drops are deposited on the TEM sample holder.

7.5 Other procedures

7.5.1 Valence band calculation

The valence band spectrum was first calibrated by C1s as in the case of the XPS deconvolution. The position of the valence band minimum energywas obtained by the intersection of the tangent line of the spectra and the baseline for the lowest energy peak of the XPS spectrum. The obtained value is referred to Fermi level E_v^f, therefore it can be corrected to refer to NHE (E_v^{NHE}) according to the Equation

$$E_v^{NHE} = E_v^f + (\phi_{sp} - 4.44) \qquad \text{Eq. 8.3}$$

Or versus vacuum (E_v^{Vac})

$$E_v^{Vac} = E_v^f + \phi_{sp} \qquad \text{Eq. 8.4}$$

Being ϕ_{sp} the work function of the equipment, which was calibrated using silver and gold. In our instrument, the obtained value was 4.244 eV.

CHAPTER 8.

CONCLUSIONS

The present doctoral thesis has reported a new strategy for the microporous graphitic carbons preparation based on soft templation. In addition, we have found that P-doping of microporous graphitic carbons derived from cyclodextrins is a suitable approach that can be implemented to increase the photocatalytic performance of these carbons for overall water splitting and H_2 evolution. For the first time, it has been found that also these carbons can promote photocatalytic CO_2 reduction, resulting in a selective CO_2 evolution. For this reaction, it seems that doping is unfavorable, but further studies are necessary to understand the origin of these observations. It has also been found that similarly to other semiconductors, the use of carbon dots is a metal-free strategy to increase photocatalytic activity.

In particular, the concrete conclusions of the present thesis are the following:

- Tetraethylammonium and hexametilenimine are suitable soft templates to structure filmogenic polysaccharides, resulting after pyrolysis in microporous graphitic carbons with a defined porosity. These structured graphitic carbons exhibit an enhanced catalytic activity to promote aerobic oxidations compared to other analogous materials, such as flat defective graphenes, graphene oxide, and activated carbons. Theoretical calculations suggest that O_2 activation by confinement defects can be responsible for this enhanced catalytic activity.

- P-doping increases the photocatalytic activity of microporous graphitic carbons derived from cyclodextrin pyrolysis for H_2evolution, O_2 evolution, and overall water splitting. The most efficient photocatalyst is obtained from α-cyclodextrin and requires an optimal amount of P content. In the absence of any metal, a photocatalytic activity under simulated sunlight of 2.5 mmol × $g^{-1}$was achieved for H_2 production in the presence of a sacrificial agent.
- Microporous graphitic carbons derived from cyclodextrins reduce selectively the CO_2 to CO upon irradiation with solar simulated sunlight. It was found that N or P doping decreases the photocatalytic activity in this reaction compared to the un-doped carbon. Transient absorption spectroscopy indicates different reasons for this photocatalytic activity decrease. In the case of N doping, and based on CO_2 quenching, the decrease in the photocatalytic activity appears to be due to the shorter lifetime of the photogenerated charge carriers. In the case of P doping, the lack of CO_2 quenching for the photogenerated transients indicates the lack of reactivity of these transients for CO_2, and the most likely reason is the unfavorable potential for this reaction.
- The microporous graphitic carbon obtained by the pyrolysis of the cyclodextrins can be applied in CO_2 electroreduction. The obtained results are promising according to the produced CO (4000 mmol × g) and the H_2 (400 mmol × g), with a faradic efficiency of 42 % to CO in the case of the P-doped material. This performance is notably better than the non-doped material, which produces 4 times less CO and H_2.

The above results and conclusions show how the present PhD. has contributed to the advance of the field of carbo- and photocatalysis by avoiding the use of transition metals to promote these reactions. The absence of transition metals constitutes a step forward toward sustainability and a circular economy. Considering the importance of renewable energy sources and particularly, the storage of solar energy into chemical compose that can be used as fuels, the present results indicate that it could be possible to develop efficient carbon-based materials for these processes.

Abstracs

9.1 Resumen

En la actualidad, el elevado consume energético y el aumento de la concentración de CO_2 en la atmósfera han hecho necesaria la búsqueda de nuevas opciones para los procesos actuales. Una respuesta ha sido el aprovechamiento de la radiación solar para producir H_2 a partir de la ruptura fotocatalítica del agua o la reducción del CO_2 emulando a la naturaleza. Para ello, se propone el uso de materiales basados en carbono, de mayor abundancia y accesibilidad que los metales y óxidos metálicos.

Además, un punto a tener en cuenta es la morfología, ya que haciendo uso del denominado “efecto de confinamiento” de los materiales 3D mejora notablemente la capacidad catalítica de los mismos.

Es por esto por lo que, en la presente Tesis Doctoral, se ha desarrollado la posibilidad de obtener materiales grafénicos con estructuración tridimensional, presentado microporos en los que tiene lugar dicho efecto de confinamiento. De este modo, estos materiales son capaces de promover tanto la reacción de oxidación de la benzilamina como la reacción fotocatalítica de obtención de H_2 a partir de agua y la de reducción de CO_2. Concretamente, los materiales se han obtenido, por un lado, mediante el uso de agentes plantilla y la capacidad de recubrimiento de polisacáridos naturales como es el quitosano; y por otro, sin agentes plantilla, aprovechando la estructura de las ciclodextrinas como precursores del grafeno microporoso. Además, estos últimos materiales se han dopado con heteroátomos, en concreto fósforo, para mejorar la actividad fotocatalítica de estos materiales microporosos basados en carbono.

9.2 Abstract

Nowadays, the high energy consumption and the increase of the concentration of CO_2 in the atmosphere have made it necessary to search for new options for the current processes. One possible answer has been the use of solar radiation to produce H_2 from the overall photocatalytic water splitting or the photoreduction of CO_2, by emulating nature. In this context, carbon-based materials, which are more abundant and accessible than metals and metal oxides, are proposed as catalysts.

In addition, a point to take into account is the morphology, since making use of the so-called "confinement effect" of 3D materials significantly improves their catalytic capacity.

This is the reason why, in this Doctoral Thesis, the possibility of obtaining graphene materials with three-dimensional structuring has been developed, presenting micropores in which this confinement effect takes place. In this way, these materials have been able to promote both the oxidation reaction of benzylamine and the photocatalytic reaction of obtaining H_2 from water and the reduction of CO_2. Specifically, the materials have been obtained, on the one hand, by using template agents and the coating capacity of natural polysaccharides such as chitosan; and on the other hand, without template agents, taking advantage of the structure of cyclodextrins as precursors of microporous graphene. In addition, the latter materials have been doped with heteroatoms, specifically phosphorus, to improve the photocatalytic activity of these carbon-based microporous materials.

9.3 Resum

En l'actualitat, l'elevat consum energètic i l'augment de la concentració de CO_2 en l'atmosfera han fet necessària la cerca de noves opcions per als processos actuals. Una resposta ha sigut l'aprofitament de la radiació solar per a produir H_2 a partir de la ruptura fotocatalítica de l'aigua o la reducció del CO_2 emulant a la naturalesa. Per a això, es proposa l'ús de materials basats en carboni, de major abundància i accessibilitat que els metalls i òxids metàl·lics.

A més, un punt a tindre en compte és la morfologia, ja que fent ús del denominat "efecte de confinament" dels materials 3D millora notablement la capacitat catalítica d'aquests.

És per això que, en la present Tesi Doctoral, s'ha desenvolupat la possibilitat d'obtindre materials grafénics amb estructuració tridimensional, presentat microporus en els quals té lloc aquest efecte de confinament. D'aquesta manera, aquests materials són capaços de promoure tant la reacció d'oxidació de la benzilamina com la reacció fotocatalítica d'obtenció d'H_2 a partir d'aigua i la de reducció de CO_2. Concretament, els materials s'han obtingut, d'una banda, mitjançant l'ús d'agents plantilla i la capacitat de recobriment de polisacàrids naturals com és el quitosan; i per un altre, sense agents plantilla, aprofitant l'estructura de les ciclodextrines com a precursors del grafé microporós. A més, aquests últims materials s'han dopat amb heteroàtoms, en concret fòsfor, per a millorar l'activitat fotocatalítica d'aquests materials microporosos basats en carboni.

List of publications

The publications that conforms the present thesis are the following:

Chapter 3

Microporous 3D graphitic carbons obtained by soft templating as carbocatalysts for aerobic oxidation

Garcia-Mulero, A.; Baldoví H. G.; Dhakshinamoorthy, A.; Primo, A.; Corma, A.; Garcia, H.

Published in *Applied Catalysis A: General*, 312 (2021) 118014

Chapter 4

Band engineering of semiconducting microporous graphitic carbons by phosphorous doping: enhancing of photocatalytic overall water splitting

Garcia-Mulero, A.; Rendon-Patiño, A.; Asiri, A. M.; Primo, A.; Garcia, H.

Published in *ACS applied materials & interfaces*, 13 (2021) 48753–48763

Chapter 5

All-carbon microporous graphitic photocatalyst-promoted reduction of CO2 to CO in the absence of metals or dopant elements

Garcia-Mulero, A.; Asiri, A. M.; Albero, J.; Primo, A.; Garcia, H.

Published in *Nanoscale*, 14 (2021) 11575-11582